ISSN 1880-8468

Technical Report of
International Development Engineering

国際開発工学報告

TRIDE-2016-02 May 9, 2016

Abstracts of Bachelor Theses
Presented in Feburary 2015

Department of International Development Engineering,
Graduate School of Science and Engineering,
Tokyo Institute of Technology
http://www.ide.titech.ac.jp/TR

Preface

Bachelor theses of Department of International Development Engineering, Tokyo Institute of Technology were presented successfully on August 4, 2014 and February 27, 2015, respectively. This technical report consists of the abstracts of those theses.

TECHNICAL REPORT OF INTERNATIONAL DEVELOPMENT ENGINEERING
TRIDE-2016-02

TABLE OF CONTENTS

Solvent Extraction of Heterocompounds Contained in Petroleum Heavy Fraction

Student Number: 10-18700 Name: Hironobu HASEGAWA Supervisor: Ryuichi EGASHIRA, Hiroaki HABAKI

1. Introduction

Some heavy fractions produced in the petroleum refinery contain heterocompounds, originating from crude oils. Nitrogen heterocyclic compounds, especially basic nitrogen heterocyclic compounds, were reported to cause degradation of fuel oil quality and catalyst poisoning, and sulfur compounds in fuel oils should result in serious air pollution. Then the removal of these heterocompounds from the fractions was expected to make the catalytic reaction stably operated or improved, keep the quality of fuel oil, and maintain the air environment[1].

Solvent extraction has been utilized as a commercialized method to separate aromatic compounds from petro-derived fractions. Separation of nitrogen heterocyclic compounds by solvent extraction has been studied, in which coal tar absorption oil or catalytic cracked oil was used as feed oil[2][3][4]. However the separation of heterocompounds from the heavy fractions has been insufficiently investigated.

In this study, the solvent extraction was applied to the separation of heterocompounds from heavy fractions generated in the petroleum refinery process, such as light cycle oil (LCO, b.p. 425-631K), coker gas oil (CGO, b.p. 431-660K) and atmospheric residue (AR, b.p. above 633K). Then, the effects of solvent species and operating conditions on the separation of heterocompounds were examined.

2. Experimental

2.1 Analysis

The liquid phases, such as feed oils, were analyzed by gas chromatograph (Shimadzu GC-2010), the chemical luminescence method (JIS-K 2609), ultraviolet fluorescence method (JIS-K 2541-6), potentiometric titration method to determine the compositions of the phases, especially, in terms of total nitrogen, total basic nitrogen, and total sulfur contents.

2.2 Batch Extraction

The experimental conditions of single batch extraction are summarized in **Table 1**. LCO, CGO and AR, obtained from the Middle East, were used as the feed oils from actual fractions in the petroleum refinery. Six kinds of solvents were selected. Sulfolane and furfural are utilized in the commercial extraction processes. Methanol, aqueous solution of acetic acid, xylene and heptane were chosen from the solvents in the research steps. The extract phase obtained from contact of AR and xylene or heptane was also utilized as feed oils, AR1 or AR2, respectively. The specified amounts of feed, R_0, and solvent, E_0, were put in conical flask and shaken at 303K for 48 hours to be equilibrated. After reaching equilibrium conditions, the raffinate and extract phases, R_1 and E_1, were separated into each other with separatory funnel. The experimental conditions by multiple batch extraction with fresh solvent are summarized in **Table 2**. LCO, CGO and AR2 were used as feed oils and methanol was selected as solvent. After phase separation of each extraction, fresh solvent was contacted with the obtained raffinate and repeated for 3 times.

3. Results and Discussion

3.1 Composition of feed oils

The gas chromatogram of AR is shown in **Fig.1**. The AR contained a large number of components and a portion of them might not be detected by GC due to the high boiling points. The periodically appeared sharp peaks on the chromatogram might represent alkane hydrocarbons with the different carbon numbers and the other components, such as, aromatics and heterocompounds, were detected as a lot of tiny peaks between the sharp peaks. The LCO and CGO were also the same. Accordingly, it was difficult to quantitatively determine the compositions of the feed oils. Nitrogen and sulfur contents in feed oils are shown in **Table 3**. Three kinds of feed oil, LCO, CGO and AR contain considerable amount of nitrogen and sulfur. And nitrogen species in LCO are almost non-basic.

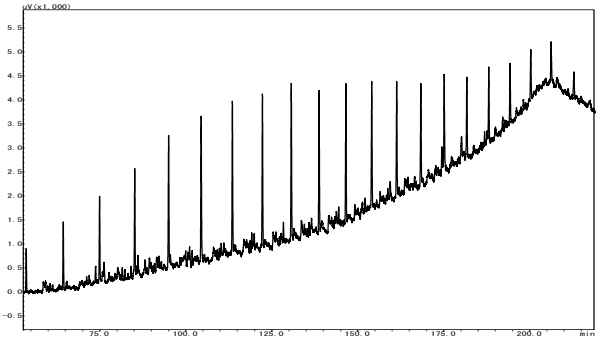

Fig.1 Gas chromatogram of AR

3.2 Definitions

The yield and distribution ratio of component i, Y_i and m_i after k-th extraction are defined as follows:

$$Y_{i,k} = E_k \cdot y_{i,k} / R_{k-1} \cdot x_{i,k-1} \quad (1)$$

$$m_{i,k} = y_{i,k} / x_{i,k} \quad (2)$$

where $y_{i,k}$ and $x_{i,k}$ are the mass fractions of component i in each phases at k-th extraction.

Table1 Experimental conditions of single batch extraction

System		
Feed		LCO, CGO, AR, AR1, AR2
Solvent		Methanol, Sulfolane, Furfural 0.4 Acetic acid, m-Xylene, Heptane
Conditions		
Mass of feed, R_0	[kg]	0.02
Solvent/feed ratio, E_0/R_0	[-]	1(Methanol, Sulfolane, Furfural, 0.4 Acetic acid) 10(m-Xylene or Heptane)
Temperature	[K]	303
Time	[hr]	48

Table2 Experimental conditions of multiple batch extraction

System		
Feed		LCO, CGO, AR2
Solvent		Methanol
Conditions		
Initial mass of feed, R_0	[kg]	0.02
Mass of solvent, E_0	[kg]	0.02(Feed : LCO, CGO)
Solvent/feed ratio, E_0/R_0	[-]	1(Feed : AR2)
Temperature	[K]	303
Time	[hr]	48
Repetition, n	[-]	3

Table 3 Nitrogen and sulfur contents in feed oils

Feed oil	Nitrogen [ppm]	Basic Nitrogen [ppm]	Sulfur [ppm]
LCO	380	17	1600
CGO	730	333	25000
AR	2400	726	38000

3.3 Batch Extraction

In the cases of LCO and CGO feeds, the feed and solvent

formed heterogeneous liquid-liquid two phases. The mixture of AR and xylene formed the homogeneous single phase and that of AR1 and furfural was also homogeneous. It was virtually impossible to sufficiently contact AR with any solvent due to quite low fluidity of AR and the phase separation was impossible as well. The mixture of AR and heptane formed the liquid-solid heterogeneous phases. Heptane acted on as deasphalting agent and asphaltene was obtained as a solid.

The effects of the combination of the feed and solvent on the yields, Y_i, and distribution ratio, m_i, of nitrogen and sulfur are shown in **Figs. 2** and **3**, respectively. In most cases, the nitrogen and sulfur heterocompounds were extracted in the used solvents. The Y_is and m_is of nitrogen were larger with any solvent than those of sulfur. The Y_is and m_is (i = N, S) with furfural solvent were higher than those with the other solvents. The aqueous solution of acetic acid was ineffective to extract both compounds. When AR was contacted with heptane, the solid phase, asphaltene, was obtained and its concentration of nitrogen was 7200ppm, much higher than that in AR, 2400ppm. The yield of nitrogen in the asphaltene, $1 - Y_{N,1}$, was approximately 0.3 and the separation of nitrogen also attained by the deasphalting operation with heptane. The m_is of nitrogen were larger with AR2 feed containing heptane than those with AR1 containing m-xylene. The nitrogen heterocompounds were more extracted in the less polar feed than those in the more polar feed[5].

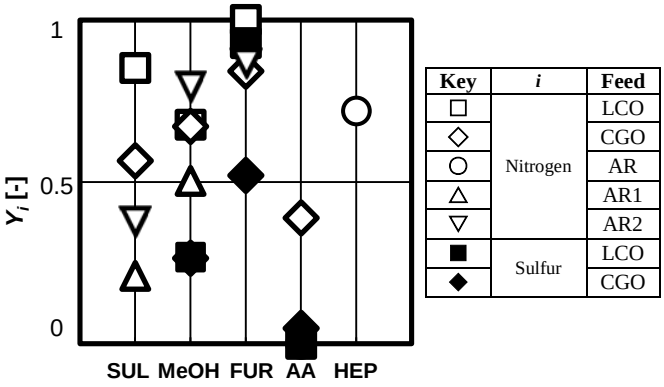

Fig.2 Effects of feed oil and solvent on yield, $Y_{i,1}$, in single batch extraction

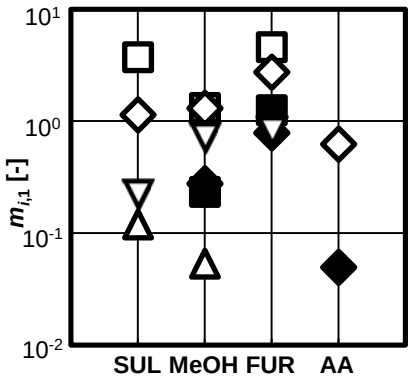

Fig.3 Effects of feed oil and solvent on distribution ratio, $m_{i,1}$, in single batch extraction

The effects of feed on the Y_N and m_N in the multiple batch extraction are shown in **Figs. 4** and **5**, respectively. In any stage of extraction, the nitrogen compounds were extracted. In the cases of LCO and CGO, Y_Ns and m_Ns were kept relatively high until the third stage. On the other hand, in the case of AR2, Y_N and m_N in the second and third stages were much lower than those in the first. The properties of nitrogen compounds contained in AR distributed wider than those in LCO and CGO, since the boiling range of AR was wider, so that the distribution ratios of some parts of nitrogen compounds in AR might be low and difficult to extract into solvent phase.

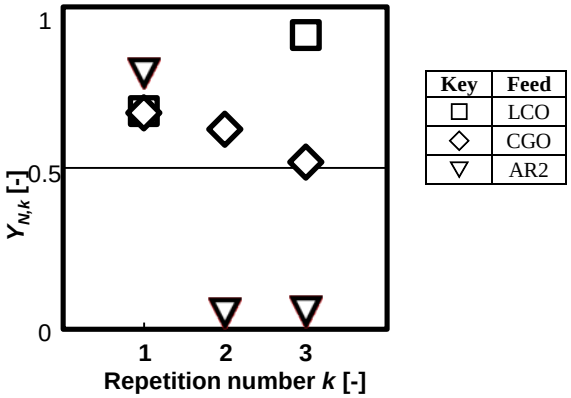

Fig.4 Effects of the kind of feed oil and repetition numbers on yield of nitrogen, $Y_{N,k}$

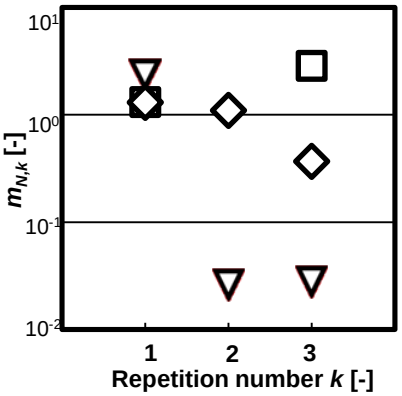

Fig.5 Effects of the kind of feed oil and repetition numbers on distribution ratio of nitrogen, $m_{N,k}$

4. Conclusion

The petroleum heavy fractions contained a large number of components and substantial amount of nitrogen and sulfur. Nitrogen and sulfur heterocompounds in the heavy fractions could be removed by solvent extraction. Some parts of nitrogen heterocompounds in atmospheric residue were difficult to extract.

Nomenclature

R	-Mass of raffinate phase		
E	-Mass of solvent phase		
x_i	-Mass fraction of i in feed phase		
y_i	-Mass fraction of i in solvent phase		
Y_i	-Extraction yield of i		
m_i	-Distribution ratio of i		
LCO	-Light cycle oil	CGO	-Coker gas oil
AR	-Atmospheric residue	FUR	-Furfural
SUL	-Sulfolane	AA	-Acetic acid
MeOH	-Methanol	HEP	-Heptane

Subscript

i	-component i
N	-nitrogen species
k	-at equilibrium state of k-th extraction experiment
0	-at initial state

Reference

[1]石油学会;石油精製プロセス,第五章,接触分解 125-138
[2]Kodera, Y., et al., Fuel, 70, (6) 765 (1991)
[3]Qi, J., et al., Fuel, 77, (4) 255 (1998)
[4]Nagai, M., 東京工業大学 1999年卒業論文
[5]Shimada, Y., et al., J. Chem. Eng. Jpn, 46, (6) 376 (2013)

The impact of urbanization on water utilities performance in a developing country: A case study of the Philippines

Student Number: 09_04820 Name: Shintaro OYA Supervisor: Naoya ABE

1. Introduction

Performance of a water utility can be seen in a wide range of aspects. The International Benchmarking Network for Water and Sanitation Utilities (IBNET) set the first global benchmarking standard for the water and wastewater sector and provides access to the enormous information of water utilities. This information source is relevant for those water utilities in developing countries as they are facing rapid increase of water demand due to the rapid growth of population.

Safe water supply has significant impact on public health. It is getting more important to understand how performance of water utilities in developing countries is affected by urbanization.

2. Objectives

The objectives of this study are: (1) to understand briefly how the performance among water utilities in the Philippines varies and; (2) to assess the impact of urbanization on performance of water utilities.

3. Literature Review

Previous research has discussed the effect of urbanization on urban water. Not technical difficulties but poor management generally causes inferior performance. It is required to focus on the actual conditions and consider how the performance is affected by urbanization. (Hashimoto (2010))

4. Data and Methodology

IBNET provides the information of 52 utilities in the Philippines both in 2004 and in 2009 with a number of indicators, which are represented by Key Performance Indicators (KPIs) such as the amount of nonrevenue water, operational costs, water production, etc. on their reports. In this way, principal Component Analysis (PCA) was conducted in order to convert KPIs into the smaller number of variables.

Urban population, urban population growth rate and urban population rate were selected as proxies to describe urbanization. The demographic data of municipalities and cities where the water utilities are placed was obtained from the Census of the Philippines. Impact of urbanization on the performance of water utilities in each year was examined with the following multiple regression model:

$$PCn = \beta_0 + \beta_1 UP + \beta_2 UPGR + \beta_3 UPR + \varepsilon$$

where PCn is score of the nth principal component (PC); UP is population living in urban areas; UPGR is growth rate of population living in urban areas; UPR is ratio of population living in urban areas against total population; and ε is an error term.

5. Results

KPIs were summarized into four PCs containing approximately 70% of the variance (see Table1). The PCs in 2004 were interpreted as factors respectively describing supply volume, operational efficiency, financial vulnerability and management efficiency. In terms of 2009, PCs show the extent of service efficiency, nonrevenue water issue, management efficiency and operational efficiency.

Table 1. Results of principal component analysis

IBNET Key Performance Indicators	2004				2009			
	PC1	PC2	PC3	PC4	PC1	PC2	PC3	PC4
Water coverage	0.129	-0.072	0.217	-0.259	-0.045	**0.435**	**-0.311**	0.123
Electrical energy cost ratio	-0.054	-0.048	**0.505**	-0.170	0.082	0.176	-0.265	**-0.408**
Nonrevenue water (ratio)	0.063	**0.486**	-0.052	0.220	-0.228	0.263	**0.452**	-0.185
Nonrevenue water (amount)	**0.318**	**0.327**	-0.043	0.224	-0.199	**0.339**	0.279	-0.222
Staff W/1,000 W population served	-0.239	0.087	-0.068	**0.343**	0.178	**-0.381**	0.289	-0.119
Continuity of service	0.131	-0.260	**-0.314**	-0.222	0.014	0.087	0.043	**0.522**
Water sold that is metered	-0.007	**-0.387**	-0.160	**0.349**	-0.185	0.109	0.073	**0.564**
Collection period	-0.032	-0.296	-0.054	**0.500**	0.214	-0.073	**0.445**	0.051
Collection ratio	0.039	**-0.351**	**-0.332**	0.102	0.128	0.009	0.102	0.284
Average revenue W & WW	0.010	0.170	**-0.508**	-0.275	**-0.442**	0.089	0.141	0.027
Operational cost W & WW	-0.177	0.343	**-0.335**	0.029	**-0.381**	-0.141	0.249	0.073
Operating cost coverage	0.157	-0.093	-0.271	**-0.381**	-0.192	**0.331**	-0.187	0.007
Water production	**0.499**	0.192	-0.019	0.170	0.203	**0.407**	**0.346**	-0.122
Total water consumption	**0.513**	-0.059	0.029	0.076	**0.402**	0.297	0.100	0.061
Residential consumption	**0.480**	-0.132	0.071	0.018	**0.437**	0.185	0.069	0.148
standard deviation	1.826	1.665	1.506	1.379	1.947	1.749	1.404	1.318
proportion of variance	0.222	0.185	0.151	0.127	0.253	0.204	0.132	0.116
cumulative proportion	0.222	0.407	0.558	0.685	0.253	0.457	0.588	0.704

W: Water service, WW: Wastewater service

Table2. Results of multiple regression analysis

	2004 (n=38)				2009 (n=19)			
	PC1	PC2	PC3	PC4	PC1	PC2	PC3	PC4
UP	**2.12e-06*** **	**1.00e-06** **		8.45e-07	**-9.89e-07***	**9.42e-07** **		-5.18e-07
UPGR			0.01	**1.31e-02** **	**3.59e-02***			**-3.50e-02*** **
UPR				**-1.15e-02***	**3.21e-02***	**2.88e-02*** **		
Const.	**-0.55***	-0.19	-0.19	0.21	**-2.38***	**-2.28*** **	0.18	**0.82***
Adj-R^2	0.48	0.11	0.044	0.15	0.15	0.66		0.31
F-value	35.1***	5.47**	2.69	3.24**	2.07	18.45***		5.114**

Significant level, *10%, **5%, ***1%

Stepwise method was introduced, and explanatory variables were selected above (see Table2). The results in 2004 show that an increase in urban population had impact on supply volume expanding (PC1) and operational efficiency worsening (PC2). Management efficiency (PC4) was also influenced by urbanization. In terms of 2009, population concentration on urban areas affected nonrevenue water issue getting worse (PC2), and a rise in urban population growth rate had negative impact on the operational efficiency (PC4).

6. Conclusion

From these results, it is concluded that: (1) while integrated components in 2004 showed relatively fundamental factors such as supply volume and financial vulnerability, the PCs in 2009 described efficiency of service, management and operation; (2) although population increase in urban areas had positive impact on performance size in 2004, urbanization had negative impact on efficiencies in both years and nonrevenue water issue has become worse by population concentration on urban areas in 2009.

References

[1] Berg, et al. 2011. *The IBNET Water Supply and Sanitation Performance Blue Book*

[2] Department of economic and social affairs, United Nations. 2014. *2014 revision of the World Urbanization Prospect*

[3] Hashimoto, K. 2010. *Situations in developing countries.* Mizkan water forum archives 2010

NUMERICAL STUDY ON DUST DEVIL-LIKE VORTICES OVER BUILDING ARRAY

Student Number: 11_12787 Name: Takafumi SUEISHI Supervisor: Manabu KANDA

1. Introduction

In daytime of sunny day, vortices called Dust devils occur at arid region like a desert. They are small-scale vortices made by ground heating and visible by dust and other particles. The lifetime is only a few minutes.

The dust devil has been studied based by field observations and numerical simulations. In past numerical studies, dust devil-like vortices (DDVs) were successfully simulated using Large-eddy simulation model. (1) They focused on DDVs over a flat homogeneous field. Recently, DDVs were found also in build-up area. (2) In this study, DDVs were simulated over regular cubic arrays or urban morphology to examine the effects of ground obstacles on the DDVs.

2. Simulation Setup

The study was carried out using PALM (PArallelized LES Model) which was developed in Leibniz University Hannover.

Three simulations were conducted by changing the surface geometry. One has flat surface named “Case Flat”. Another one has cubical array named “Case Topo”. The other has realistic urban geometry in Shinjuku named “Case City”.

The simulation conditions of Case Flat and Case Topo was as follow. The simulation domain was 768m by 768m by 1572m. Grid spacing was 2m except for vertical grid spacing above 800m. No mean background wind was imposed. A constant surface sensible heat flux of 0.24Kms^{-1} were applied. The initial potential temperature was constant at 300K up to 700m and increased at 0.02Km^{-1} above that. Cyclic lateral boundary conditions, no slip conditions at the lower and free boundary conditions at the upper boundary were used.

In Case Topo, a single cube size was 32m by 32m by 32m, and street width was also 32m. A constant surface sensible heat flux of 0.24Kms^{-1} were applied from ground and roof top.

In Case City, the simulation domain was 1000m by 1000m by 1919m. Grid spacing was 2m horizontally and 3m vertically except for vertical grid spacing above 1080m. Heat flux was calculated by LOCALS-UCSS which is developed by Ashie et al (2011). Radiation at Shinjuku on 5 August 2014 at 12:00 was considered in this model and the result was used as PALM heat flux input.

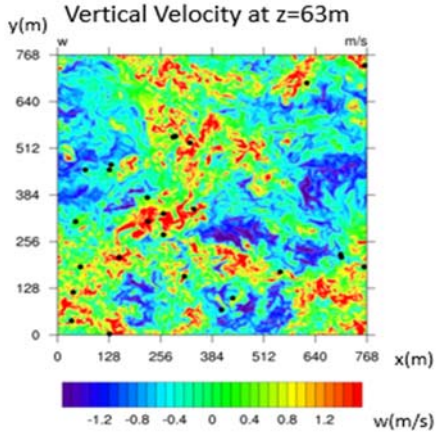

Figure 1. Horizontal cross section of vertical velocity w for Case Topo at z=63m, t=5045s.

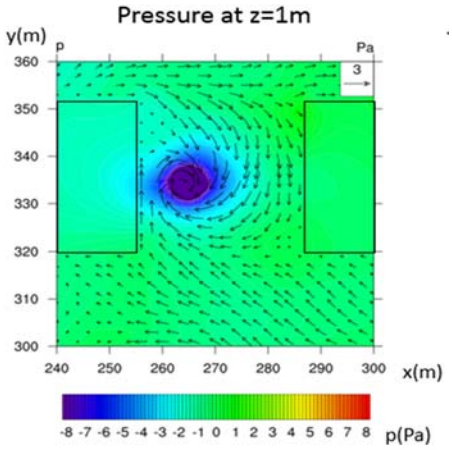

Figure 2. Perturbation pressure contour and horizontal velocity near DDV.

Vortex centers were determined by using perturbation pressure and vorticity as follow. (1)

(1) $p < -4.0\mathrm{Pa}$

(2) $|\zeta| > 1.0s^{-1}$

(3) $|\zeta|$ should be local maximum.

Where p is the perturbation pressure. ζ is vertical vorticity, and it is defined as follow.

$$\frac{\partial \zeta}{\partial t} = \frac{\partial v}{\partial x} - \frac{\partial u}{\partial y} \qquad (1)$$

Where x and y represent horizontal axis of Cartesian coordinates, and u and v are the corresponding horizontal velocity components.

3. Results

Figure 1 shows that horizontal cross section of vertical velocity w for Case Topo at z = 63m, t = 5045s.

Figure 1 demonstrates that there were some convergence lines. These convergence lines formed a part of spoke-like pattern. Most of DDVs were on convergence lines. These observations agree well with Case Flat or previous study. (1) However DDVs occurred not only from convergence lines but also from edge of buildings.

Figure 2 shows that flow structure near strongest DDV in Case Topo. Contour shows perturbation pressure, and black vectors show horizontal velocity. Black rectangles show the position of buildings.

The diameter of DDV is about 20m. Near the DDV center, perturbation pressure was decreased. Absolute value of vorticity was increased, and updraft also occurred.

There were 5.43 DDVs in Case Flat and 18.60 DDVs in Case Topo on average.

Figure 3 shows that the relationship between distance from DDV center and tangential velocity for time averaged vortices for strongest DDVs in Case Flat and Case Topo. These data were time averaged over t = 4800s ~ 4900s for Case Flat, t = 5006s ~ 5053s for Case Topo.

Figure 3 demonstrates that tangential velocity becomes the pick at about 4m from DDV center. In Rankin's model, this relationship is represented as follow.

$$v = \begin{cases} \dfrac{rK}{r_0^{\,2}} & (o < r \le r_0) \\ \dfrac{K}{r} & (r_0 < r) \end{cases} \qquad (2)$$

Where v is tangential velocity, r is distance from DDV center, r_0 is radius of forced vortex, K is constant respectively. The form of tangential velocity was similar to Rankin's model, so the radius of forced vortex became about 4m. Tangential velocity of Case Topo's DDV was less than that of Case Flat.

In Case City, there were less heat flux than that of Case Flat and Case Topo.

Figure 4 shows that positions of DDVs in Case City. These DDVs were found in 300 time steps. Contour shows the building height and black points show the positions of DDVs.

From Figure 4, DDVs occurred near high buildings. This is because there were winds caused by buildings. These winds helped making DDVs. DDV positions also needed to be on convergence lines, the same as Case Flat and Case Topo. But DDVs need some spaces to develop bigger. So there were not DDVs high dense area at north-east part and south-west part in Case City domain.

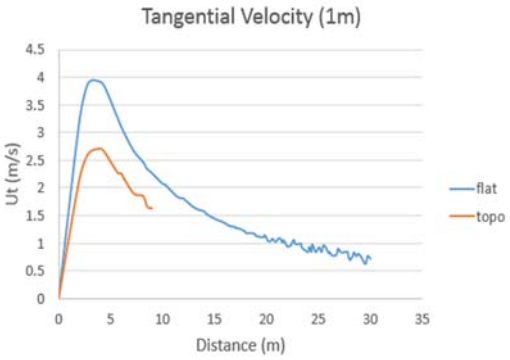

Figure 3. Relationship between distance from DDV center and tangential velocity.

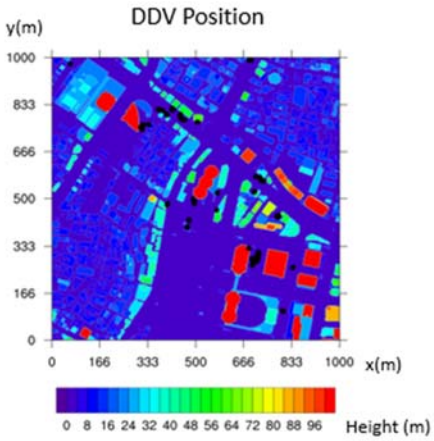

Figure 4. Building height contour and DDV positions in Case City.

4. Conclusion

From 3 simulations, we can get summary as follow.

(1) DDVs developed on convergence lines.

(2) Buildings helped DDV to grow up by edge effect and winds caused by buildings.

(3) Comparing Case Flat and Case Topo, Case Topo's number of DDVs were much than that of Case Flat. But, the strength of Case Topo was weaker than that of Case Flat.

(4) Flow structure of Case Flat's DDV and that of Case Topo had similarity. These can be explained by using Rankin model.

5. Reference

[1] S.Raasch and T.France (2011), Structure and Formation of Dust Devil-Like Vortices in the Atmospheric Boundary Layer: A High-Resolution Numerical Study

[2] Fujiyoshi Y, Yamashita K, Fujiwara C (2009), Detection of Organized Airflow in the Atmospheric Boundary Layer and the Free Atmosphere Using a 3D-Scanning Coherent Doppler Lidar

[3] Ashie Y, Kono T (2011), Urban-Scale CFD Analysis in Support of a Climate-Sensitive Design for the Tokyo Bay Area

Improvement of Fisher linear discriminant based on normal distribution

Student ID number: 10-15305 Full name： CUNG Van Dung Supervisor： Yukihiko YAMASHITA

1 Introduction

Fisher linear discriminant analysis is not optimal for class separation even assuming a normal distribution. To solve this problem, Yokota et al. proposed an iterative method based on Chernoff or Bhattachyya distance for binany class problem. Its equation is given by a generalized eigenvalue problem with a correction term. In the case of multi-class problem, it is necessary to extend this theory. Unfortunately, since the evaluation function becomes complicated, it is not possible to obtain a simple formula. Therefore, in this study, i propose a method to obtain approximated solution based on a correction term. I showed its advantage by experiment.

2 Fisher linear discriminant

Let $\boldsymbol{\mu}_c$ be the average of pattern in class C ($c = 1, 2, \ldots, C$), and let $\boldsymbol{\Sigma}_c$ be the variance-covariance matrix . $E_{\boldsymbol{\xi}\in\Omega_c} f(\boldsymbol{\xi})$ indicates the expected value of $f(\boldsymbol{\xi})$. We have

$$\boldsymbol{\mu}_c = E_{\boldsymbol{\xi}\in\Omega_c}\boldsymbol{\xi}, \tag{1}$$

$$\boldsymbol{\Sigma}_c = E_{\boldsymbol{\xi}\in\Omega_c}(\boldsymbol{\xi}-\boldsymbol{\mu}_c)(\boldsymbol{\xi}-\boldsymbol{\mu}_c)^T. \tag{2}$$

The feature value is given by the inner product of the feature extraction vector $\boldsymbol{v}$ and a pattern. The mean of feature value in class c m_c is given by

$$m_c = E_{\boldsymbol{\xi}\in\Omega_c}\langle \boldsymbol{v}, \boldsymbol{\xi}\rangle = \langle \boldsymbol{v}, \boldsymbol{\mu}_c\rangle. \tag{3}$$

The inter-class covariance matrix $\boldsymbol{\Sigma}_{\mathrm{B}}$ is given by

$$\boldsymbol{\Sigma}_{\mathrm{B}} = \sum_{k=1}^{C}\sum_{l=k+1}^{C}(\boldsymbol{\mu}_k-\boldsymbol{\mu}_l)(\boldsymbol{\mu}_k-\boldsymbol{\mu}_l)^T. \tag{4}$$

The inter-class variance of feature value is given by

$$\sum_{k=1}^{C}\sum_{l=k+1}^{C}(m_k-m_l)^2 = \langle \boldsymbol{v}, \boldsymbol{\Sigma}_B\boldsymbol{v}\rangle. \tag{5}$$

The variance of feature value in class c is given by

$$E_{\boldsymbol{\xi}\in\Omega_c}(\langle \boldsymbol{v}, \boldsymbol{\xi}\rangle - m_c)^2 = \langle \boldsymbol{v}, \boldsymbol{\Sigma}_c\boldsymbol{v}\rangle. \tag{6}$$

The sum of the variance-covariance matrices of patterns $\boldsymbol{\Sigma}_{\mathrm{W}}$ is given by

$$\boldsymbol{\Sigma}_{\mathrm{W}} = \sum_{c=1}^{C}\boldsymbol{\Sigma}_c. \tag{7}$$

The sum of variances of feature values is given by

$$\langle \boldsymbol{v}, \boldsymbol{\Sigma}_{\mathrm{W}}\boldsymbol{v}\rangle. \tag{8}$$

Fisher linear discriminant is defined as maximizing the following ratio with respect to $\boldsymbol{v}$.

$$J_{\mathrm{F}} = \frac{\langle \boldsymbol{v}, \boldsymbol{\Sigma}_{\mathrm{B}}\boldsymbol{v}\rangle}{\langle \boldsymbol{v}, \boldsymbol{\Sigma}_{\mathrm{W}}\boldsymbol{v}\rangle}. \tag{9}$$

This problem can be solved by the following generalized eigenvalue problem .

$$\boldsymbol{\Sigma}_{\mathrm{B}}\boldsymbol{v} = \lambda\boldsymbol{\Sigma}_{\mathrm{W}}\boldsymbol{v}. \tag{10}$$

3 Correction term by Bhattacharyya distance

Error rate of recognition of distributions is given by

$$e = 1 - \frac{1}{C}\sum_{k=1}^{C}\int_{\{\boldsymbol{x}|p_k f_k(\boldsymbol{x})=\max p_i f_i(\boldsymbol{x})} p_k f_k(\boldsymbol{x})d\boldsymbol{x}, \tag{11}$$

where p_k is the probability of category Ω_k and $f_k(\boldsymbol{x})$ is the probability density function of pattern in category Ω_k.

For two probability density functions $f_1(\boldsymbol{x})$ and $f_2(\boldsymbol{x})$, Chernoff distance is given by

$$d_{\mathrm{C}} \equiv -\log\int_{R^D}\left(f_1(\boldsymbol{x})\right)^{\alpha}\left(f_2(\boldsymbol{x})\right)^{1-\alpha}d\boldsymbol{x}. \tag{12}$$

In particular, when $\alpha = 1/2$, it is called the Bhattacharyya distance. Assume that $f_1(\boldsymbol{x})$, and $f_2(\boldsymbol{x})$ are the probability density functions of the normal distributions of which means and variances are m_1 and S_1, and m_2 and S_2, respectively. Chernoff coefficient $J_{\mathrm{C}} \equiv e^{-d_{\mathrm{C}}}$ is given by

$$J_{\mathrm{C}} = \sqrt{\frac{|\boldsymbol{S}_1|^{1-\alpha}|\boldsymbol{S}_2|^{\alpha}}{|(1-\alpha)\boldsymbol{S}_1+\alpha\boldsymbol{S}_2|}}\exp\left(-\frac{1}{2}\langle \boldsymbol{m}_1-\boldsymbol{m}_2, \alpha(1-\alpha)\left((1-\alpha)\boldsymbol{S}_1+\alpha\boldsymbol{S}_2\right)^{-1}(\boldsymbol{m}_1-\boldsymbol{m}_2)\rangle\right). \tag{13}$$

I obtain K feature extracting vectors $\boldsymbol{v}_1, \boldsymbol{v}_2, \ldots, \boldsymbol{v}_K$. The feature extraction matrix $\boldsymbol{V}$ is given by

$$\boldsymbol{V} = (\boldsymbol{v}_1\boldsymbol{v}_2\ldots\boldsymbol{v}_K). \tag{14}$$

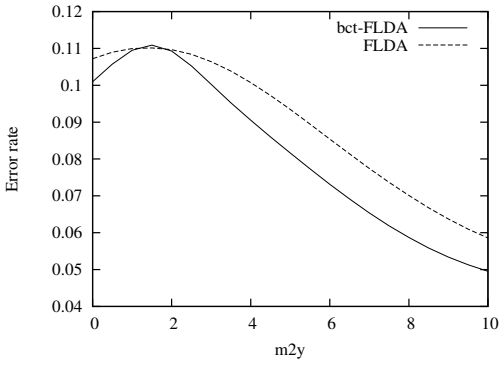

(a) Error rate ($\sigma_{2y}^2 = 8$)

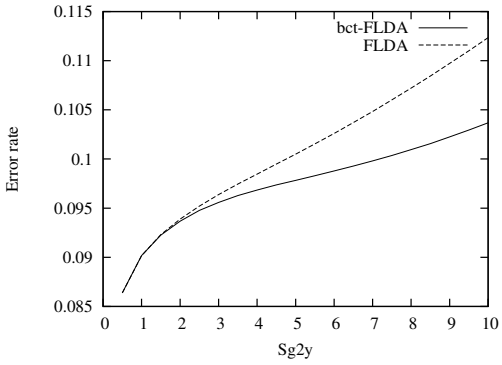

(b) Error rate ($\boldsymbol{\mu}_{2y} = 0$)

Figure 1: Classification of 3-dimensionalnormal distributions by best division

For recognition, the distance of distributions should be large. The sum of the Bhattacharyya coefficients is given by

$$J_{\mathrm{B}} = \sum_{k=1}^{C} \sum_{l=k+1}^{C} \sqrt{\frac{2\sqrt{|\boldsymbol{S}_k||\boldsymbol{S}_l|}}{|\boldsymbol{S}_k + \boldsymbol{S}_l|}} \exp\left(-\frac{1}{4} \langle m_k - m_l, (\boldsymbol{S}_k + \boldsymbol{S}_l)^{-1}(m_k - m_l)\rangle\right) \quad (15)$$

Therefore, by minimizing J_{B} with respect to $\boldsymbol{V}$, it is possible to determine the feature extraction matrix $\boldsymbol{V}$. However, minimization of eq (15) is difficult. Therefore I solve this problem approximately based on the iterative method for binary class and one feature extraction vector. I call this method the Bhattacharyya correction term Fisher linear discriminant analysis (bct-FLDA). Let $\boldsymbol{v}_1^{(n)}, \boldsymbol{v}_2^{(n)}, \ldots, \boldsymbol{v}_N^{(n)}$ be feature extraction vectors at n-th iteration. The feature extraction matrix $\boldsymbol{V}^{(n)}$ is expressed by

$$\boldsymbol{V}^{(n)} = (\boldsymbol{v}_1^{(n)} \boldsymbol{v}_2^{(n)} \ldots \boldsymbol{v}_K^{(n)}). \quad (16)$$

The generalized eigenvalue problem to be solved is given by

$$\left(\boldsymbol{\Sigma}_{\mathrm{B}} - \sum_{c=1}^{C} \frac{\boldsymbol{\Sigma}_c}{\langle \boldsymbol{v}^{(n)}, \boldsymbol{\Sigma}_c \boldsymbol{v}^{(n)} \rangle}\right) \boldsymbol{v}^{(n+1)} = \lambda \boldsymbol{\Sigma}_{\mathrm{W}} \boldsymbol{v}^{(n+1)}. \quad (17)$$

I denote eigenvectors in descending order of the eigenvalues as $\boldsymbol{v}_1^{(n+1)}, \boldsymbol{v}_2^{(n+1)}, \ldots, \boldsymbol{v}_N^{(n+1)}$. They are feature extraction vectors obtained at the n-th computation. The initial vectors of this iterative calculation were set to feature extraction vectors of FLDA. The process is repeated until convergence.

4 Experiment

In this experiment, three three-dimensional normal distributions are recognized. I extracted two feature extration vectors.

$$\mu_1 = \begin{pmatrix} 0 \\ 0 \\ 0 \end{pmatrix}, \quad \boldsymbol{\Sigma}_1 = \begin{pmatrix} 1 & 0 & 0 \\ 0 & 1 & 0 \\ 0 & 0 & 1 \end{pmatrix}$$

$$\mu_2 = \begin{pmatrix} 3 \\ \mu_{2y} \\ 0 \end{pmatrix}, \quad \boldsymbol{\Sigma}_2 = \begin{pmatrix} 1 & 0 & 0 \\ 0 & \sigma_{2y}^2 & 0 \\ 0 & 0 & 1 \end{pmatrix}$$

$$\mu_3 = \begin{pmatrix} 0 \\ 3 \\ 1 \end{pmatrix}, \quad \boldsymbol{\Sigma}_3 = \begin{pmatrix} 1 & 0 & 0 \\ 0 & 1 & 0 \\ 0 & 0 & 8 \end{pmatrix}$$

Figure 1 (a) shows error rates when σ_{2y}^2 is 8 and μ_{2y} is changed from 0 to 10. Figure 1 (b) shows error rates when μ_{2y} is 0 and σ_{2y}^2 is changed from 0.5 to 10. From Figure 1 (a), we can see around $\mu_{2y} = 1.7$ both error rates are maximum and they are almost the same. In other region bct-FLDA outperforms FLDA clearly. From Figure 1 (b), we can see bct-FLDA outperforms FLDA clearly for $\sigma_{2y}^2 >= 2$. As increasing σ_{2y}^2, the difference becames larger. In addition, the iteration in calculation of bct-FLDA was converged in several times.

5 Conclusions

I proposed a new feature extraction method based on FLDA and Bhattacharyya distance. It provided a correction term to the generalized eigenvalue problem. I showed its advantage by recognition of three three-dimensional normal distributions. For future works, it is necessary to analyze the obtained approximated solution and apply the proposed method to real problems.

References

[1] R.A.Fisher,"The use of multiple measurements in taxonomic problems,"Annals of Eugenics, vol.7, no.2, pp.179-188, 1936.

[2] Yokota Tatsuya, Wakahara Toru, Sakano Hitoshi, Yamashita Yukihiko "Correction Term of Fisher Discriminant Analysis Based on Normal Distribution", IEICE Technical report. PRMU, vol.112, no.495, pp.31-36, 2013.

[3] M. Loog and R.P.W.Duin,"Linear dimensionality reduction via a heteroscedastic extension of Ida: The chernoff criterion,"IEEE Trans. Patter Anal. Mach. Intel., vol.26, no.6, pp.732-739, 2004.

インドネシアの国内航空市場における直行便と乗継便の経路選択分析

学籍番号：11_08455　　氏名：姜　佳文　　指導教員：花岡　伸也

1　はじめに

インドネシアは東西に非常に長く、約 13,000 の島を抱える国であるゆえに、航空輸送は重要な役割を果たしている。しかし、ほとんどの大規模空港の容量が不足している。特に、ジャカルタのスカルノハッタ空港は処理能力の 2 倍以上の旅客数が利用し、非常に混雑している。

スカルノハッタ空港の混雑を解消するため、インドネシア東部にあるマカッサル空港を、本格的なハブ空港として活用するハブ・アンド・スポーク・システムが考えられている。しかし、新しいシステムでは、地方空港への中型機による直行便を減らし、大型機でマカッサル空港に行き、そこから小型機で地方空港に行く乗継便を増やす必要がある。そこで、インドネシア国内の航空利用者について以下の 2 点を明らかにする必要がある。（1）旅客が直行便と乗継便を選択する理由、（2）フルサービスキャリア(FSC)とローコストキャリア(LCC)利用者が経路選択で考慮する要因に違いがあるかどうか。

したがって、本研究の目的は、FSC のガルーダ・インドネシア航空（以下 GA）と LCC のライオンエア（以下 JT）に対し、利用者属性分析を行い、また選好調査を用いて航空経路選択モデル（直行便/乗継便）を構築し、経路を選択する際に重視する選択要因を明らかにする。

2　現地調査

インドネシア国内の航空利用者が航空会社と経路を選択する際の優先事項を明らかにするため、2014 年 7 月にジャカルタとマカッサルの空港で 12 日間のアンケート調査を行った。有効サンプル数 3079 の内、直行便サンプル数が 1,998 で、乗継便サンプル数が 1,081 である。

調査対象路線はジャカルタ発東インドネシア行きの路線の中で、GA と JT が直行便と乗継便（マカッサル経由）を提供する 6 路線である。目的地は Kendari、Palu,、Gorontalo、 Manado、 Ambon と Jayapura である。

調査票では個人属性（性別、年齢、住所、職業、同居者数、世帯月収）、便名と目的地、昨年の旅行経験数、旅行目的、経路決定者、支払運賃、航空券購入手段、マイレージプログラム、航空会社の選択理由、経路の選択理由及び別の経路を選択しなかった理由の、全部で 11 問である。

3　利用者属性分析

現地調査データ全体で見ると、旅客が経路を選択するとき、適切な出発と到着の時間帯を重視する傾向がある。航空会社の選択理由では、GA 旅客が時間帯と安全性を重視し、JT 旅客が低運賃を重視する傾向がある。

次に、航空会社別の旅客特性を詳しく分析した。両社の利用者の中で、JT の 20 歳以下の旅客の割合は GA の 2 倍の 16%であり、若い年齢層が JT を好む傾向が見える。世帯月収では、3 milIDR (約 2.8 万円)以下の利用者の割合は GA が 16%で、JT が 31%である。GA の 3 milIDR~10 milIDR (約 9.3 万円) の利用者の割合は約 7 割で、JT は約 5 割である。世帯月収が 20 milIDR (約 18.6 万円)を超える利用者の割合は GA が 3%で、JT が 5%である。旅行目的は顕著な差はなく、両社ともビジネス旅客が 3 割以上占めている。航空券の購入手段として、旅行代理店で購入する利用者の割合は GA が 7 割以上で、JT が約 6 割である。インターネットで購入する利用者の割合は GA が 18%で、JT が 26%である。マイレージプログラムの加入者の割合は GA が 31%で、JT が 16%である。日本と違って、インドネシアの航空利用者の多くはマイレージプログラムに加入していないことがわかった。昨年の旅行経験数が 1 回以下の利用者の割合は GA が 24%で、JT が 32%である。2~3 回の利用者の割合は GA が 46%に対して、JT が 35%である。6 回以上の利用者の割合は GA が 10%で、JT が 17%である。

また、各路線においての利用者属性の分析も行った。たとえば、Jayapura 行きの長距離路線で、直行便利用者が出発時刻と到着時刻を重視し、乗継便利用者は安い運賃を重視する傾向がある。Ambon 行きの短距離路線では、ある乗継便の到着時間が朝の 7 時半であるので、ビジネス客の割合は全体平均を上回っている傾向がある。そのほかの利用者の多くは満席で直行便を購入できないため、仕方なく乗継便を選択していたことがわかった。

4　選好調査

業務目的と非業務目的の旅客が利用する航空経路を選択する際に重視する選択要因を明らかにするため、2015 年 1 月下旬に航空利用経験があるジャカルタ市民を対象にインターネット調査を行い、有効サンプル数 362 を収集した。

現地調査の各路線の利用者属性の分析結果を踏まえて、選好調査の対象路線は Jayapura、Palu、Ambon、Manado で、それぞれに対して調査票 1 式を設定した。選好調査では GA と JT の直行便・乗継便の合計 4 つの選択肢を提供し、回答者にそれぞれ業務目的と非業務目的での選好順位を

答えてもらった(業務目的旅行では雇用者が運賃を支払う設定とした)。選択肢を構成する属性は運賃、頻度、総時間（乗継時間含む）である。それぞれのレベルは現地調査データの分析を踏まえて、3 つずつに設定した。直交法を用い、シナリオ数を 729 から 36 に減らし、ランダムに 4 つのブロックに配分した。よって、一式の調査票につき 9 つシナリオに対して選択順位をつける必要がある。

より現実に近い航空経路選択モデルが構築されるよう、選好調査の回答者の性別、年齢と収入の各層の割合はインドネシアの人口統計データおよび現地調査の集計結果に基づき設定した。選好調査の回答者の中、自営業が 4 割占めている。また、昨年の旅行経験数が 3 回以下の回答者が 85%である。

5　航空経路選択モデル

本研究では順位付けデータを独立な選択データに分解し、交通分野で多用されているロジットモデルを用いて尤度関数を計算した。本研究ではランクロジットモデルを用いた。表 1 と表 2 は業務旅行、非業務旅行の航空経路選択モデル推定結果である。

表 1　業務旅行航空経路選択モデル推定結果

分析対象	全体		自営業のみ	
説明変数	推定値	t 値	推定値	t 値
運賃　(milIDR)	-	-	-0.255	-0.929
頻度（便数/週）	0.080	1.404	-	-
総時間　(h)	-0.574	-5.757**	-0.328	-1.603
定数 1（GA 直行）	0.680	3.405**	0.729	1.515
定数 2（JT 直行）	1.248	6.455**	1.533	3.676**
定数 3　(GA 乗継）	1.215	14.761**	0.896	5.079**
修正済尤度比	0.238		0.190	
サンプル数	362		80	

（*：5%有意水準　**：1%有意水準）

業務旅行航空経路の選択では、分析対象が有効サンプル全体と自営業サンプルのみの 2 通りの推定になる。選好調査データの基礎集計では、収入に関係なく、GA 直行便を 1 位に選択した回答者の割合が最も多い。したがって、運賃の推定値の符号がプラスになってしまうため、全体推定では運賃以外の説明変数で推定を行った。また、自営業の場合は業務旅行であっても自分で運賃を支払うことになるので、自営業のみのサンプルで推定するときは、運賃を説明変数として設定した。全体の推定では、総時間は符号がプラスで、t 値も 1%有意なことから、最も重要な選択要因である。自営業のみの推定では、運賃と総時間の符号がマイナスで、増加すると効用が下るという妥当な結果となっている。修正済尤度比は推定したモデルが選択結果に対する適合性を表す基準であり、0.2 以上の場合は信頼できるモデルと言える。

表 2　非業務旅行航空経路選択モデル推定結果

分析対象	全体			
説明変数	推定値	t 値	推定値	t 値
運賃　(milIDR)	-0.475	-3.364**	-0.465	-3.320**
頻度（便数/週）	-0.039	-0.651	-	-
総時間　(h)	-0.390	-4.090**	-0.385	-4.056**
定数 1（GA 直行）	-1.208	-5.507**	-1.207	-5.502**
定数 2（JT 直行）	0.402	2.126*	0.427	2.299*
定数 3　(GA 乗継）	0.901	11.412**	0.891	11.565**
修正済尤度比	0.248		0.248	
時間価値	7763 yen/h		7725 yen/h	
サンプル数	362			

（*：5%有意水準　**：1%有意水準）

非業務旅行航空経路の選択では、頻度の符号がマイナスになってしまうため、頻度を含む、含まないの 2 通りの推定をした。2 通りの推定の中、運賃と総時間の符号がマイナスで、t 値は 1%有意になっているので、重要な選択要因である。修正済尤度比は両方とも 0.2 以上になっており、推定結果が信頼できることを示した。ただし、時間価値が非常に高い。選好調査のデザインで、直行便の運賃はウェブ運賃に従っているが、乗継便の基準運賃をウェブ運賃の 8 割に相当する運賃に設定したことが、原因の一つと考えられる。

6　結論

本研究ではインドネシア国内の航空利用者を対象に、現地調査データで直行便と乗継便の利用者属性の分析を行い、選好調査データで業務目的と非業務目的旅行の航空経路選択モデルを構築し、旅客が航空経路を選択する際に考慮する選択要因を明らかにした。修正済尤度比が高く、サンプル比率が実態と一致しているため、モデルの説明力があると判断できる。ただし、推定モデルでは頻度の重要性が低いため、今後選好調査データと現地調査データを統合する推定を行い、頻度の重要性を再検討する必要がある。

参考文献

交通工学研究会編 : やさしい非集計分析, 丸善出版株式会社, 2001

Relation between Wind Velocity, Rotation Speed and Torque of Drag Type Wind Turbine for Small Wind Power Generation

Student Number: 09_16176 Name:Yusuke Tokuda Supervisor: Kunio Takahashi

1. Introduction

In recent years, electric power generation using renewable energy including wind power generation has attracted considerable attention throughout the world due to exhaustion of fuel, and environmental issue. Besides of large scale plants, small scale wind power generation operating at low wind at the living environment has also attracted attention. Since this scale of generation is instability, it is therefore necessary to track for maximum power point. As shown in Fig. 1, the efficiency of the wind power generation is determined by the efficiency of the wind turbine, the generator and the storage circuit. As related researches, the efficiency the storage circuit, i.e. maximum power point tracking, has already been studied [1], and that of the generator is currently under consideration.

In this study, a wind power generation at the living environment, i.e. wind velocity of 3-5m/s. Within this wind range, drag type wind turbine can gain higher power coefficient than lift type wind turbine [2], and doesn't require starting torque. Whereas, lifting power of the wind turbine drastically decreases [3]. Therefore, drag type wind turbine is more efficient than lift type wind turbine.

The purpose of this study is to investigate the relation between the rotation speed, torque of drag type wind turbine and the wind velocity for small wind power generation at low wind (3-5m/s) experimentally.

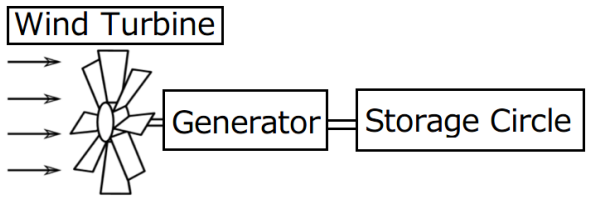

Fig.1 wind power generation system model

2. Experiment

2.1 Experimental tools

To investigate effects of projected area of the wind turbine's blades on its torque, several turbines of different number of blades (the blades have the same shape and size) are fabricated (Fig.2).

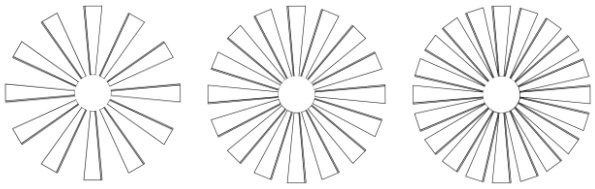

Fig.2 wind turbine design

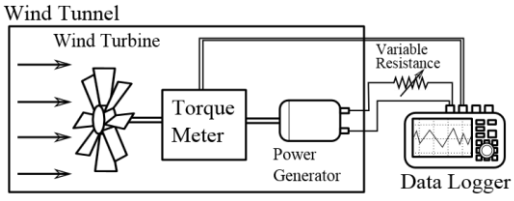

Fig.3 experimental apparatus

The experiment is conducted in a wind-tunnel, which can control wind velocity in the range of 2-5m/s, as shown in Fig.3. The torque and the rotation speed of the wind turbine are adjusted by a variable load resistor connected to the power generator. The torque and the rotation speed are measured by a torque meter (UTM Ⅱ; torque range up to 0.05Nm) for some certain resistance, wind velocities, and blade number, as shown in table 1. Each measurement is repeated twice with times interval of ten seconds.

Table 1. Experimental parameters

blade number	2,3,4,8,12,16,20
wind velocity [m/s] U	5, 4.7, 4.5, 4.2, 4, 3.7, 3.5, 3.2
Resistance [kΩ] R	10, 7, 5, 4, 3, 2.5, 1.5, 1, 0.9, 0.8, 0.7, 0.6, 0.5, 0.45, 0.4, 0.35, 0.3, 0.25, 0.1, 0.05, 0.03, 0.01, 0.0003, 0.0001

2.2 Experimental Results

The measurement results of the torque and the rotation speed of the turbine are obtained as Fig.4. Fig. 4(a) shows the relation between the torque and the rotation speed for several wind speed. Fig. 4(b) shows the relation between the torque and the rotation speed for several load resistances. Fig. 4(c) shows the relation between the rotation speed and the wind speed for several load resistances.

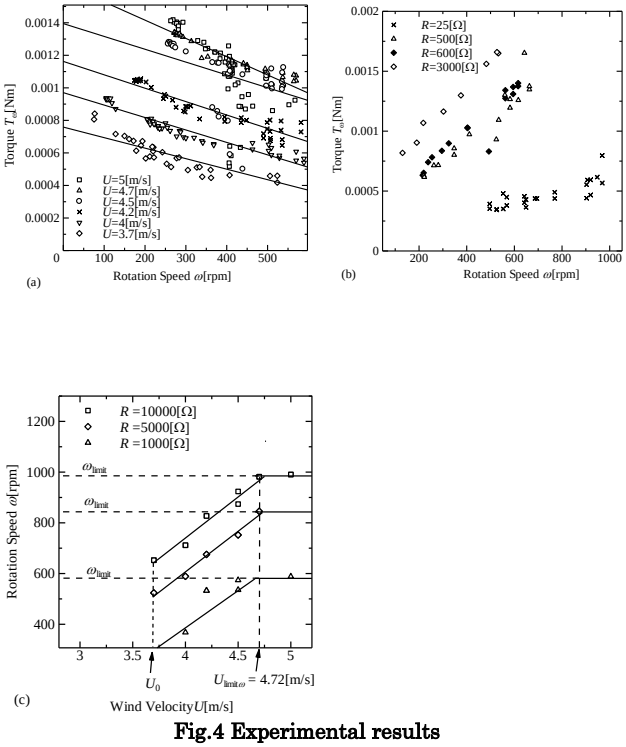

Fig.4 Experimental results

3. Discussions

3.1 Relation between torque and rotation speed

The relation between the torque and the rotation speed has a linear tendency, as shown in Fig. 4(a), whereas, that shown in Fig. 4(b) doesn't. Therefore, from Fig. 4(a), the torque and the rotation speed are assumed having a relation as eq. (1),

$$T_\omega = k(U)\omega(U,R) + C(U) \quad (1)$$

where, the slope $k(U)$ and the intercept $C(U)$ are considered as functions of the wind velocity.

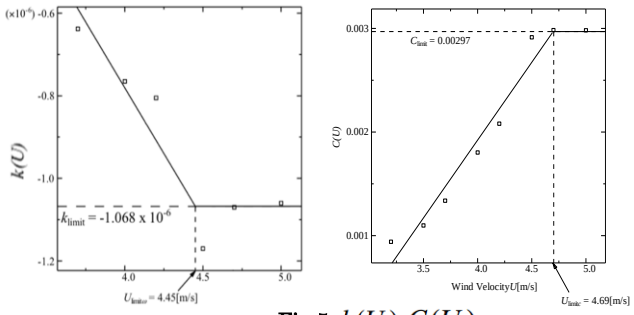

Fig.5 $k(U)$ $C(U)$

The slope $k(U)$ and $C(U)$ the intercept of eq. (1) are obtained by applying least-squares method, as shown in Fig. 5. Both $k(U)$ and $C(U)$ have linear relation before a certain point, and constant after the certain point. We call this certain point as $U_{\text{limit\_k}}$ and $U_{\text{limit\_c}}$. Therefore, their relation can be described as

$$k(U)=\begin{cases} k_k U + C_k \,(U < U_{\text{limit\_k}}) \\ k_{\text{limit}}\,(U_{\text{limit\_k}} \le U) \end{cases} \tag{2}$$

$$C(U)=\begin{cases} k_c U + C_c \,(U < U_{\text{limit\_c}}) \\ C_{\text{limit}}\,(U_{\text{limit\_c}} \le U) \end{cases} \tag{3}$$

where k_k, C_k, k_c, C_c are estimated from experimental results.

3.2 Relation between rotation speed and wind velocity

From the measurement result shown in Fig. 4(c), the relation between the rotation speed and wind velocity is estimated as eq. (4),

$$\omega(U,R)=\begin{cases} 0\,(U \le U_0) \\ k_\omega U - C_\omega\,(U_o < U < U_{\text{limit}\_\omega}) \\ \omega_{\text{limit}}\,(U_{\text{limit}\_\omega} \le U) \end{cases} \tag{4}$$

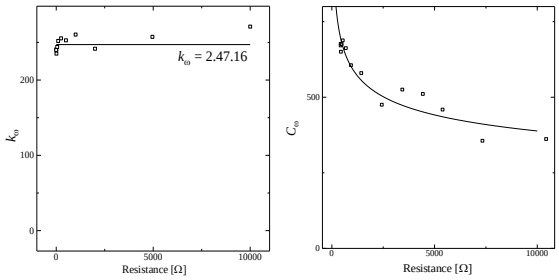

Fig.6 k_ω C_ω

By applying least-squares method, k_ω is obtained as a constant value, as shown Fig.6. As the same manner, by applying least-squares method, C_ω can be estimated as a function of resistance as

$$C_\omega = k_{C_\omega} R^n \tag{5}$$

where $k_{C\omega}$ is estimated from experimental result.
Finally, the rotation speed, wind velocity and resistance are obtained as the following relation.

$$\omega(U,R)=\begin{cases} 0\,(U \le U_0) \\ k_\omega U - k_{C\omega} R^n (U_o < U < U_{\text{limit}}) \\ \omega_{\text{limit}}\,(U_{\text{limit}} \le U) \end{cases} \tag{6}$$

Equation (6) can predict the torque by 7 parameter $k_\omega, k_{C\omega}, k_k, C_k, k_c, C_c, n$ which are estimated from experimental results.

3.3 Comparison of Estimated and Measured value

The output of the wind turbine obtained from experimental values is compared to eq. (6). As shown in Fig. 7, they are qualitatively matched, especially at the vicinity of the maximum point of the power.

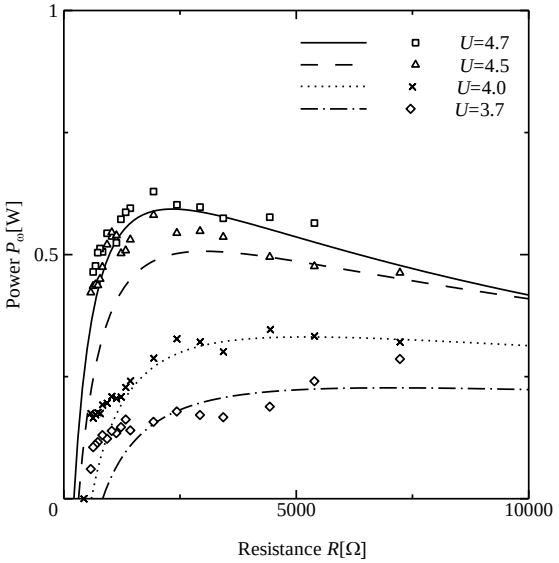

Fig.7 resistance and wind mill output

3.4 Control criteria

When the wind turbine output is at maximum point, resistance $R_{\max}$ is

$$R_{\max} = \left(-\frac{k_C U + C_C}{2k_{Cw}(k_k U + C_k)} - \frac{k_w U}{k_{cw}}\right)^{\frac{1}{n}} \tag{7}$$

Therefore, eq. (7) suggests a possibility of control criteria for maximum power point tracking by measuring the resistance and the rotation speed, as shown in Fig. 8.

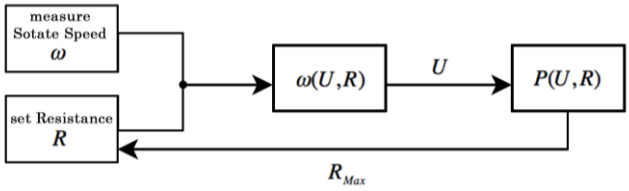

Fig.8 control system

4.Conclusion

- A specific of drag type wind turbine is derived from 8 experimental values.
- The windmill output is obtained by wind velocity and resistance.
- we suggest possibility that maximum power point tracking form resistance and rotate speed that is a measured value.

5.References

[1] Y.Honda, Master Thesis, Tokyo Institution of Technology, "Control Method of Boost Switching Regulator for Generators with Voltage Variation 2014"

[2] H. Tokuyama and I Ushiyama "Experimental Determination of Optimum Design Configuration for Micro Wind Turbines at Low Wind Speeds" T. Japan Wind Energy Association, Vol24, No.4 (2000)

[3] Izumi Ushiyama, "Fushakogakunyumon", Morikitashuppan

Numerical analysis of the 1917 Storm Surge in Tokyo Bay based on a reproduced topography

Student Number: 10_07323 Name: Masahiro KAMBARA Supervisor: Hiroshi TAKAGI

1. Introduction

Storm surge caused by typhoons have occurred in many parts of the world since ancient times. In recent years, Hurricane Sandy that hit New York in 2012 and Typhoon Yolanda that hit Philippines in 2013 have been known as remarkable typhoon, which caused devastating storm surge.

October 1, 1917, storm surge occurred in Tokyo Bay due to the passage of a powerful typhoon crossing Tokyo in the early morning of that day. Casualties and destroyed houses by this storm surge reached up to 1,301 people and 43,083, respectively, and it became the worst disaster caused by storm surge in Tokyo Bay at least in the last few centuries.

In the first place, Tokyo Bay is vulnerable to storm surge. Sea water intruding into the bay brought by typhoon tends to be amplified because of the shape of the bay and relatively shallow water depth. Sea level increase due to typhoon wind is known to be proportional to the length of the bay and inverse proportional to the depth of the sea [1]. The frequency of major typhoon which struck Tokyo area is not necessarily often, occurring once every 5 years or so. However, if a strong typhoon approaches the bay with a critical travelling direction, significant storm surge could happen due to these topographical features. To investigate storm surge risk in the Tokyo Bay Area, the present research conducts the following four things, focusing on the event of the 1917 typhoon:

1. To reproduce the coastline of Tokyo Bay a century ago,
2. To simulate the typhoon and storm surge, encompassing Tokyo Bay,
3. To compare inundation between the simulation and the past documents which describes the situation in the Tokyo Bay, and
4. To assess the vulnerability of the current Tokyo Bay to future storm surges.

2. Reproduction of old coastline

Because of land changes in the past century due to dredging and landfill, there are many differences in the topography between the current and the past Tokyo Bay. To the authors' best knowledge, there have been no digital elevation map of the old Tokyo Bay that describes detailed topography and bathymetry in a century ago. Therefore, first we reproduced the past topography using both old paper-based map and recent digital elevation map, incorporating coastline and river in the past. A method called Kriging interpolation was applied to fill the blank areas, which are inevitably present between past and present coastlines, with smoothed interoperated elevations.

The current topography is shown in Fig. 1, and the topography before the interpolation and final reproduced topography are shown in Figs. 2 and 3, respectively.

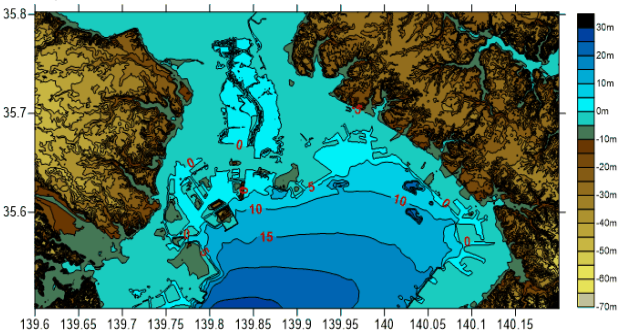

Figure 1: Current topography of Tokyo Bay

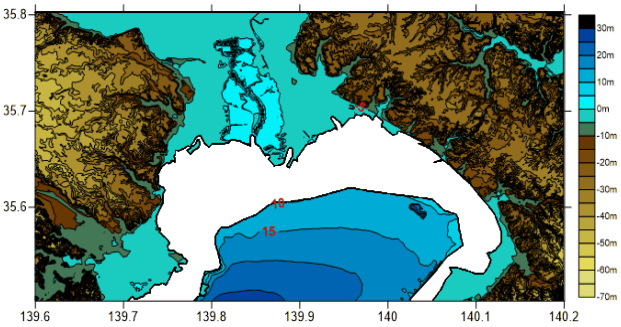

Figure 2: Before the interpolation

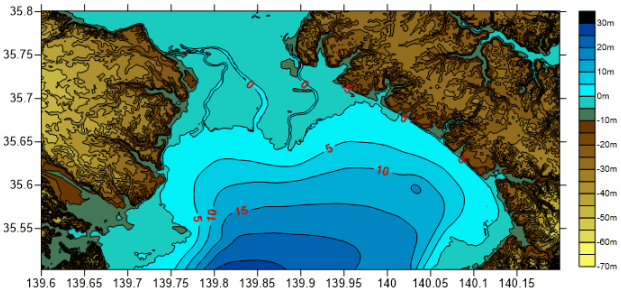

Figure 3: Reproduced topography

3. Numerical analysis

The model for storm surge simulation used is composed of a typhoon model and the fluid model using Delft-3D Flow [2]. We conducted a series of numerical trials to find meteorological conditions that best describes the storm surge due to the 1917 Typhoon by changing the central pressure and the typhoon path. These trials were required because of the limitation of available meteorological information at that time.

3.1 Analysis by changing the central pressure

Unlike the recent meteorological data which contains a number of information on a typhoon, available data in those days are limited. The typhoon central pressure, which is one of the fundamental parameters to simulate typhoon, is not available. Therefore, the central pressure has been changed until we found that the simulation could evaluate the storm surge described in the literatures [3] [4] at reasonable accuracy, while the typhoon path is set to be constant. The simulation results and water elevation measured at Kamihirai are shown in Fig.4. We found that the simulation provides the best estimate when the pressure is 830hPa, though such low pressure appears to be unrealistic.

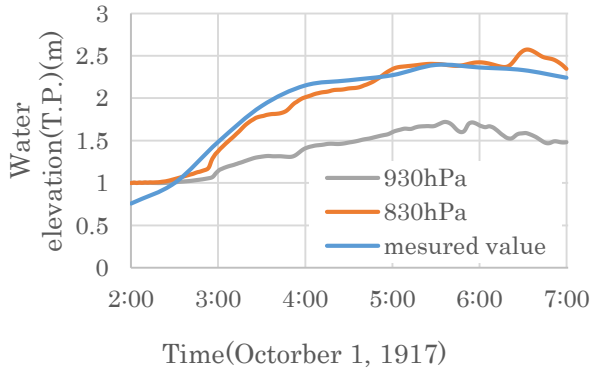

Figure 4: Result (change central pressure)

3.2 Analysis by changing the path

Second, we changed the path of typhoon, while the central pressure is kept to be constant as 930hPa. The result at Kamihirai is shown in Fig. 5. It shows that Path 3 is the closest value to the actual measured water level. However, the profiles do not necessarily resemble each other.

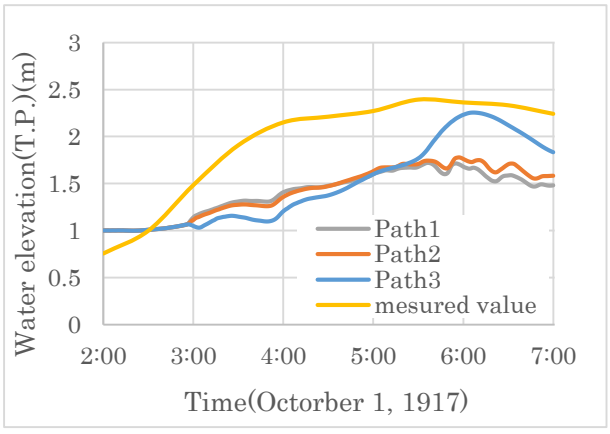

Figure 5: Result (change the path)

3.3 Analysis for the current Tokyo Bay

Finally, we performed storm surge simulation, assuming the case that the 1917 Typhoon hit the present day of Tokyo Bay. Although the present coastline has been protected by massive dykes, the present research neglected these structures in order to realize how much present Tokyo relies on the hard structures. The inundation in 1917 is shown in Fig.6. And the result of current Tokyo Bay is shown in Fig.7.Inundation occurs in a wide range of the floodplain of Arakawa and Sumida Rivers if there are no dykes. This is due to land subsidence by several meters in the past several decades. However, the dykes were designed about 4m or even higher (T.P.) in Tokyo Bay [5]. In contrast, the highest tidal level of this analysis is about 3m. Therefore, inundation would not occur even if a typhoon with the same intensity with the 1917 Typhoon comes to the present Tokyo Bay as long as such hard structures sustain the performance during the passage of typhoons.

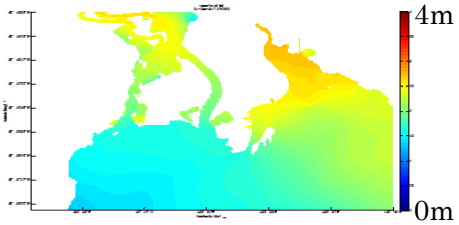

Figure 6: Inundation due to the 1917 Typhoon, assuming the old Tokyo Bay

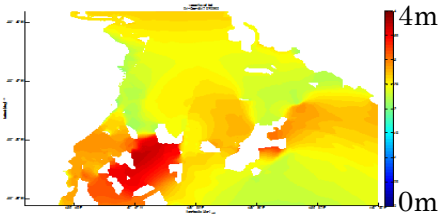

Figure 7: Inundation due to the 1917 Typhoon, assuming Tokyo Bay without the dykes

4. Conclusions

In this paper, we created a digital elevation in a century ago based on old maps and simulated the storm surge in Tokyo Bay due to the 1917 Typhoon. It was confirmed that people may not suffer from severe storm surge if the same size of typhoon hit the present day of Tokyo Bay. However, it is feared that severe storm surge would occur if the dykes protecting the waterfront lose their functionalities due to ground subsidence in the past several decades.

References

[1] 合田良實，佐藤昭二:新訂版 海岸・港湾， 彰国社，p.p.148，1981.
[2] Takagi H. et al.: Track Analysis, Simulation and Field Survey of the 2013 Typhoon Haiyan Storm Surge, J. Flood Risk Management, 2014.
[3] 土木学会: 東京湾ノ津浪，土木学会誌，第四巻，第二号，1918.
[4] 土木学会: 災後ニ於ケル東京市河海応急施設，土木学会誌，第四巻，第二号，1918.
[5]東京港湾局: 東京湾海岸保全施設整備計画，2012.

Estimation of CO_2 Emissions in Household Expenditures for Urban and Rural Area of China

Student Number: 11_07680 Name: Guan Jianxin Supervisor: Shinya HANAOKA

1. Introduction

The IPCC concluded that the rapid rise of GHG emissions concentration is the result of human activities in its 5th assessment report (AR5) [1]. China started the reform and opening-up policy since 1978. In these 30 years, Chinese government changed its planned economy to market economy, which resulted in rapid increase of economy. On the other hand, with the increase in economy rapidly increasing, CO_2 emissions of China also increased accordingly. On the basis of Emissions Database for Global Atmospheric (EDGAR)'s statistic, in 2005 China`s CO_2 emissions was 5,800,000 thousand ton, which accounted for 20% of global emission, and surpassed United States, which was the country with CO_2 emissions [2]. Therefore, increasing CO_2 emissions is a serious problem of China. One of the reasons why these years CO_2 emissions of China increased rapidly is that high speed of urbanization and rapidly increased household expenditure (demand). After the 22nd APEC Economic Leaders Meeting, Chinese government announced that China would strive to bring its spiralingCO_2 emissions to a peak by 2030.

CO_2 emission can be categorized 2 types, direct emissions and indirect emissions. In this study, direct emissions mean the emissions from different CO_2 emitting regions which are derived from industry sector, transportation sector, commercial sector, and residential sector (Figure 1). And indirect emissions are defined as the emissions from the regions where the commodities are consumed according to expenditure of money on the items for daily household life. And indirect emission divided into 2 parts. One is called indirect using, which means emissions cause by household`s daily life commodity expenditure (final demand, downstream of supply chian), the other is direct burning, which means that the emissions when household sector burns home energy (Figure 2). Consideration of the indirect CO_2 emissions is important because it is necessary to change viewpoint of emission responsibilities regarding household expenditure in China.

The objective of this study is 1) to estimate direct and indirect CO_2 emissions from urban and rural areas of different provinces in 2002 and 2007 in China, and 2) to estimate future indirect CO_2 emissions from urban and rural areas based on change in population, urbanization and household expenditure.

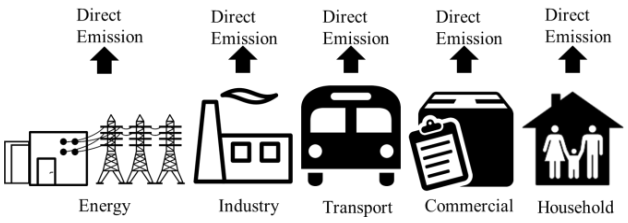

Figure 1 Direct Emission

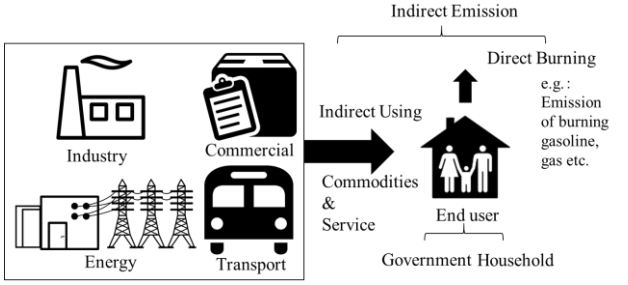

Figure 2 Indirect Emission

2. Estimation of Present Emissions

2.1. Methodology

2.1.1. Direct Emissions

In this study, the methodology for calculating direct emissions is based on the methodology used in IPCC AR5. This methodology calculated all the sector`s direct CO_2 emissions from different energy sources like gas, gasoline and so on. Detailed equation is Eq.1.

$$D_n = \sum_k q_{nk} \cdot j_k \cdot c_k \cdot o \cdot 44/12 \quad \text{.....Eq.1}$$

D_n: direct emissions of province n (t-CO_2/year)
k: 8 kinds of fuel (coal, coke, crude oil, gasoline, kerosene, diesel, fuel oil, nature gas.)
q_{nk}: consumption of province n fuel k (t/year)
j_k: lower heating value of fuel k (TJ/Gg)
c_k: carbon emissions factor of fuel k (kg-C/TJ)

2.1.2. Indirect Emissions

The calculation of indirect emissions are used Input-Output table (I-O table) (Table1). This table shows the demand of one sector for other sectors. Firstly indirect emissions intensity e_k is calculated by using Eq.2-Eq.4. Eq.2 shows the input coefficient a_{ij}, and Eq.3 means matrix of I-O table. In this study, target is household expenditure. In order to calculate indirect emission intensity, only intermediate use part is used. In competition type of I-O table, which is used in China, import and export is already added and subtracted in intermediate use part and only shown in final demand row. That means the result is not affected by import and export in considering household indirect emission.

Table 1 Input-Output Table

Input \ Output		Intermediate Use							Final Demand	Total Output
		Sector 1	Sector 2	…	Sector j	…	Sector n	total		
Interm-ediate Input	Sector 1	x_{11}	x_{12}	…	x_{1j}	…	x_{1n}		f_1	x_1
	Sector 2	x_{21}	x_{22}	…	x_{2j}	…	x_{2n}		f_2	x_2
	…	…	…	…	…	…	…		…	…
	Sector i	x_{i1}	x_{i2}	…	x_{ij}	…	x_{in}		f_i	x_i
	…	…	…	…	…	…	…		…	…
	Sector n	x_{n1}	x_{n2}	…	x_{nj}	…	x_{nn}		f_n	x_n
	total									
Added Value		v_1	v_2	…	v_j	…	v_n			
Total Input		x_1	x_2	…	x_j	…	x_n			

$$a_{ij} = x_{ij}/x_j \quad \text{.....Eq.2}$$

$$\boldsymbol{x} = (\boldsymbol{I}-\boldsymbol{A})^{-1}\boldsymbol{f} \quad \text{.....Eq.3}$$

$$e_k = \boldsymbol{d}^t(\boldsymbol{I}-\boldsymbol{A})^{-1} \quad \text{.....Eq.4}$$

After calculating the indirect emissions intensity e_k, it is necessary to match the sector k in household expenditure with sector ij in I-O table. It is able to calculate indirect emissions by using Eq.5.

$$ID_{n,u} = P_{n,u}\left(\sum_k ic_k \times E_{k,u} + db_u\right)_{u=0,1} \quad \text{.....Eq.5}$$

ID_n: Indirect emissions of province n (t-CO_2)
P_n: population of province n (person)
ic_k: indirect emissions intensity of item k (t-CO_2/CNY)
E_k: household expenditure of item k per capita (CNY/Capita)
db_t :direct burning per capita (t-CO_2/capita)
u: urban area is 1, rural area is 0

2.2. Results

The direct and indirect emissions of China was calculated for the year 2002 and 2007. The emission results for 2002 and 2007 are shown in Figure 3, direct emissions increased to double in 2007, especially in Shandong, Hebei, Liaoning province, each of province has a lot of industries or power plant.

On the other hand, indirect emissions was also increased (Figure 4). Although urban area is developed more than rural area, the increase speed of urban area is faster than rural area. Urban area`s emissions in 2007 is about double of 2002. Whereas the emission from rural area is increased just a bit. Guangdong province is in the top of the list followed by Jiangsu and Shandong province. And because of big gap of population and household expenditure (especially population), the gap between top and last is about 500 times. The emission from Guangdong is 530 megaton, whereas Xizang has only 5 megaton, which means the gap between provinces in indirect emissions is huge.

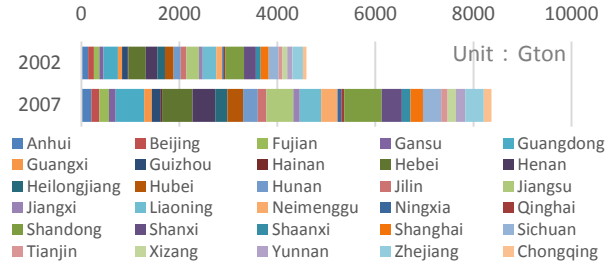

Figure 3 Direct Emissions in the year 2002 and 2007

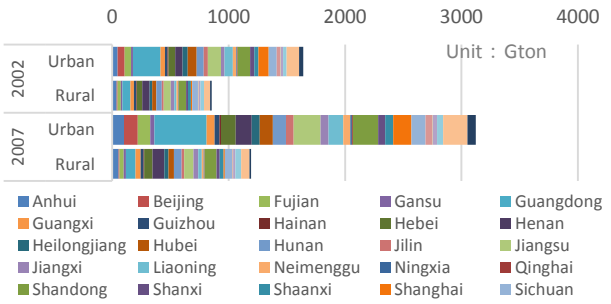

Figure 4 Indirect Emissions in the year 2002 and 2007

3. Future Forecast

3.1. Scenario Creation

1. Scenario 1: assumes that population and household consumption will maintain the current growth (BAU) as follows:

i. Population Forecast

In this study the country level forecast uses data from World Population Prospects of United Nations (UN) [3]. To calculate provinces level population, natural growth model is used [4], this model will forecast population by using a changing growth rate and fix the growth rate by using UN`s data per 5 years and then forecasts for next 5 years (Eq.6).

$$P_{n,t+5}=P'_{n,t}\times\left(1+R_{n,t}\right)^{5} \quad \text{.....Eq.6}$$

$P_{n,t}$: calculated population of province n on the year t
$P'_{n,t}$: fixed population of province n on the year t
$R_{n,t}$: growth rate in 5 years of province n

ii. Urbanization Forecast

Urbanization data is used for a logistic model of IIASA (International Institute for Applied System Analysis) [5]. Assume that the urbanization will follow s-curve (Eq.7).

$$U_t=1/1+C\times e^{-r\times(t-1979)} \quad \text{.....Eq.7}$$

The parameter C and r are based on existing data by IIASA.

iii. Household Expenditure Forecast

Change of household expenditure will follow the Engel's coefficient, when income increases, the percentage of food expenditure will decrease. By checking data from other countries, Engel's coefficient is effective. So this study assume that household expenditure follows Engel's coefficient. Double Moving Average Model (DMAM) [6] is used in this study (Eq.8).

$$x_{T+t}=\left(2M_T-M_T'\right)+\left[\frac{1}{N-1}\left(M_T-M_T'\right)\right]t \quad \text{.....Eq.8}$$

M_T: single moving average
M_T': double moving average
X_{T+t}: forecast data after t years
N: length of moving average

2. Scenario 2: consider about development policy of Chinese government at provinces in Northeast and West regions, and "donut" phenomenon of Beijing and Shanghai. In other words, urbanization rate will increase in provinces which affected by policy, and population will decrease in Beijing and Shanghai.

3. Scenario 3: household expenditure will change by logarithm distribution (Eq.9).

$$y=12123\ln(x)-106597 \quad \text{.....Eq.9}$$

4. Scenario 4: mixed scenario form scenario 2 and scenario 3.

3.2. Results

Figure 5 shows that emission result, indirect emission from almost all provinces will increase in scenario 1, 2 and 3. Indirect emission from Beijing and Shanghai will decrease because of donut phenomenon and household expenditure reduction in scenario 4. Provinces such as Hebei, Zhejiang will have a big difference in each scenario. The reason is that when donut phenomenon occur in Beijing or Shanghai, people will relocate to provinces around those cities, which leads to the increase of indirect emission. Moreover, emissions by scenario 2 is higher than scenario 3 which means that change of household expenditure is more effective to indirect emission reduction than urbanization.

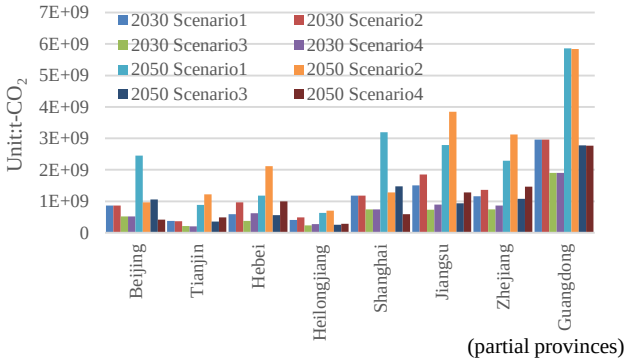

Figure 5 Urban Indirect Emissions in 2030 and 2050

4. Conclusion

The results of emissions in the year 2002 and 2007 show that CO_2 emissions increased rapidly due to the rapidly development of china in 2002 and 2007. And this study calculated indirect emission by 4 scenarios. According to the result, donut phenomenon will affect huge city like Beijing and Shanghai in the future. Furthermore the change in household expenditure is more influence on indirect emission reduction than urbanization. However, the indirect emission increase speed of whole China will get slower after 2030, therefore, CO_2 emissions will not decrease because of the increasing household expenditure and urbanization whether by scenario 1, 2, 3 or 4. In other words, it is difficult to realize the announcement of China.

References

[1]Wang, X.: Visualization of Direct and Indirect CO_2 Emission of each Municipality in Japan,Bachelor theses of IDE, 2014.
[2] EDGAR: CO2 time series 1990-2013 per region/country, http://edgar.jrc.ec.europa.eu/overview.php?v=CO2ts1990-2013.
[3]UN: World Population Prospect Total Population-Both Sexes, http://esa.un.org/wpp/Excel-Data/population.htm.
[4]Deng, Y. et al.: Spatial pattern and its evolution of Chinese provincial population and empirical study, Acta Geographica Sinica, Vol.69, No.10, pp.1473-1486, 2014.
[5]Liu, S. et al.: Scenario Analysis on Urbanization and Rural-Urban Migration in China, International Institute for Applied Systems Analysis (IIASA), Austria, 2003.
[6]Liu, W.: The forecast about the trend of consumption demands in unborn 15 year, Productivity Research, No.12, 2006.

Regularization of Support Vector Machine with Variable Kernel Functions

Student Number:11-04144 Name:Dan WANG Supervisor:Yukihiko YAMASHITA

1 Introduction

Kernel method is a data analysis methodology which has been rapidly developed in the field of computer science in recent years. It was named after kernel functions, which works in a derived feature space where the real coordinates of patterns never have to be calculated. Kernel methods have demonstrated very high performance with the best known example of Support Vector Machine (SVM). The central idea of kernel method is mapping an original input vector into a high dimensional feature space to change the nonlinear classification functions to linear classification functions. However, to realize such excellent performance, the proper selection of feature mappings is very important. For the purpose, the asymmetric kernel method (AKM) was researched. Although all sample patterns have the same parameter in the standard kernel method, in AKM, each sample pattern has its individual parameter.

In this paper, I propose variable kernel functions (VKF) to improve recognition performance, which can change the kernel parameter according to the position. I explain the framework of VKF, VKF-SVM and show five weighted regularization terms in VKF-SVM. I also show experimental results by using a toy problem and UCI datasets.

2 Framework for VKF

2.1 Mercer's Theorem

Let $\{(x_n, y_n)\}_{n=1}^N$ be a set of samples, where each x_n is a sample pattern and y_n is its label (± 1). The inner product between x and z is denoted by $\langle x, z\rangle$. In this paper, I consider a linear discriminant model for a binary problem.

In case of the standard kernel method, a Mercer kernel function $k(x, z)$ is fixed and the discriminant function is given by

$$d(x) = \sum_{n=1}^{N} \alpha_n k(x_n, x) + \theta. \quad (1)$$

Here, α_n are coefficients and θ is a threshold. From Mercer's theorem, we can consider there exists a feature mapping $\Phi(x)$ that can satisfy

$$k(x, z) = \langle \Phi(x), \Phi(z)\rangle. \quad (2)$$

Then eq.(1) can be written as

$$d(x) = \langle w, \Phi(x)\rangle + \theta, \quad w = \sum_{n=1}^{N} \alpha_n \Phi(x_n). \quad (3)$$

2.2 Asymmetric Kernel Method

AKM shows better experimental results by combining several feature mappings. In AKM, I prepare several feature mappings $\Phi_j(x)(j = 1, 2, ..., J)$ of which inner product can be calculated analytically and their kernel functions are denoted by

$$k_{i,j} = \langle \Phi_i(x), \Phi_j(z)\rangle. \quad (4)$$

2.3 Framework for VKF

In the proposing VKF, I prepare nonlinear feature mappings Φ_n for each learning pattern x_n and only one feature mapping Φ_0 for an unknown pattern x. The model of w in eq.(3) can be denoted by

$$w = \sum_{n=1}^{N} \alpha_n \Phi_n(x_n). \quad (5)$$

Then, the discriminant function is given by

$$\begin{aligned} d(x) &= \langle w, \Phi_0(x)\rangle + \theta \\ &= \sum_{n=1}^{N} \alpha_n k_{n,0}(x_n, x) + \theta. \end{aligned} \quad (6)$$

In VKF, we can change the kernel parameter according to the disatances to the adjacent sampling points.

3 VKF with SVM

SVM can be summarized as minimizing

$$\|w\|^2 + C \sum_{n=1}^{N} \xi_n, \quad (7)$$

subject to (for any n =1,2,...N)

$$y_n d(x_n) - 1 + \xi_n \geq 0, \quad \xi_n \geq 0, \quad (8)$$

where C is a constant.

I prepare a new classifier named VKF-SVM where VFK is applied to SVM. For VKF, the regularization term in (7) is denoted by

$$\|w\|^2 = \sum_{m=1}^{N} \sum_{n=1}^{N} k_{m,n}(x_m, x_n) \alpha_m \alpha_n. \quad (9)$$

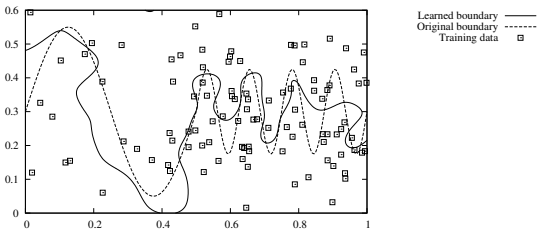

(a) SVM

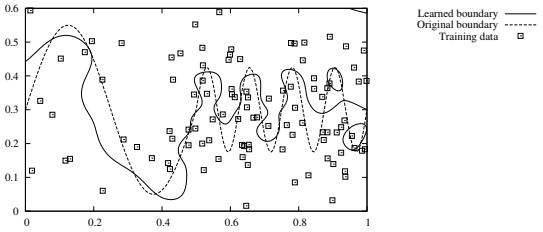

(b) VKF-SVM with SSKFR

Figure 1: Results of toy problem

I considered five weighted regularization terms to balance the regularization among α_n.

(1) Projected regularization(PrR): Let S_0 be the subspace spanned by $\Phi_0(x_n)$. Let P_0 be the orthogonal projection operator onto S_0. The regularization term is defined by $\|P_0 w\|^2$.

(2) Training sample regularization(TSR): Define the regularization term as $\sum_{n=0}^{N} |\langle w, \Phi_0(x_n)\rangle|^2$.

(3) Peak Regularization(PKR): The regularization term is given by

$\sum_{m=1}^{N}\sum_{n=1}^{N} k_{m,0}(x_m,x_m)k_{n,0}(x_n,x_n)k_{m,n}(x_m,x_n)\alpha_m\alpha_n$.

(4) Sum of kernel function regularization(SKFR):

α_n in the regularization term is replaced by

$\sum_{m=1}^{N} k_{n,0}(x_n,x_m)\alpha_n$.

(5) Square root of sum of kernel function regularization(SSKFR): α_n in the regularization term is replaced by $\sqrt{\sum_{m=1}^{N} k_{n,0}(x_n,x_m)\alpha_n}$.

4 Experiment Result

In the experiment, I decide σ_j by the average of the distances from x_j to its nearby 10 points. I use the smallest σ_j as σ_0. I also use the Gaussian kernel function (GKF) for a feature mapping. Then, the feature mapping with σ_j from a point to a function is defined by

$$(\Phi_j(x))(z) = \left(\frac{2}{\pi\sigma_j^2}\right)^{\frac{M}{2}} \exp(-\|z-x\|^2/\sigma_j^2). \quad (10)$$

From eq.(4), the kernel function for VKF is given by

$$k_{i,j}(x,z) = \left(\frac{2\sigma_i\sigma_j}{\sigma_i^2+\sigma_j^2}\right)^{M} \exp\left(-\frac{\|x-z\|^2}{\sigma_i^2+\sigma_j^2}\right). \quad (11)$$

Table 1: Error rates for UCI datasets

DN	SVM	PrR	TSR
Ba	10.52±0.50	10.52±0.49	10.53±0.47
Br	25.38±4.52	25.23±4.70	27.17±4.66
Di	23.15±1.70	23.17±1.86	**23.11±1.80**
Fl	32.31±1.84	32.31±1.84	**32.31±1.83**
Ge	23.46±2.08	23.61±2.25	23.73±2.14
He	15.39±3.28	15.39±3.24	16.01±3.35
Im	**2.97±0.57**	3.56±0.52	3.73±0.72
Ri	**1.50±0.10**	1.53±0.10	1.56±0.13
Sp	11.20±0.74	11.61±1.08	11.85±0.97
Th	4.13±2.20	**3.99±2.24**	4.12±2.19
Ti	22.29±1.05	**22.27±1.07**	22.30±1.04
Tw	2.40 ± 0.14	2.40±0.14	**2.14±0.13**
Wa	9.96±0.48	9.79±0.47	9.95±0.42

DN	PKR	SKFR	SSKFR
Ba	10.59±0.51	10.65±0.49	**10.51±0.47**
Br	25.42±4.69	**25.19±4.61**	25.32±4.35
Di	23.24±1.72	23.33±1.77	23.23±1.76
Fl	32.33±1.81	33.14±1.76	32.32±1.82
Ge	**23.39±2.28**	24.29±2.26	23.42±2.30
He	**15.27±3.19**	15.33±3.33	15.35±3.18
Im	3.08±0.58	6.75±1.31	3.20±0.68
Ri	1.58±0.13	2.52±0.26	1.60±0.13
Sp	11.51±0.72	**10.89±0.73**	11.71±0.69
Th	4.20±2.37	4.56±2.38	4.16±2.35
Ti	22.31±1.05	22.45±1.18	22.31±1.05
Tw	2.41±0.14	2.42±0.12	2.39±0.14
Wa	9.99±0.47	9.97±0.49	**9.91±0.44**

Then, I apply VKF-SVM to a toy problem and 13 types of UCI datasets. In the toy problem, the error rates for SVM, and VKF-SVM with PrR, TSR, PKR, SKFR, and SSKFR are 11.59%, and 11.16%, 11.49%, 9.93%, 11.60%, and 9.90%, respectively. From the results that VKF-SVM with SSKFR is the best with parameters: $\sigma = 0.0178$, and $C = 1.78$. Fig. 1 (a) shows results with SVM, and Fig. 1 (b) shows results of VKF-SVM with SSKFR with the best parameter. We can see clearly that Fig. 1 (b) is more smooth.

I also use 13 types of UCI datasets for experiments. Table 1 shows error rates for UCI datasets. From Table 1, we can see VFK-SVM with TSR in Tw outperformed SVM clearly.

5 Conclusion

In this paper, I proposed to apply VKF to SVM. The method was verified by a toy problem. However, error rates of UCI datasets were not improved very much. In this experiment, the selection of 12 types of UCI datasets may not be suitable. For future work, I have to improve the method to decide σ_i and search datasets that are suitable to the proposed method.

References

[1] Naoya Inoue and Yukihiko Yamashita, "Simultaneous learning of localized multiple kernels and classifier with weighted regularization" Structural, Syntactic and Statistical Pattern Recognition, pp.354-362, Springer Berlin Heidelberg, 2012.

[2] G.Wahba, "Support vector machines, reproducing kernel hilbert spaces and the randomized gacy" Technical Report 984rr, Department of Statistics, University of Wisconsin, 1998.

[3] B.W. Silverman "Spline smoothing: the equivalent variable kernel method" The Annals of Statistics, Vol.12, No. 3, 898-916, 1984.

インドネシア産天然ゼオライトを用いたマンガン除去

学籍番号：12B16311　氏名：ハリス　レザ　セプティアーノ
指導教官：日野出洋文及びウィナルト　クルニアワン

1. 緒言

天然ゼオライトはその吸着及びイオン交換能により、水質浄化、特に重金属の除去剤として期待されている [1]。火山灰等から自然形成されたため不純物が含まれており、人工的に合成されたゼオライトより除去能は低いが、合成ゼオライトよりも安価な水質浄化剤として開発が望まれる。また、既存の研究により、様々な改質・修飾処理による重金属除去能の向上が検討されている。

重金属の一つにマンガンが挙げられる。鉱物からの溶出や、工場からの排水、採掘活動がマンガンの主な排出源である。マンガンを含む水は異臭味があり、水管の閉塞、衣服への汚れなどの問題を引き起こす。さらに、マンガンを高濃度に含む水は、皮膚の病気をはじめとして人体に影響をもたらす。

従って、本研究ではマンガンの除去能に着目し、天然ゼオライトのキャラクタリゼーション及び改質処理を行うのが目的とする。

2. 実験

2.1. キャラクタリゼーション・改質処理

本研究で用いられる天然ゼオライトはインドネシアの Lampung 産天然ゼオライトである。実験で利用する前、120℃で乾燥させ、粒径 150~425 μm に調整した。得られたゼオライトは以下 NZL と呼ぶ。次に、NZL を「NaCl 処理」「HCl 処理」及び「NaCl+HCl 処理」を用いて改質を行った。

塩化ナトリウムの改質処理「NaCl 処理」での手順は次となる。NZL と/1.0 N 塩化ナトリウム水溶液を固液比 100g/L になるように混合し、12 時間以上振とうした。次に固液分離を行い、イオン交換水で残留した塩化ナトリウムを洗浄した。濾滓を 120℃で乾燥させ、粉砕し、篩で粒径を 150~425 μm に調整した。得られたゼオライトを以下 Na-NZL と呼ぶ。

塩酸の改質処理「HCl 処理」は「NaCl 処理」とほぼ同様で、1.0 N の塩化ナトリウム水溶液の代わりに 1.0 N の塩酸を使用し、この処理で得られたゼオライトを以下 HCl-NZL と呼ぶ。

塩酸及び塩化ナトリウムの複合改質処理「NaCl+HCl 処理」は「HCl 処理」を行った後、「NaCl 処理」を行う処理であり、得られたゼオライトは以下 Na-HCl-NZL と呼ぶ。

以上のすべてのゼオライトを X 線回折（XRD）、窒素吸着による BET 比表面積の測定、Chapman 法による陽イオン交換容量実験 [2]を用いてキャラクタリゼーションを行った。

2.2. マンガン除去能評価

マンガンの水溶液は酢酸マンガンを用いて所定の濃度に調整し、地下水とほぼ同様な状況の pH 6.7 ±0.2 とした。除去の実験はバッチ式で行った。

マンガンの水溶液 20 mL に 0.75 g のゼオライトを添加し、12 時間以 30℃で上振動機を用いて振とうした。液体をフィルターで収集し、ICP-AES でマンガンの濃度を測定した。ゼオライトを用いたマンガンの除去量と平衡濃度の関係を Sips 式に当てはめた。

$$q_e = \frac{q_{\max}(k_S C_e)^{1/n}}{1+(k_S C_e)^{1/n}} \qquad (1)$$

q_{max} 及び q_e は最大除去量及び除去量(mg/g)であり、C_e は平衡濃度(mg/L)を示す。また、k_s 及び n は Sips の定数及び、均一性に関する定数である。

3. 結果・考察

3.1. X 線回折

X 線回折パターンにより、NZL は主にクリノプチロライトに構造されており、不純物として曹長石及び葉ろう石が含まれている。「NaCl 処理」では結晶構造の変化があまり見られないが、「HCl 処理」を行ったゼオライトのクリノプチロライトのピーク強度の低下が見られた。これは、「HCl 処理」によ

る脱アルミニウム化による構造変化からだと考えられる。

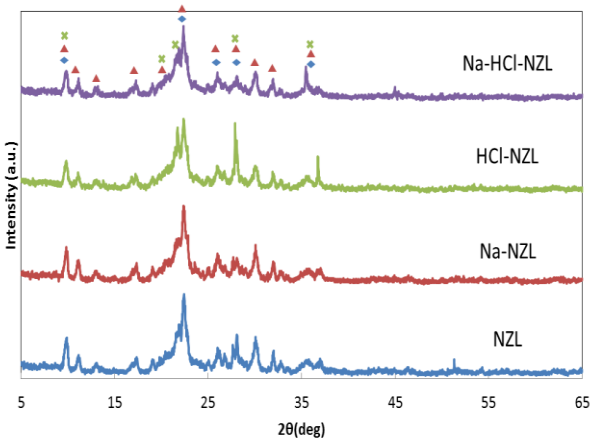

図 1 NZL 及びその改質の XRD パターン

(▲:クリノプチロライト、◆: 葉ろう石、×: 曹長石)

3.2. 陽イオン交換容量（CEC）

Chapman 法で測定した陽イオン交換容量の結果を図 2 に示した。Na-NZL が最も高い CEC(234.9 meq/100g)を有することがわかる。Na-HCl-NZL では Na-NZL より低い結果を示したが、これは脱アルミニウム化が起こり、交換容量が下がったからだと考えられる。

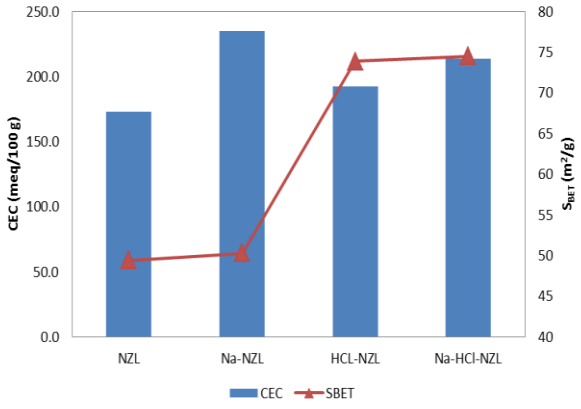

図 2 CEC 及び比表面積

3.3. 比表面積

窒素吸着の結果により BET 法で計算した比表面積を図 2 に示した。最も高い比表面積（74.51 m^2/g）を持つのが Na-HCl-NZL である。これは表面が塩酸を用いて洗浄された後、塩酸だけで交換できなかった陽イオン（K^+、Mg^{2+}、Ca^{2+}など）が、比較的小さい Na^+で交換されたからだと考えられる。よって、大きな陽イオンによって塞がれた細孔が開き、比表面積が上昇したと考えられる。

3.4. マンガン除去測定

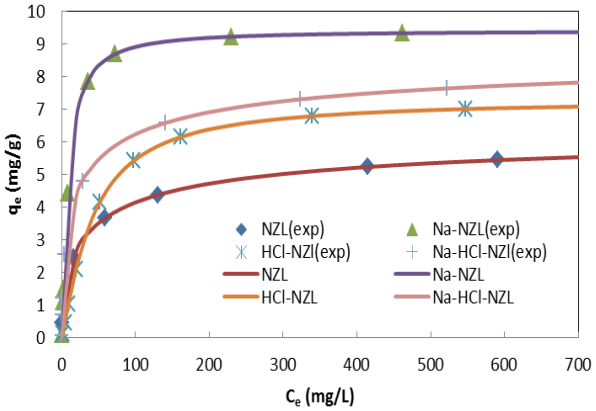

図 3 マンガン除去の Sips 等温線

Sips 式で分析されたマンガン除去実験の結果を図 3 に示した。最も高い除去量を示すのが 9.40 mg/g 最大除去量を持つ Na-NZL であり、Na-HCl-NZL、HCl-NZL、NZL の順に除去量は低下し、これは CEC の順位と一致した。しかし、CEC の値とはほど遠く、Na-NZL のマンガン除去から換算する値は 34.2 meq/100g である。これは、イオン半径及びゼオライトの構造によるものであり、Na^+が Mn^{2+}より交換されやすいことがわかった。また、マンガンの除去量は比表面積との相関が見られなかったため、除去の反応は吸着ではなく、イオン交換が支配的であると考えられる。

4. 結言

本研究で行った改質処理によってマンガン除去能を、最大 6.62 mg/g から 9.40 mg/g まで上昇させることができた。また、除去の過程ではイオン交換現象が支配的であることもわかった。

5. 参考文献

1. *USE OF NATURAL ZEOLITE (CLINOPTILOLITE) IN AGRICULTURE.* **Polat, Ersin, et al., et al.** 12, Poland：Journal of Fruit and Ornamental Plant Research, 2004, pp. 183-189.

2. *Cation-Exchange Capacity.* **Chapman, H.D.** USA：Agronomy Monograph, Methods of Soil Analysis, 1965, pp. 902-904.

Influence of initial chloride content and water cement ratio on corrosion of steel bar in mortar exposed to marine environment for 32 years

ID: 11_23733 Name: Ayako MIZUMA

Supervisor: Prof. Nobuaki OTSUKI, Assistant Prof. Takahiro NISHIDA

1. Introduction

Chloride attack is one of the serious deterioration of reinforced concrete under marine environment, and it is considered that the usage of low water cement ratio(W/C) and initial chloride content is important for preventing chloride attack. However the influence of initial chloride content on deterioration of chloride attack after long-term exposure under marine environment is not clear.

In this study, the influence of initial chloride content and W/C on corrosion after 32 years exposure was evaluated. Especially issues below were investigated.

1) To clarify the influence of initial chloride content and W/C on corrosion of steel bar within 1 year exposure to marine environment.
2) To clarify the influence of initial chloride content and W/C on corrosion of steel bar after 32 years exposure to marine environment using mortar specimens.
3) To evaluate the relations between influential factors, such as chloride content and oxygen permeability, and corrosion of steel bar after 32 years exposure to marine environment.

2. Experimental Work

1) Mortar specimen

Cement type is ordinary Portland cement, (density: 3.17g/cm^3, specific surface area: 3180cm^2/g) and sand cement ratio(s/c) is 2.0, there are 6levels in W/C; 40,45,50,55,60,65% and 6types in mixing water; tap water, seawater, seawater diluted 0.5 and 0.25 fold, and doubled and fourfold increase of chloride ion against seawater. Specimens mark W in table1 shows specimens mixing with tap water, 1S shows specimens mixing seawater and 0.25S, 0.5S, 2S, 4S is shows their concentration and dilution rate.

Specimens were made by mortar and their size is 4x4x16. Steel bar in mortar was SR235 round steel bar,(Φ:9mm, length:100mm) and cover depth is 15mm.

2) Exposure environment

The specimens had been exposed for 32 years to tidal environment of seawater in Kurihama bay at Yokosuka city.

3) Measurement

In this study, anodic/cathodic polarization curves, corrosion weight loss of steel bar and chloride content were measured on specimens.

Anodic/cathodic polarization curves were measured using potentiodynamic method. Electric current was applied with 1.0mV/sec of the sweep speed. Chloride content in mortar and corrosion weight loss were measured using JCI(SC-4) and JCI(SC-1) respectively.

3. Results and discussion

3.1Within 1year exposure

Figure1 shows the result of evaluation from the results of anodic polarization. These numbers show the grade of passive film and “0” indicates that it is easy to corrode. In figure1, specimens become grade0 faster with increasing W/C. In the same W/C, specimens become grade0 faster with increasing initial chloride content. According to those results, it was confirmed that W/C and initial chloride content hasten the destruct of passive film, but with low W/C, influence of initial chloride content becomes small.

Table1, criterion of assessment by anode polarization curves

Grade	Criterion
0	*Corrosion current density exceed 100μA/cm^2 even once. (complete destruction)
1	*Corrosion current density is in 10μA/cm^2 to 100μA/cm^2.
2	*Corrosion current density exceed 10μA/cm^2 even once and it is not in grade1 and 3.
3	*Corrosion current density is in 1μA/cm^2 to 10μA/cm^2.
4	*Corrosion current density exceed 1μA/cm^2 even once and it is not in grade3 and 5.
5	*Corrosion current density never exceed 1μA/cm^2.

*Corrosion current density in this table is in (En+0.2V to En+0.6V)

		exposed to sea water (curing in tap water)											
curing day		1 day					7 day				28 day		
measuring day		7	28	91	180	365	28	91	180	365	91	180	365
40	W	1	1	1	0	0	1	2	1	0	2	1	0
	S	1	1	1	0	0	1	1	0	0	1	1	0
	2S										1	1	0
	4S										0	0	0
45	W	1	1	1	0	0	1	1	0	0	1	0	0
	0.25S										1	0	0
	0.5S										1	0	
	S	1	1	1	0	0	1	0	0	0	1	0	0
	2S								1		1	0	0
50	W	1	1	1	0	0	1	1	0	0	1	1	0
	S	1	1	1	0	0	1	1	0	0	1	0	
55	W	1	1	1	0	0	1	0	0	0	1	0	0
	0.25S	1	1	1	0	0	1	0	0	0	1	0	0
	0.5S	1	1	0	0	0	1	0	0	0	0	0	0
	S	0	1	1		0	1	0	0	0	0	0	0
	2S	1	1	0	0	0	1	1	0	0	0	0	0
	4S	0	1	1	0	0	0	0	0	0	0	0	0
60	W	1	1	0	0	0	1	0	0	0	0	0	0
	S	1	1	0	0	0	0	0	0	0	0	0	0
65	0.25S										0	0	
	0.5S										0	0	0
	S	1	0	0	0	0	0	0	0	0	0	0	0
	2S										0	0	0

Figure 1, passivation grade

3.2 After 32years exposure

Figure2 and figure3 shows the effect of W/C and initial chloride content on corrosion content. According to these graph, it was confirmed that corrosion content is increased with an increase in W/C. On the other

hand, influence of initial chloride content is smaller than that of W/C.

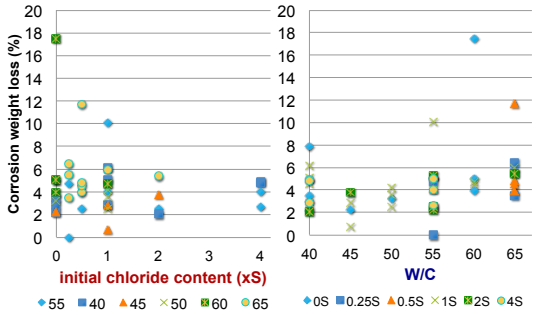

Figure2, effect of W/C Figure3, effect of initial chloride content

3.3 Relations between influential factors and corrosion

1) Corrosion and chloride content

Figure4 shows the effect of total chloride content in mortar on corrosion after 32years exposure. According to the graph, correlation was not confirmed between chloride content in mortar and corrosion. Thus estimation of corrosion content from chloride content in mortar may be difficult.

On the other hand, figure5 shows the correlation between corrosion and chloride content on steel bar. Thus it is expected that chloride content on steel bar effects on the corrosion for 32years.

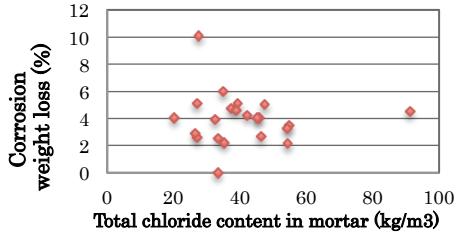

Figure4, effect of total chloride content

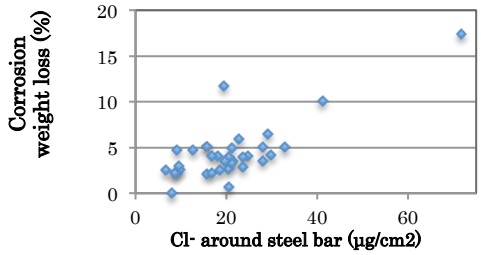

Figure5, effect of chloride content on steel bar

2) Corrosion rate and oxygen permeability

Figure6 shows the relation between corrosion rate and oxygen permeability. It was confirmed that oxygen permeability influence on corrosion rate after 32years exposure.

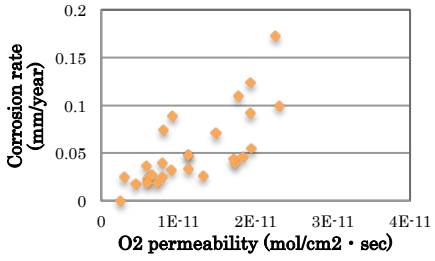

Figure6, effect of oxygen permeability on corrosion rate

3.4 Multiple regression analysis

Multiple regression analysis is one of the methods of multivariate statistics, showing the objective variable using explanatory variables. Table2 and table3 show "T-statistic" which shows the influence degree from result of multiple regression analysis. Generally, it is said that where "T-statistic" exceeding 2.0 shows the major effect. According to table2, influence of W/C on the corrosion is confirmed. From Table3, it was confirmed that correlation between chloride content on steel bar and corrosion content, and correlation between oxygen permeability and corrosion rate.

Table2, T-statistic of materials to corrosion

explanatory variable \ objective variable	corrosion content	corrosion rate
W/C	**2.37**	1.33
Initial chloride content	-0.30	-1.54

Table3, T-statistic of properties to corrosion

explanatory variable \ objective variable	corrosion content	corrosion rate
chloride content on steel bar	**4.51**	0.13
oxygen permeability	0.51	**3.13**

4. Conclusion

1) The Influence of water cement ratio on corrosion after 32years exposure is larger than that of initial chloride content under sever chloride attack environment.
2) Within 1year exposure, it was confirmed that W/C and initial chloride content hasten beginning of corrosion. Although, with low W/C, influence of initial chloride content on beginning of corrosion become small.
3) Strong correlation between corrosion weight loss and chloride content on steel bar was confirmed after 32years exposure. On the other hand, the corrosion rate of steel bar in mortar after 32 years exposure is highly related to oxygen permeability.

5. References

[1] Nobuaki Otsuki (1985) The study about influence of chloride ion on corrosion of steel bars in concrete, Port and Airport Research Institute, Vol. 24, No. 3, pp.183-284.
[2] Fukute Tsutomu (1990) The study on the durability of marine concrete mixing seawater, Port and Airport Research Institute, Vol. 29, No. 3

ドップラーライダーで観測された
水平風速パターンの自動分類

学籍番号：11B27079　氏名：李　安琪　指導教官：神田　学，稲垣　厚至

1．背景と目的

大気境界層の特性やメカニズムを理解することは、都市の排熱や工業地域の大気汚染などの問題を解決する上で重要である。過去の研究によって、大気境界層内の水平風速場は大まかにストリーク構造とセル状構造の２種類に分けられることが指摘されている。[1]これまでの研究において、ドップラーライダーを用いて水平風速場を測定し、その可視化画像から目視によって流れ場を分類することがなされている。主流風速と大気安定度が水平風速分布のパターンの出現頻度と密接な関係があることが分かっている[2]。

しかし、目視分類法は主観的であり、かつ時間がかかるなどの欠点があり、長期間の観測データを客観的に解析することが難しい。そこで本研究では、ドップラーライダーで観測された水平風速分布の可視化画像と VAD 法[3]で算出した主流風速に基づいて機械学習で判別分析をし、一年間の画像を 3 つのパターンに自動分類するアルゴリズムを開発した。それによる各パターンの出現頻度の日中変化と季節変化について調べた。

2．観測、解析手法

観測概要

観測領域は東京都目黒区東京工業大学西 8 号館屋上（地上高 42m）を中心とした半径 4km の円内であり、解析対象は、2012 年 3 月 1 日~2013 年 2 月 11 日の間でドップラーライダーの水平スキャンによって実測されたデータである。2012 年 7 月 26 日~9 月 24 日の間、空間分解能は 100m、その他の期間は 50m である。

データ前処理

Generic Mapping Tools によって対象期間内全てのデータを視線方向風速分布の二値画像と RGB 画像にし、関心領域(ROI) を X、Y 軸に沿ってそれぞれ-4.3km~4.3km に、画像サイズを 285 x 285 pixel に統一した。

中心から半径 143pixel の円内の関心領域(ROI)に存在する視線風速は正(黒)と負(白)の境界線の長さを計算し、この境界線の長さはパターンによって変化すると推測した。

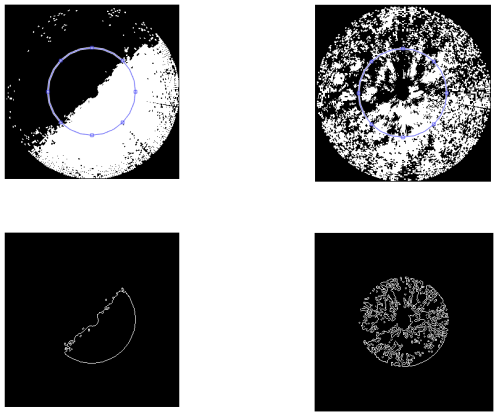

(a) Streak/No-streak　　(b) Fishnet

Figure 1　中心から半径 143pixel の円内の関心領域(上)とその中に存在する境界線(下)

Velocity Azimuth Display (VAD) 法を用いて、水平主流風速(A_{tran})を含む５つの指標を最小二乗近似の回帰線によって推測した。

教師あり機械学習に用いるため、2012 年 10 月~2013 年 2 月の毎月 1 日~10 日の間の RGB 画像に対し、目視分類を行った。15946 枚の画像のうち、11033 枚が八木ら[4]の目視分類結果と同じことがわかった。

さらに、データの品質管理上、一定の観測領域半径 (空間分解能 50m, 100m のデータはそれぞれ 2025m, 2050m)内で Signal to Noise Ratio(SNR) が 6dB 以下の値が 1 %以上のデータは Error と分類し、解析対象外とした。

分類予測器

線形判別と２次判別があり、MATLAB Statistic Toolbox を用いてそれぞれ目視分類を行ったデータのうち 'Fishnet', 'Mixed' と 'Streak/No-streak' に分類されたデータをもとに判別分析を行った。

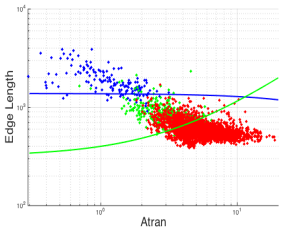

(a) A_{tran}, 境界線の長さを変数とした線形判別分析

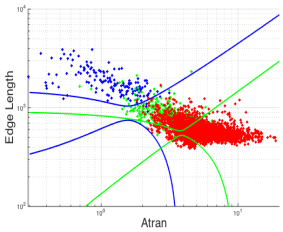

(b) A_{tran},境界線の長さを変数とした 2 次判別分析

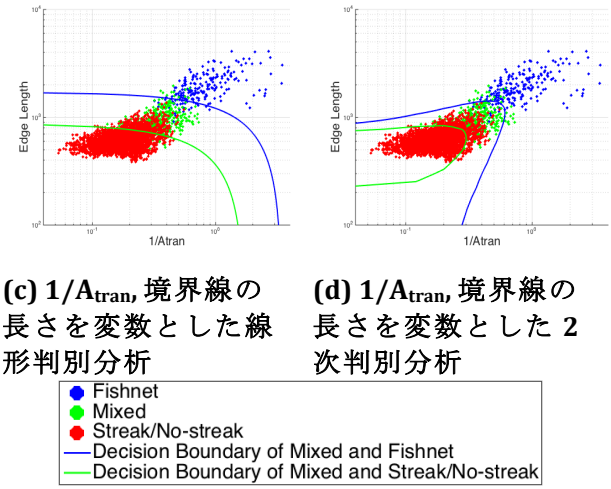

(c) $1/A_{tran}$, 境界線の長さを変数とした線形判別分析

(d) $1/A_{tran}$, 境界線の長さを変数とした 2 次判別分析

Figure 2 各変数のパターン散布図と 2 種類の判別分析の境界線(データ数 3868)

3. 結果

境界線の長さ(Edge Length)と主流風速(A_{tran})、または $1/A_{tran}$ を変数に基づいて、2 つの判別タイプでそれぞれ分析を行った結果の誤判別率を以下の表に示す。

Table 1 The re-substitution errors of 2 types of discriminant analysis and 2 types of variables as input

Variables (input)	Discrimin-ant type	Re-substitution error
A_{tran}, Edge Length	Linear	0.2055
A_{tran}, Edge Length	Quadratic	0.2306
$1/A_{tran}$, Edge Length	Linear	0.1722
$1/A_{tran}$, Edge Length	Quadratic	0.1642

この結果より、誤判別率と判別境界線の形状より、$1/A_{tran}$ と Edge Length を変数としたほうがより正確的に自動分類できると考えられる。そのうち線形判別分類器より 2 次判別分類器のほうは誤判別率が小さかった。

2 次判別分類器をもとに、1 年四季全期間の分類を行った。各水平風速パターンの出現率の月ごとの変動を Figure 3、日中変化を Figure 4 に示す。

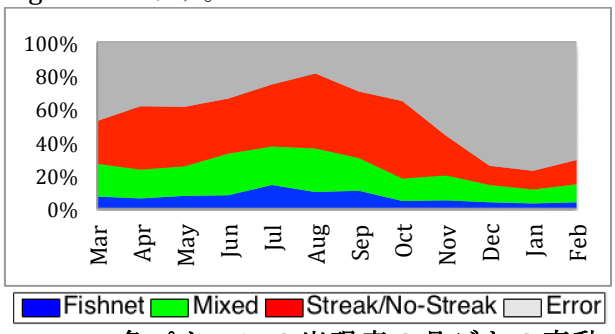

Figure 3 各パターンの出現率の月ごとの変動 (データ数 93443)

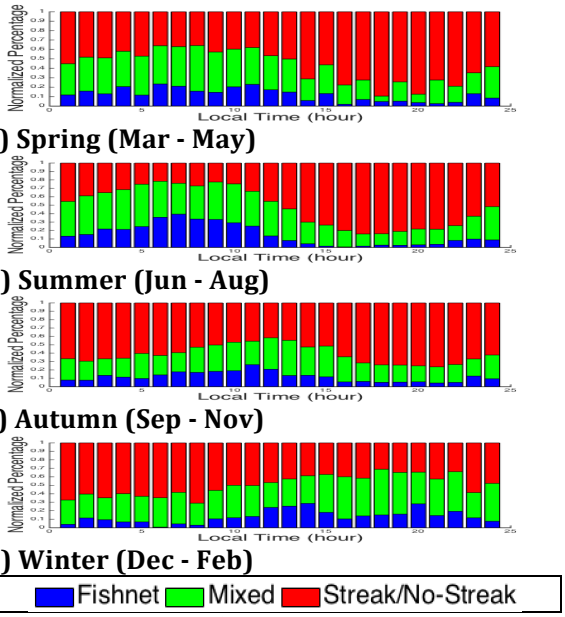

(a) Spring (Mar - May)

(b) Summer (Jun - Aug)

(c) Autumn (Sep - Nov)

(d) Winter (Dec - Feb)

Figure 4 各水平風速パターンの出現率の日中変化(Error を除く)

4. 考察と結論

'Fishnet'と'Mixed'の出現率のピークは、データ取得率が高い夏季には午前 10 時前に、データ取得率がやや高い秋季には 11 時~12 時に見られた。一方、データ取得率が低いことや PPI スキャンスケジュールの不統一性があるため、春季と冬季には'Fishnet'と'Mixed'の出現率のピークがそれほど見られなかった。

また、2 次判別分類器の 0.1642 の誤判別率は相対的に低かった。しかし、目視分類は客観的な分析ではないため、'Fishnet'と'Streak/No-streak'の中間である'Mixed' パターンの分類基準は不明瞭である。それに対して、本研究成果により'Mixed'と'Fishnet'、または'Mixed'と'Streak/ No-streak'の境界線を客観的に決めることができた。

参考文献

1) 藤吉康志, 山下和也, 藤原忠誠, 2005: 3 次元走査型コヒーレントドップラーライダーによる大気境界層の流れの可視化, 天気, 52, p.665-666.

2) 有場次郎, 神田学, 2013:ドップラーライダーで観測された流れ場の分類と特性の把握, 東京工業大学国際開発工学科学位論文

3) Browing, K. A., Wexler R., 1968: The Determination of Kinematic Properties of a Wind Field Using Doppler Radar, Journal of Applied meteorology and climate 7, p.105-108.

4) 八木綾子, 稲垣厚至, 神田学, 藤原忠誠, 藤吉康志, 2014: 相似測に基づいた大気境界層における水平乱流場の分類, 土木学会論文集 B1(水工学), Vol.70, No.4, I_325-I_330.

フルデュプレクスで構成される基地局間無線バックホールリンクの自己干渉に関する基礎的検討

学籍番号: 11_27139　名前: リュウ　コウ　指導教員: 高田　潤一

1　研究の背景

近年，モバイルデータトラヒックが急速に増加している．モバイルデータトラヒックは 2013 年には前年比 81% 増加し，2018 年には 2013 年の 19 倍になると予測されている [1]．そのため，今後高速にデータを伝送する技術が必要となる．伝送速度を高めるためには，広帯域を利用することが必要である．現在，低周波数帯域においては，すでに多くの帯域が利用されているため実現が困難であるが，高周波数帯域ではまだ利用されていない周波数帯域が存在するため，低周波数帯域を利用することに比べ，広帯域化の実現に将来性がある．しかし，高周波数帯域を利用する場合，電波の減衰が速いため，広い範囲をカバーすることができない．このため，マクロセル，及びスモールセルを組み合わせて利用する方法が提案されている [2].

通常，基地局と基幹ネットワーク間には中継回線が存在し，これをバックホールという．バックホールは光ファイバで繋がっているが，川や道路に分かれた場所に回線の設置が困難であり，コスト削減するために新規のスモールセルと既存のマクロセルの間に無線でバックホールを設置する方法が検討されている．そして，高速通信のため，マクロセルとスモールセル間のバックホールはフルデュプレクス通信方式で構築する方法が提案されている．フルデュプレクス通信方式とは，同じ周波数帯域を利用し同時に送受信を行う通信方式である [3]. この通信方式では，通常のハーフデュプレクスに比べて周波数利用効率が 2 倍となる一方，送信信号が直接受信機に回りこむ自己干渉の問題があるため，まだ広く使われていない．自己干渉の問題を解決できれば，更なる無線通信の高速化が期待できる．自己干渉は，送受信アンテナ間の相互結合と反射波による回り込みの 2 種類が存在する．送受信アンテナの距離 R とすると，相互結合は $\frac{1}{R^2}$ に比例する．このとき，送受信アンテナを離すと，その影響が小さくなる [4]．しかし，アンテナの正面に散乱体があると，反射波の影響により自己干渉が発生し，受信機の低雑音増幅器が飽和し，信号処理による自己干渉除去ができなくなる．また干渉量は，散乱体と基地局

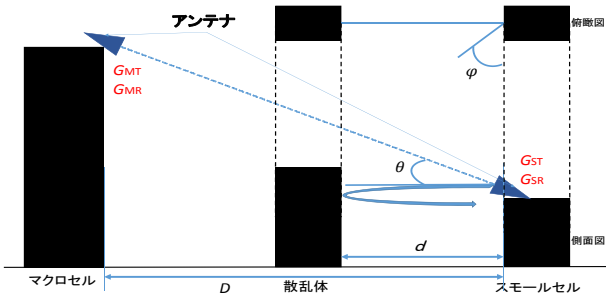

図 1: シミュレーション環境

位置やアンテナ利得などのパラメタに影響されている．

よって，本研究では自己干渉電力と各パラメタの関係を定量的に分析し，自己干渉が許容できる強度以下となるアンテナの条件を明確にする．

2　干渉波受信電力の計算方法

干渉受信電力発生のメカニズムをパラメタとともに図 1 に示す．自己干渉は，スモールセルから送信された電波が，アンテナ近傍にある建物等の散乱体により散乱されるため，その干渉波はスモールセルの受信アンテナで受信されることで生じる．図 1 において，D はマクロセルとスモールセル間の距離，d はスモールセルと散乱体間の距離を表す．G はアンテナ利得を表しており，G_{MT}，G_{MR}，G_{ST} と G_{SR} はそれぞれマクロセルとスモールセルの送信と受信アンテナの利得を表す．θ はスモールセルアンテナの仰角を表す．H_{M} と H_{S} はそれぞれマクロセルとスモールセルの高度を表す．これらのパラメタを用いると各基地局の受信電力は以下のように表される．

$$P_{\mathrm{MR}} = P_{\mathrm{ST}} + G_{\mathrm{ST}}(0) + G_{\mathrm{MR}}(0) + P_{\mathrm{L}}(D) \quad (1)$$
$$P_{\mathrm{SR}} = P_{\mathrm{MT}} + G_{\mathrm{MT}}(0) + G_{\mathrm{SR}}(0) + P_{\mathrm{L}}(D) \quad (2)$$

ここで，P_{ST} はスモールの送信電力，P_{MT} はマクロセルの送信電力，$P_{\mathrm{L}}(D)$ は伝搬距離に依存する自由空間伝搬損失を表している．マクロセルとスモールセルの位置が決まると，変更可能なパラメタはアンテナ利得だけになる．そのため，アンテナ利得を得ることができるようにバックホールの回線設計をする必要がある．そして，

回線設計においてアンテナ利得の配分を行えば，干渉電力も散乱体の距離 d によって式 (3) のように定まる．ただし，建物における散乱は，最悪値を想定し全反射と仮定する．このとき，回線設計を満足する範囲で自己干渉受信電力（P_{I}）を制御できるパラメタは $G_{\mathrm{ST}}(\theta)$ と $G_{\mathrm{SR}}(\theta)$ のみなる．またシミュレーションで用いるアンテナは，円形一様分布開口面アンテナを想定するため，各方向の利得が計算できる．このとき，G_{ST} と G_{SR} を用いて，P_{I} は次の式で求められる．

$$P_{\mathrm{I}} = P_{\mathrm{ST}} + G_{\mathrm{ST}}(\theta) + G_{\mathrm{SR}}(\theta) + P_{\mathrm{L}}(2d) \qquad (3)$$

本研究では，スモールセル側における反射波の受信電力について検討するが，パラメタを変化させるときに，マクロセルとスモールセルを繋げるため，バックホールに関する設計を行い，パラメタの変化範囲を計算する必要がある．そこで基地局間の距離，仰角や最大送信電力などを式 (1) に代入し，最低限必要となるアンテナ利得の計算を行い，自己干渉電力の影響がない条件を明らかにする．

3 シミュレーション結果

スモールセル側の方が自己干渉の影響が大きいため，スモールセルを主な対象とする．式 (3) により，干渉電力に決まるのは P_{ST}，G_{ST}，G_{SR}，d と θ のみである．シミュレーションの条件は，マクロセル側のアンテナ利得バックホールが通信できると仮定し，スモールセル側の送受信アンテナ利得が同じと設定する．そのため，もし P_{ST} と d が決まると，自己干渉の受信電力がちょうど最低受信レベルになるような利得 G と仰角 θ に関する等高線の図が描ける．ここで，二つの例を出す．図 3 と図 2 に示している線は各距離 d の時に自己干渉電力が受信できる最低の条件を示している．これらの線より左側は自己干渉がある条件で，右側は自己干渉がない条件である．アンテナ利得が低い場合では，干渉が発生しにくいが，マクロセル側の非常に高利得のアンテナを使う必要があるため，実現するのは難しい．次に，干渉エリアの形はすごく特徴があるが，実はこれアンテナ放射パターンと似て，関連している．また，仰角が小さいときも干渉がない部分についての理由はアンテナ放射パターンに非常に小さく，ヌルと呼ばれる部分であるため，そこからほとんど電波を出さないため，反射してきた干渉電力も小さいからだ．

これらの図から，環境の条件が決まるとどのような利得のアンテナを使うべきかわかった．例えば，図 2 のように P_{ST} が 23 d Bm の時．θ が 6 度の場合では，利得が 25 d Bi 以上のアンテナを使うべきである．そして，図 3 のように P_{ST} が 15dBm のとき．同じく，θ が 6 度

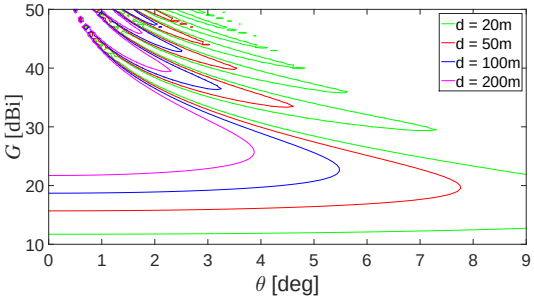

図 2: P_{ST}=23dBm 時の自己干渉条件

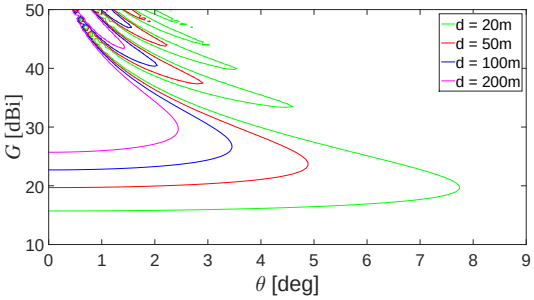

図 3: P_{ST}=15dBm 時の自己干渉条件

の場合では，アンテナ利得の制限がない．このように，環境条件により使用すべきなアンテナ条件がわかる．

4 結論

本研究おいて，フルデュプレクスでスモールセルの無線バックホールを構築するときに，自己干渉電力と各パラメタの関係を定量的に分析できた．そして, その結果を利用し，アンテナ利得の選択により，自己干渉に影響されない条件が明らかにした．

参考文献

[1] Contact Cisco,“Cisco VNI Service Adoption Forecast, 2013-2018,” http://www.cisco.com/c/en/us/solutions/collateral/service-provider/vni-service-adoption-forecast/Cisco_VNI_SA_Forecast_WP.html

[2] Association of Radio Industries and Businesses (ARIB), “ARIB 2020 and Beyond Ad Hoc Group White Paper Mobile Communications Systems for 2020 and beyond,” http://www.arib.or.jp/english/20bah-wp-100.pdf

[3] A. Sabharwal, P. Schniter, “In-Band Full-Duplex Wireless: Challenges and Opportunities,” IEEE, pp.813-816, Department Rutgers University, July 2, 2014

[4] Xiang-Yu Cao, Guo-Xian Dai, Shu-Chun Zhen, Jun Gao, “The mutual coupling between horns in the near-field,” IEEE, pp.357-359, 18-20 Aug, 1998

プロペンを還元剤とした Mo 添加 ZrO_2-CeO_2 複合触媒による NO 選択還元

学籍番号：10_07837　氏名：許 正航　指導教官：日野出 洋文　Winarto Kurniawan

1　はじめに

ガソリンエンジンは、静粛性が高い特徴がある。比較的軽量で製造コストが安く、乗用車をはじめ小型商用車、自動二輪車などに広く利用される[1]。しかし、酸性雨や光化学スモッグの原因物質の一つであるリーンバーンエンジン排気中の NO_x の低減が大きな課題である。さまざまな対策方法の中に、炭化水素による NO_x の選択還元触媒（HC-SCR）が NO_x と未燃炭化水素を同時に除去することができ移動発生源に由来する窒素酸化物を除去するために効果的かつ経済的な技術であることが証明されている。現在のパフォーマンスは、特に商用アプリケーションでは、その低温領域での性能は十分ではない。HC-SCR 反応では、異なる金属の組み合わせで生まれる“複合触媒機能”および“二元促進効果”は固体触媒の働きを考える上で重要でかつ非常に有用な現象である。

そこで、本研究では、Mo 添加 CeO_2-ZrO_2 複合触媒の NO 選択還元に対する活性を検討した。CeO_2 は経済的な材料であり、酸素貯蔵物質として注目されている[2]。CeO_2 それ自体は、高い NO 分解の活性を示さないため、ZrO_2 を混合触媒の活性向上のために使用した[3]。また、既存の研究より、NO から NO_2 への酸化反応を促進させる MoO_3 は、炭化水素の還元剤としての働きをさらに高めることもできると報告されている[4]。

2　触媒調製および触媒のキャラクタリーゼーション

触媒は機械的混合法によって調製した。日本参照触媒部会の JRC-ZRO-６（以下 ZrO_2）と JRC-CEO-１（以下 CeO_2）、そして $(NH_4)_6Mo_7O_{24}$ ・$4H_2O$ の 3 種の触媒を前駆体として使用した。3 種の前駆体を５５０℃で 4 時間焼成してから、ZrO_2、CeO_2 をモル比 1:1 になるように秤量し、次に、MoO_3 を目的の混合比になるよう秤量する。 秤量した ZrO_2、CeO_2 と MoO_3 をメノウ乳鉢で機械的に混合する。分散性を高めるために、少量のエタノールを加えた。試料を均一に粉砕し、常温で乾燥した後、円筒状のペレットにして、粒径が 0.71～1.00mm になるよう成型し、「焼成前」の触媒として使用した。焼成処理の触媒活性への影響を確認するため、常温で乾燥のステップまで調製した触媒をもう一度５５０℃で 4 時間焼成し、円筒状のペレットにして、粒径が 0.71～1.00mm になるよう成型し、「焼成後」の触媒も用意した。選択還元反応でプロペンの役割を確認するため、プロペンの有無による活性実験を行った。

活性実験は固定床流通反応装置で行った。反応ガス組成は、NO:1500 ppm, O_2:10%, C_3H_6: 1500 ppm であり、He をバランスガスとして用いた。調製した触媒 0.9-1.4g に、空間速度を 13000 h^{-1}（約 4 mL/s の総ガス流量に相当）に固定し、温度を 150-550°C まで段階的に変更して活性実験を行った。NO 濃度は、窒素酸化物分析計（島津製作所、NOA-7000）によって分析した。CO_2 分析には、ガスクロマトグラフ（GL サイエンス、GC-390）を使用した。触媒のキャラクタリーゼーションのために、TG-DTA(TG8120, Rigaku)、XRD(Multi Flex, Rigaku)、窒素吸脱着法（Autosorb-1MP, Quantachrome）を用いた。機械的混合法により調製した Mo 添加 ZrO_2-CeO_2 複合触媒の比表面積を表 1 に示した(以下、BC:焼成前、AC:焼成後)。焼成処理により、10%MoO_3 添加触媒の比表面積は、78.1 m^2/g から 42.9 m^2/g に、20%MoO_3 添加触媒の比表面積は、75.4 m^2/g から 29.9 m^2/g にそれぞれ低下した。調製した各複合触媒の XRD の測定結果を図 1 に示した。これより、調製した触媒は焼成処理により、新しい化合物（$Ce_2Mo_4O_{15}$）が生成したことが認められた。

表 1　MoO_3 添加触媒の比表面積

触媒	比表面積(m^2/g)
10%MoO_3+(ZrO_2-CeO_2)(BC)	78.1
20%MoO_3+(ZrO_2-CeO_2)(BC)	75.4
10%MoO_3+(ZrO_2-CeO_2)(AC)	42.9
20%MoO_3+(ZrO_2-CeO_2)(AC)	29.9

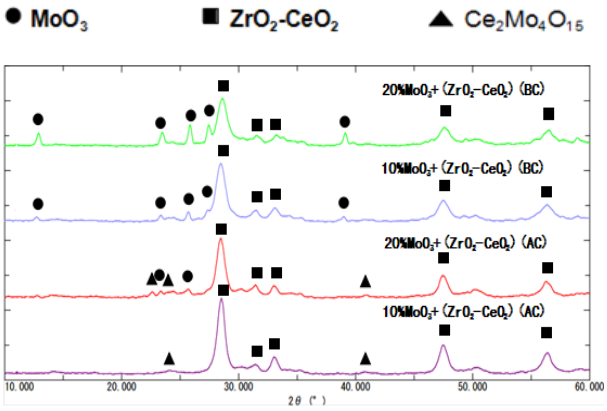

図１　MoO_3添加触媒の XRD 解析結果

３　触媒の活性実験結果と考察

図２に機械的混合法による「焼成前」の Mo 添加 ZrO_2-CeO_2 触媒の NO の活性実験結果を示した。ZrO_2-CeO_2 触媒に比べ、10%、15%、20%の MoO_3 を添加した ZrO_2-CeO_2 触媒は、活性の向上が確認できた。最大活性点は 10%添加触媒の 300℃で、約 46%の転化率を示した。MoO_3 を添加した触媒は、温度変化に対しての活性の傾向はほぼ同じで、最大活性点を示す温度が ZrO_2-CeO_2 複合触媒より低くなった。

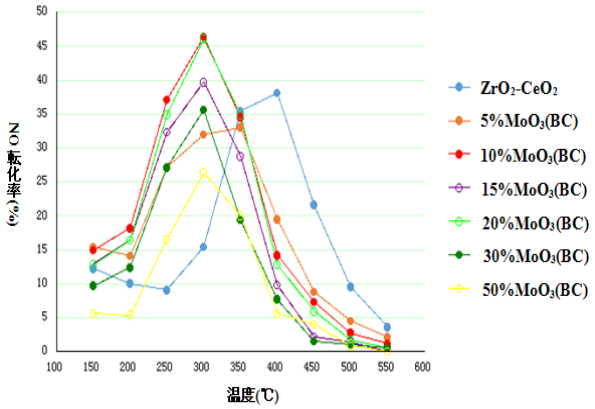

図２　MoO_3添加触媒の焼成前の NO→N_2還元活性実験(BC)

図３には、プロペン未流通下の条件で機械的混合法による調製した Mo 添加 ZrO_2-CeO_2 触媒を焼成する前の NO の活性実験結果を示した。これらは全部、NO 転化率が５％以下となった。この結果より、Mo 添加 ZrO_2-CeO_2 触媒による NO 選択還元反応では、プロペンは重要な役割を担っていることが確認できた。

図４には、機械的混合法による調製した「焼成後」の Mo 添加 ZrO_2-CeO_2 触媒の NO の活性実験結果を示した。NO から N_2 への転化率は両方とも 10%以下であった。また、図１から、焼成処理により、MoO_3 添加触媒は、新しい化合物が生成したことを確認できたため、触媒活性の低下をもたらしたと考えられる。

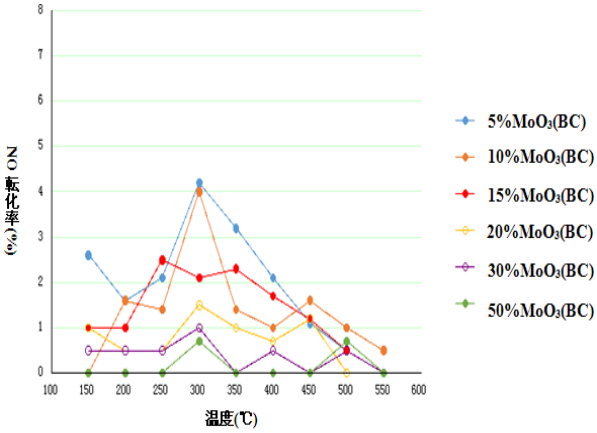

図３　プロペン未流通下 MoO_3添加触媒の NO→N_2還元活性実験(BC)

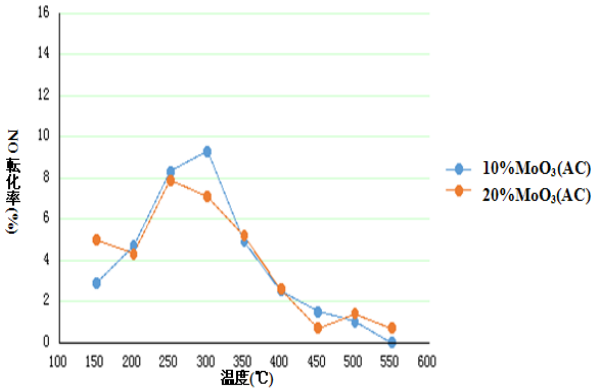

図４　MoO_3添加触媒の焼成後の NO→N_2還元活性実験(AC)

４　結論

機械的混合法によるプロペンを還元剤とした Mo 添加 ZrO_2-CeO_2 複合触媒の NO の選択還元反応は、比較的に高い活性を示した。10%、15%、20%の MoO_3 を添加すると、 ZrO_2-CeO_2 複合触媒の活性を向上させることができることが確認できた。10%MoO_3 を添加した CeO_2-ZrO_2 が、最も活性の高い触媒であった。その理由としては、ZrO_2-CeO_2 複合触媒と MoO_3 の混合率が影響を与えるためであると考えられる。そして、Mo 添加 ZrO_2-CeO_2 触媒による NO 選択還元反応では、プロペンは不可欠なことも確認できた。また、「焼成後」の Mo 添加 ZrO_2-CeO_2 の触媒活性は、「焼成前」より低くなったのは、焼成処理による複合化合物の生成が原因だと考えられている。

参考文献

[1] 図解雑学 「自動車のメカニズム」， 古川修 監修，ナツメ社 (2009)

[2]「化学大辞典」，大木 道則，大沢 利昭 他編集， 東京化学同人 (1989)

[3]「いまセリウムがおもしろい」，(株)ティー・アイ・シィー，初版 (2005)

[4] 金 東一， 学士論文， 東京工業大学 (2012.3)

Field survey and numerical analysis of storm surge inundation in Tacloban City caused by the 2013 Typhoon Haiyan

Student Number: 11_27091 Name: Siyang Li Supervisor: Hiroshi Takagi

1. Introduction

Typhoon Haiyan (Yolanda, the local name) made landfall in the Philippines on 8 November 2013, which gave huge damages to the Leyte, Samar, and many other islands. According to the National Disaster Risk Reduction and Management Council, it is reported that 6245 people died, 28626 people injured, and 1039 people were still missing by March 6, 2014. Haiyan is the strongest storm recorded at landfall, and the strongest typhoon ever recorded in terms of one-minute sustained wind speed.

On November 8, Typhoon Haiyan made landfall in Leyte, Samar and other islands causing catastrophic destruction. According to the statistical result, a large storm surge inundated most to the coastline of Leyte Gulf, causing particularly large damage to the sea front of Tacloban City, which is the biggest city in Leyte Island, located at the north western end of Leyte Gulf.

This paper aims at revealing the characteristics of storm surge caused by Haiyan, focusing on Tacloban City, Leyte Island, where the largest number of casualties took place. To do so, the numerical simulation was conducted and verified by a comparison with the field survey by the authors.

2. Overview of field survey

Because the elevation data measured by satellites is not sufficiently accurate, it cannot be used for the purpose of storm surge simulation. The field survey was carried out in Tacloban City from May 2 to May 4, 2014 (Fig.1), and the following factors were measured: First, elevations at about one hundred points were measured using a handy GPS and laser rangefinder. Second, inundation depth, arrival time of the storm surge, flow direction and other relevant information were obtained primarily by the interview with local residents. The results of field survey are shown in Fig 2.

In addition, the flow velocity of the storm surge was also estimated by a visual investigation of the video taken from Hotel Alejandro in order to compare it with the simulated flow velocity. The velocity was estimate to be about 0.6 m/s on 7:50AM November 8, 2013.

Figure 1: Field survey in Tacloban, Philippines

		latitude	longitude	Measured height from sea level(m)	Terrain elevation(m)	Measured height from the ground(m)
Tacloban	Survey 1	11.2416667	125.004306	4.46	3.38	1.08
	Survey 2	11.2419444	125.0045	5.23	3.38	1.85
	Survey 3	11.2430833	125.000639	3.5	2.5	1
	Survey 4	11.2436944	125.000028	4.8	2.5	2.3
	Survey 5	11.2463333	124.995694	5.2	2.4	2.8
	Survey 6	11.2452778	124.996306	5.2	2.4	2.8
	Survey 7	11.2446667	125.00075	5.8	2.7	3.1
	Survey 8	11.2438889	125.00225	6.17	3	3.17
	Survey 9	11.2458333	125.002222	5.9	1.7	4.2
	Survey 10	11.2483056	125.003694	5.5	2	3.5
	Survey 11	11.2455556	125.007944	3.6	1.5	2.1
	Survey 12	11.2467222	125.004028	4.52	2	2.52
	Survey 13	11.2389167	125.005167	5.03	2.8	2.23
	Survey 14	11.2512778	125.006806	7.61	6.11	1.5

Figure 2: results of filed survey

3. Numerical analysis

The fluid simulating code, Delft3d-Flow, coupled with the typhoon model (Takagi et al., 2014) was employed for the simulation. The elevation of Tacloban City was created using the results of field survey (Fig.3). The modified map is expected to greatly contribute to improving the accuracy of the model.

Figure 3: Elevations used for the simulation in Tacloban

The Manning's *n* value is one of the determining factors of fluid mechanics. The simulation was repeated to find the appropriate value for this factor by changing the number, and the result was obtained as shown in Fig.4. Comparing the velocity between the simulation and the video inspection, the *n* value was estimated to be 0.04, which is a similar value recommended by MLIT (2012) for tsunami simulation.

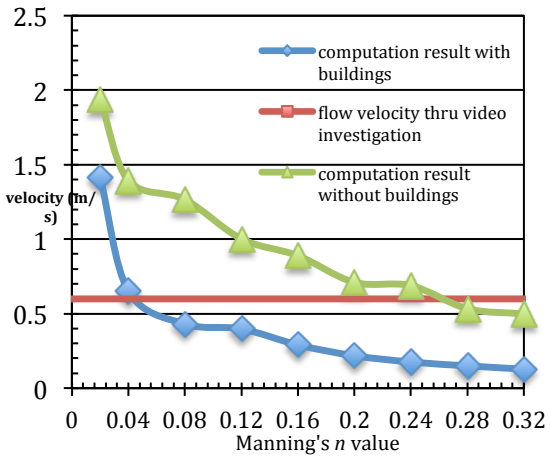

Figure 4: comparison of velocity

The results of computation between "with buildings" and "without buildings" are shown in Fig.5, indicating significant overestimate for the case of "without", while the simulation with buildings agrees well with the measured heights. It is expected that the existence of dense buildings contributes to reducing flow velocity and lower the depth of storm surge inundation.

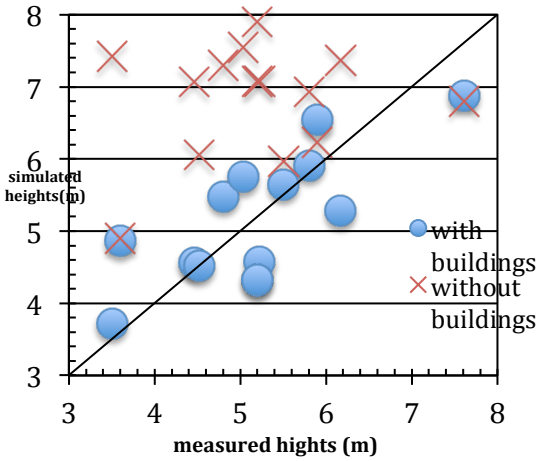

Figure 5: comparison of depth

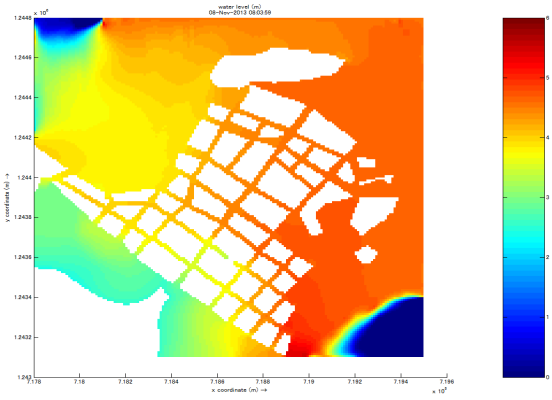

Figure 6: inundation map during the surge peak (08-Nov-2013 08:04:00)

4. Conclusions

In this research, we conducted the field survey and performed the numerical analysis to assess the characteristics of storm surge inundation in Tacloban. The numerical simulation considering buildings can estimate inundation and flow speed at a reasonable accuracy when Manning's *n* value is set to be 0.04. It was demonstrated that the street shielded by dense buildings could contribute to reducing flow velocity as well as inundation depth due to storm surges.

References

a) Takagi H. et al. (2014) Track Analysis, Simulation and Field Survey of the 2013 Typhoon Haiyan Storm Surge, *J. of Flood Risk Management*

b) JTWC best track joint Typhoon warning center. Retrieved 2014-11-30

c) MLIT (2012) Guide to determining the potential tsunami inundation (Version 2.00)

Batch Equilibrium Extraction of Model Petroleum Heavy fraction

Student Number: 11_22640 Name: Tomonori MASUDA Supervisor: Ryuichi EGASHIRA, Hiroaki HABAKI

1. Introduction

Some petroleum-derived heavy fractions contain not only homocyclic but also heterocyclic compounds at certain concentration, and the latter should cause degradation of fuel oil quality and be poisonous for catalysts used in the successive processes, such as hydrocracking, desulfurization and so on. Then the removal of these heterocyclic compounds from the heavy fractions has been studied for the catalytic reaction stably operated or improved, keep the quality of fuel oil.

Solvent extraction has been utilized as a commercialized method to separate aromatic compounds from petro-derived fractions. Separation of nitrogen heterocyclic compounds (Hetero) by solvent extraction has been studied, in which coal tar absorption oil or catalytic cracked oil was used as feed oil [2-4]. However the separation of heterocyclic compounds from the heavy fractions has been insufficiently investigated.

In this study, liquid-liquid equilibrium extraction of model heavy fractions with aqueous solutions of methanol was measured. The effects of species of Hetero and other coexisting components on the liquid-liquid equilibrium were studied.

2. Experimentals

2.1 Materials

The material systems used in this study are summarized in **Table 1**. The 3 types of nitrogen heterocyclic compounds (Hetero), such as quinolines (Qs), indoles (INs) and Carbazoles (CBZs),and 2 types of non-heterocyclic compounds (Non-hetero), such as aromatics and alkanes(AL), were selected and totally 21 components were used. For each type of Hetero, the carbon numbers in molecules were varied by changing their functional group. To prepare the model feed solutions of binary system, one each component was chosen from Hetero and Non-hetero components. The carbon number in the molecule, CN, was estimated by regarding heteroatom as carbon in the molecule. Aqueous methanol solution, one of the popular solvents used in the previous studies, was used as the solvent.

2.2 Experimental conditions

The experimental conditions are summarized in **Table 2**. The mass fraction of the Hetero component in the model binary feed solutions was set as 0.01. The specified amounts of feed, and solvent, were put in conical flask and shaken at 303K for 48 hours to be equilibrated. After reaching equilibrium conditions, the raffinate and extract phases and were separated into each other with separatory funnel. The liquid phases were analyzed by gas chromatograph (Shimazu GC-2010) with capillary column (HR-1) to determine respective compositions of both phases.

Table 1 Compounds in model systems

Hetero

Quinolines(Qs)
quinoline(Q, CN = 10), 2-methylquinoline(MeQ, CN = 11), 2,6-dimethylquinoline(DMeQ, CN = 12), 4-phenylpyridine (PhPYR, CN = 12), benzo[h]quinolone(BeQ, CN = 14)

Indoles(INs)
indole(IN, CN = 9), 2-methylindole(MeIN, CN = 10), 7-ethylindole(EtIN, CN = 11), 2,3-dimethylindole (DMeIN, CN = 11), 2-phenylindole(PhIN CN = 15)

Carbazoles(CBZs)
carbazole (CBZ, CN = 13), 9-methylcarbazole(MeCBZ, CN = 14), 9-ethylcarbazole(EtCBZ, CN = 15)

Non-hetero

Aromatics
1-metylnaphthalene(1MeN, CN = 11), butylbenzene (BuBEZ, CN = 10)

Alkanes(AL)
decane(C10, CN = 10), undecane(C11, CN = 11), dodecane (C12, CN = 12), tridecane(C13, CN = 13), tetradecane(C14, CN = 14)

Table 2 Experimental conditions

System			
Feed	Model heavy fraction		
Solvent	Methanol aqueous solution		
Conditions			
Mass of feed, R_0		[kg]	0.02
Solvent/feed ratio, E_0/R_0		[-]	1
Mass fraction of Hetero $y_{Hetero,0}$		[-]	0.01~0.2
Mass fraction of methanol in solvent $y_{MeOH,0}$		[-]	0.8
Temperature		[K]	303
Time		[h]	48

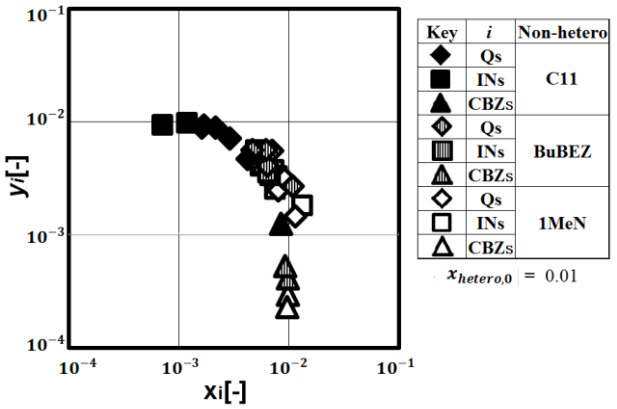

Fig.1 Mass fraction of Hetero in raffinate and extract phase

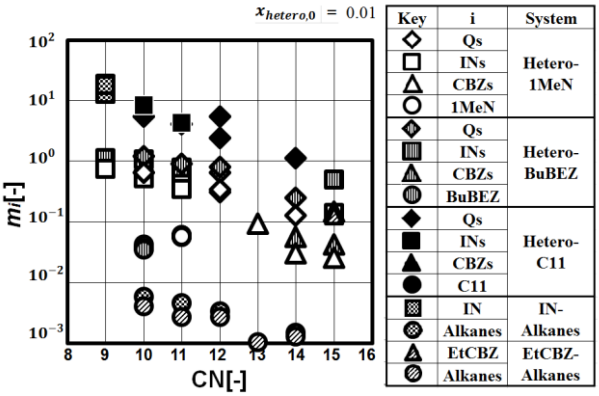

Fig.2 Effect of carbon number on distribution ratio, m_i

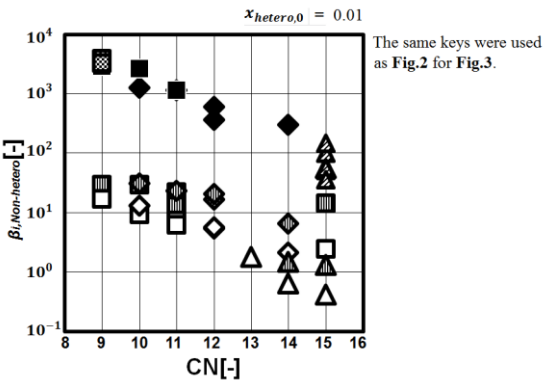

Fig.3 Effect of carbon number on selectivity $\beta_{i,Non-hetero}$

3. Results and Discussion

3.1 Definitions

The distribution ratio of component i, m_i and the

selectivity of component i against Non-hetero, $\beta_{i,Nonhetero}$ is defined as follow:

$$m_i = y_{i,1}/x_{i,1} \quad (1)$$

$$\beta_{i,Nonhetero} = m_i/m_{Non-hetero} \quad (2)$$

Where $y_{i,1}$ and $x_{i,1}$ are the mass fractions of component i in each phases in extraction. Mass fraction excluding solvent in extract phase , z defined as follow:

$$z = 1 - y_{MeOH,1} - y_{W,1} \quad (3)$$

Where k is all compounds used in model systems and solvent, n is compounds used in solvent.

3.2 Equilibrium with model binary feed oil systems

In all cases, the liquid-liquid extraction could be stably operated and stable emulsion was not formed. The compounds of Q and C12, or MeQ and 1MeN could not be appropriately analyzed by gas chromatogram since they could not be separated by the used column in the gas chromatogram.

The plots of the mass fractions of Hetero components in the extract phases against those in the raffinate phases are shown in **Fig.1**. The $y_{i,1}$ of Hetero components were larger with C11 than in 1MeN-hetero systems. The $y_{i,1}$ of Qs and INs were relatively high and those of CBZs were small with each Non- hetero component.

The effect of CN on m_i, is shown in **Fig.2**. In most case, m_i decreased as CN increased and m_i of Hetero components were larger than those of Non-hetero components. Among Hetero components, m_i of Qs and INs were almost comparable with each other, and were larger than those of CBZs. The m_i of Hetero components were the largest with C11, followed by those with BuBEZ and 1MeN. The m_i of Non-hetero components were independent of the coexisting Hetero components to be constant for respective Non-hetero components. The m_i was the smallest with C11, followed by BuBEZ and 1MeN.

The effect of CN on $\beta_{i,Non-hetero}$ is shown in **Fig.3.** The $\beta_{i,Nonhetero}$ decreased as CN increased. The $\beta_{i,Nonhetero}$ was the largest with C11, followed by those with BuBEZ and 1MeN, and $\beta_{i,Nonhetero}$ of IN with C11 attained more than 2800. This so high selectivity might be caused by the water content in extract phase.

Figure 4 shows the effect of z on m_Q and m_i of Non-hetero components when $x_{Q,0}$ was varied from 0.01 to 0.2. In lower range of z, m_Q decreased and m_i of Non-hetero component increased as z increased. With less polar component, such as C11, more polar component, such as Q, preferably dissolved into the solvent phase. The difference between m_i of Q and C11 was quite large and the ratio, m_Q/m_{C11}, was more than 1200. This characteristic feature became obscure in the order of C11, BuBEZ, and 1MeN, that is to say, the ascending order of the mass fraction of Non-hetero component in the extract phase. In the higher range of z, although m_Q was kept constant, m_{1MeN} increased with z. When both components in the binary system are likely to dissolve into solvent phase, the solubility of less polar component should be enhanced by the other more polar component. This trend was also reported in the previous studies[8].

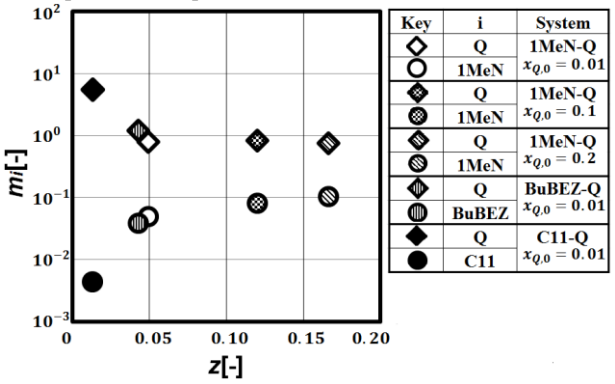

Fig. 4 Effect of mass fraction excluding solvent in extract phase for distribution ratio

3.3 Extraction of model multicomponent feed oil system

The results with the multicomponent system are shown in **Fig.5,** when 1MeN was used as Non-hetero compound. The m_i of Hetero components were larger than m_i of Non-hetero in 2 components systems, because total initial mass fraction of Hetero component in multicomponent system was larger than that of Hetero component in 2components systems. So, the tendency of 2 components systems was same as that of multicomponent system.

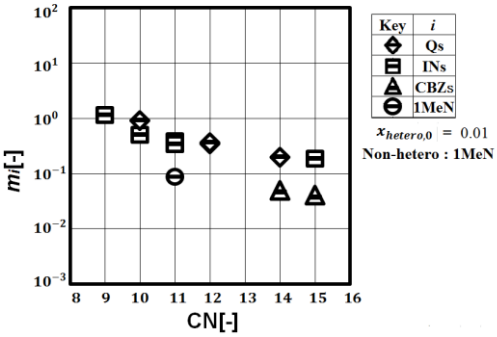

Fig. 5 Effect of CN for distribution ratio in multicomponent system

4. Conclusion

Batch Equilibrium of nitrogen heterocyclic compounds, alkanes and aromatics were measured on 2 component systems. As CN increased, distribution ratio of Hetero and alkanes decreased. Distribution ratio of CBZs were smaller with each Non- hetero components than that of INs and Qs. Distribution ratio of Hetero was larger than that of aromatics, and that of aromatics was larger than that of alkanes. The selectivity of Hetero against alkanes was largest, followed by those with BuBEZ and 1MeN.

The distribution ratio of Hetero was smaller with aromatics than that of Hetero with alkanes. The solubility of less polar component was enhanced by the other more polar component.

The liquid-liquid equilibrium in 2 compounds systems and multicomponent system was almost comparable with each other.

Nomenclature

CN = carbon number of compounds, x_i = Mass fraction of i in raffinate phase, y_i = Mass fraction of i in extract phase, m_i = Distribution ratio of i

1MeN = 1-methylnaphthalene, BuBEZ = Buthylbenzene, C10 = Decane, C11 = Undecane, C12 = Dodecane, C13 = Tridecane , C14 = Tetradecane, Q = Quinline, DMeQ = 2,6-dimethylquinline, MeQ = 2-methylquinoline, PhPYR = 4-phenylpyridine, BeQ = benzo[h]quinline, IN = Indole, MeIN = 2-methylindole, EtIN = 7-ethylindole, DMeIN = 2,3-dimethylindole, PhIN = 2-phenylindole, CBZ = Carbazole, MeCBZ = 9-methylcarbazole, EtCBZ = 9-ethylcarbazole, MeOH = Methanol, W = Water, Qs = Quinoline compounds, INs = Indole compounds, CBZs = Carbazole compounds, Hetero = Heterocyclic compounds, Non-hetero = alkanes and aromatics, AL = alkanes

Subscript

i : component i, 0 : at initial state, 1 : at equilibrium state

Reference

[1] Nagai.M 東京工業大学 1999 年卒業論文

[2] Yoshimura.Y Solvent Extraction Research and Development, Japan, **20**, 169~174 (April, 2013)

[3] Chris. S 東京工業大学大学院 2000 年卒業論文

[4] Hasegawa.H, 東京工業大学 2014 年卒業論文

[5]石油学会;石油精製プロセス,第五章,接触分解 125-138

[6] Kim. C.J, Won.D.B, Fluid Phase Equilibria 193 (2002) 217–227

[7] George.W.M, Dennis.R.H, Ind. Eng. Chem. Res. (2008), 47, 2867-2875

[8] Chris.S et al, J.Jpn. PetInst, 48, 60-66 (2005)

The effect of non-policy factors on the diffusion of EV

Student Number: 11_01714 Name: Junya Ishida Supervisor: Naoya Abe

1. Introduction

Electric vehicle (EV) is one of the key options for the automobile sector to save energy consumption and reduce emissions mainly because it uses electricity as its power source. Anticipating the future where renewable energy will account for greater portion of electricity source, further contribution from EV in creating a cleaner environment is expected. Thus, the diffusion of EV is a great concern and interest in the world. Despite of its promising role, the diffusion of EV is still at an early stage. Previously, some researchers tried to find out the key factors of EV diffusion. Sierzchula et al. (2014) revealed positive effects of financial incentives, charging infrastructure, and local manufacturers. Tagashira et al. (2013) pointed out the complaints made by EV drivers including short cruising range and the inconvenience of charging that is done away from home, but there are also positive points of EV such as low running cost and charging at home. Looking back at the former EV's failed diffusion movements, Tsuchiya et al. (2010) claimed that it is important to create scenarios that are suitable with consumers' lifestyle and needs.

The primal cause of the short cruising range is that the capacity of battery is small. However, there are also other factors that can worse cruising range. These are temperature and slope. Using an air conditioner and driving EV on a steep slope require extra consumption of electricity. Although these do not affect only to EV, its short cruising range makes it more serious for EV. Moreover, since Japan is a stretched and mountainous island country from north to south and mountainous, those factors possibly have stronger effects in some specific regions. Especially for EV users in cold and mountainous districts, running out of battery electricity could be a bigger anxiety due to safety reasons. It is assumed that temperature and slope affect not only actual cruising range but also consumer's sense of danger. By deepening the understanding of the effect of non-policy factors on the EV diffusion, which are often out of our control, we can improve the policy strategies such as realignment of area-targeting to realize more effective subsidy scheme.

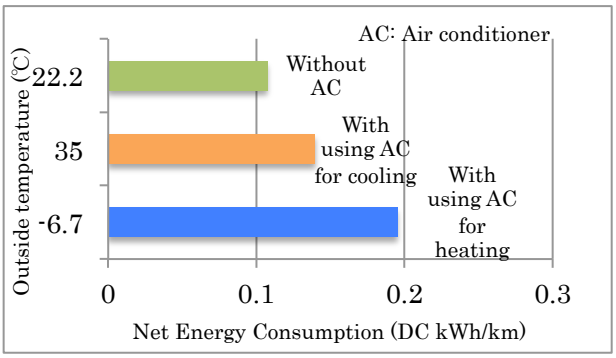

Figure 1: Urban Dynamometer Driving Schedule (UDDS) Test for Nissan Leaf 2013 SV. Source: [1]

2. Purpose

The purpose of this paper is to investigate whether or not non-policy factors, such as temperature and slope, affect the actual diffusion of EV. People in some districts could have disadvantages in terms of cruising range. However, there is no research that focuses on those local differential impacts for the actual diffusion of EV. In this paper, the hypothesis is that low temperature and steep slope would negatively affect consumer preferences and hinder the actual diffusion of EV in cold or mountainous districts.

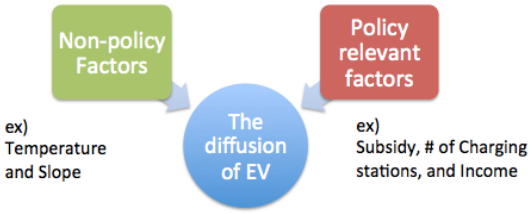

Figure 2: Concept of this study

3. Methodology

Multiple regression analysis was conducted, targeting municipalities in Japan. Dependent variables (y) and independent variables (x, z, w) are set as below.

Table1: Variables

y_1	The number of retained EV (cars)
y_2	The number of retained EV per 1,000 persons (cars/1,000 persons)
x_1	The average temperature (℃)
x_2	The average highest temperature (℃)
x_3	The average lowest temperature (℃)
x_4	The average temperature in summer (℃)
x_5	The average temperature in winter (℃)
x_6	The annual average number of days whose maximum temperature is more than 30 ℃ (days/year)
x_7	The annual average number of days whose maximum temperature is less than 0 ℃ (days/year)
x_8	The annual average number of days whose maximum temperature is more than 25 ℃ (days/year)
x_9	The annual average number of days whose minimum temperature is less than 0 ℃ (days/year)
z_1	The average slope of residential areas (°)
z_2	The average slope of nonresidential areas (°)
w_1	The number of households (household)
w_2	The number of person per habitable area (person/km^2)
w_3	The income index
w_4	The number of charging station per habitable area (station/km^2)
w_5	The ratio of detached house against all houses

w_6	The number of passenger cars per household (cars/household)
w_7	Electricity price in midnight (JPY/kWh)
w_8	Gasoline price (JPY/L)
w_9	Subsidy (Dummy)
w_{10}	EV・PHV town (Dummy)

Here, "EV" is a car classified into standard-sized passenger car, and the data of EV is as of March 2014. [2] Temperature factors (x) are the average from 1981 to 2010. [3] The data of slope was summarized in 2005. [4] The data of household and population is as of January 2014. The data of charging station is as of March 2014. The data of house is as of 2008. Electricity price is the average from 2010 to 2012. Gasoline price is the average from 2010 to 2013. Subsidy is what was enforced from 2012 JFY to 2013 JFY.

Although there are approximately 2,000 municipalities in Japan, the sample number is 85 due to the limited availability. There are 9 variables in the temperature category and 2 variables in the slope category. One variable was chosen from each category. All of the combination was simulated in each model. y_1, y_2, and x_1 were applied to logarithmic transformation to cope with heteroskedasticity of the residuals. Most of the independent variables follow the normal distribution. Model 2 does not include x_3 because y_2 is ratio against people.

$$Model\ 1: \ln y_1 = \beta_0 + \beta_1 x_1 + \beta_2 x_2 + \beta_3 \ln x_3 + \beta_4 x_4 + \beta_5 x_5 + \beta_6 x_6 + \beta_7 x_7 + \beta_8 x_8 + \beta_9 x_9 + \beta_{10} x_{10} + \beta_{11} x_{11} + \beta_{12} x_{12} + \varepsilon$$

$$Model\ 2: \ln y_2 = \beta_0 + \beta_1 x_1 + \beta_2 x_2 + \beta_4 x_4 + \beta_5 x_5 + \beta_6 x_6 + \beta_7 x_7 + \beta_8 x_8 + \beta_9 x_9 + \beta_{10} x_{10} + \beta_{11} x_{11} + \beta_{12} x_{12} + \varepsilon$$

(β is coefficient, and ε is residual, assumed as to follow the normal distribution.)

4. Results and areas for further study

Table 2 shows the regression analysis results. The adjusted R^2 of model 1 is much higher than that of model 2. Temperature factors, except for x_9, have negative effect on the diffusion and are statistically significant at 1% level in all cases. The number of charging station per habitable area has positive effect on the dependent variable and is statistically significant at 5% level in all the cases of model 1 when z1 was chosen. In the model 2, it is significant whether z1 or z2 was chosen. The number of passenger cars per household has positive effect and is statistically significant at 5% level in all cases of model 1. The other factors hardly show statistical significance. Now, the effects of some variables in those models are understood. When temperature factors and the number of charging station per habitable area increase, there are more the number of retained EV and the number of retained EV per 1,000 persons. When the number of passenger cars per household increases, the number of retained EV enlarges. In addition, the impacts of temperature factors and the density of charging station is almost the same.

5. Conclusion

In this paper, we statistically found that low temperature negatively affected the actual diffusion of EV in Japan. On the other hand, slope did not have effect on the diffusion of EV. Now, it is suggested that the local differential effect derived from temperature should be considered for better diffusion strategies of EV.

Table 1: Normalized beta coefficients

	Model 1		Model 2	
VARIABLES	1	2	1	2
x1	0.145***	0.134***	0.363***	0.331***
z1	-0.0464		-0.168	
z2		-0.0179		-0.0354
w1	0.990***	1.00***		
w2	-0.178*	-0.160	-0.422*	-0.331
w3	0.0849	0.0897	0.242	0.274*
w4	0.138**	0.121**	0.376***	0.323**
w5	0.00566	0.000241	0.0165	-0.00587
w6	0.259***	0.276***	0.335*	0.393**
w7	-0.0766	-0.0803*	-0.161	-0.176
w8	0.028	0.0225	0.123	0.101
w9	-0.0273	-0.025	-0.0497	-0.0401
w10	-0.0345	-0.0305	-0.176*	-0.168
adj R2	0.868	0.867	0.311	0.289
F-value	47.11***	46.53***	4.441***	4.106***
*** p<0.01, ** p<0.05, * p<0.1				

Example of policies incorporating temperature effects are as follow: ①Cold districts should be supported more strongly than the other regions. ② Since EV is not appropriate for cold districts, other types of vehicle, such as fuel cell vehicle, should be promoted in these areas. ③ In cold districts, EV may survive in specific business or activities, for example, postal service and bus service.

There are some limitations in this study. It does not consider consumers' individuality. People in a municipality are regarded as the same. In addition, as written above, the diffusion is still at an early stage. Therefore, the next phase might show a different trend. The transition should be followed.

References

Sierzchula et al., (2014), The influence of financial incentives and other socio-economic factors on electric vehicle adoption

Tagashira et al., (2013), A User Survey of Plug-in Hybrid and Battery Electric Vehicles

Tsuchiya et al., (2010), Transition of the Diffusion Policies and their Impacts with the Market on Electric Vehicle in Japan

[1] Argonne National Laboratory Transportation Technology R&D Center, Advanced Powertrain Research Facility Downloadable Dynamometer (D3)

[2] Automobile Inspection & Registration Information Association

[3] Japan Meteorological Agency, The past meteorological downloadable database

[4] Zaiki et al., (2005), "Relationship between Distribution of Japanese Residential Areas and Topography"

DISSIPAITION ENERGY IN THE PROCESS OF ADHESION AND DETACHMENT BETWEEN ELASTIC BEAM AND RIGID BODY

Student Number: 11-08604 Name: Takeru KUSAKARI Supervisor: Kunio TAKAHASHI

1 Introduction

Hysteresis is frequently observed in adhesion phenomena. It is significant and essential to understand the mechanism of the hysteresis, in the design of devices, such as grip-and-release devices.

The hysteresis is the difference between loading and unloading process. Based on a point contact model, Beak [1] suggested that energy dissipation is never observed in the loading processes and dissipation energy appears in the unloading processes. Furthermore the dissipation energy is proportional to the contact edge length. In the experiments [1], the contact edge length varies every moment, so, complicated calculation is required to consider the mechanism of energy dissipation using.

In the present study, the contact model between an elastic beam and rigid body is used to fix the contact edge width to simplify the geometry. And the dissipation energy is measured to discuss the mechanism of the hysteresis.

2 Method of Calculating Dissipation Energy

Fig.1 shows the model used in the present study. f_z, is the force and d is the displacement, and $\Delta\gamma$ is the work of adhesion between the beam and the substrate. l is the length of non-contact area of the beam, which has the angle θ, the width W, length L, Young's modulus E, and the moment of inertia I. In order to calculate the dissipation energy, the equation (1) can be used,

$$\Delta U_{dis.} = \Delta U_{ext.} - \Delta U_{el.} - \Delta U_{int.} \quad (1)$$

where $\Delta U_{dis.}$, is the dissipation energy, $\Delta U_{ext.}$ is the external work from the outside, $\Delta U_{el.}$ is the elastic energy stored in the elastic beam, $\Delta U_{int.}$ is the energy come from the $\Delta\gamma$. These energy can be calculated by using equations (2)~(4)[2].

$$U_{\text{ext.}} = \int f_z \mathrm{d}\, d \quad (2)$$

$$U_{\text{el.}} = \frac{6EI}{l\cos^2\theta}\left(\frac{d}{l} + \frac{1}{2}\sin\theta\right)^2 + \frac{EI}{2l}\tan^2\theta \quad (3)$$

$$U_{\text{int.}} = -W(L-l)\Delta\gamma = W\cdot\Delta l\cdot\Delta\gamma \quad (4)$$

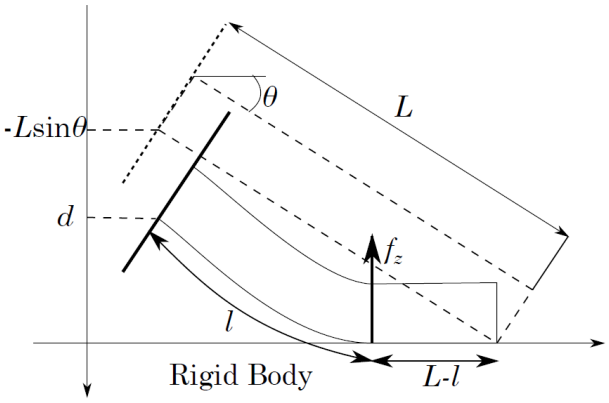

Figure.1 Schematic illustration of the contact model

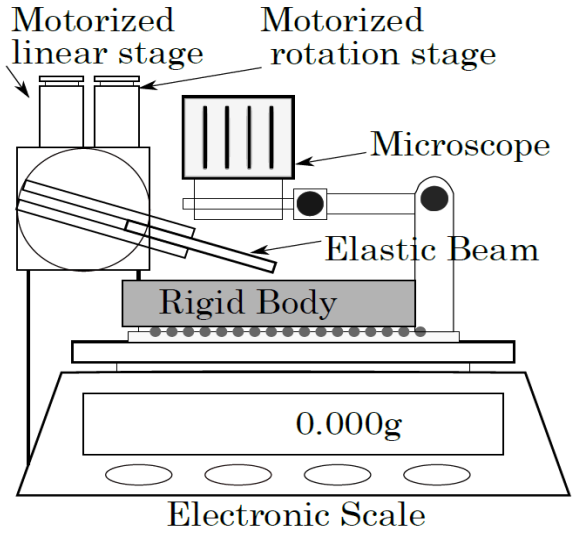

Figure.2: Schematic illustration of the experimental system

3 Experiment to Measure Dissipation Energy

In order to calculate dissipation energy by using equations (2)~(4), it is necessary to measure the force f_z, the displacement d, and the length of not-contact area l experimentally. In the presant study, an experimental system like Fig.2 is used for measuring these parameters. The stepping motor is operated to load and unload the beam by 50μm per step. The displacement is set to zero when the beam starts contacting the rigid body. There are

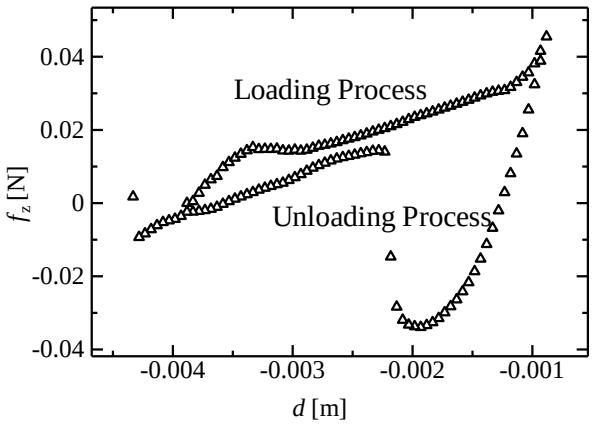

Figure.3 Experimental results of relation between the force and the displacement

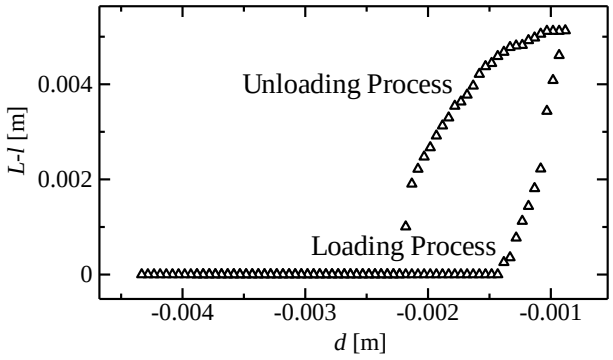

Figure.4 Experimental results of relation between the length of contact area and the displacement

60 steps of loading process and we unload the beam until it detaches from the rigid body. The duration of waiting time between each step is 60 seconds. By using electronic scale, the force f_z is measured. By using microscope, the length of not-contact area l is observed. In this study, we use PDMS as the elastic beam and slide glass as the rigid body. And in this study, because the friction force between the beam and the rigid body is neglected, steel balls which diameter is 5 mm are set under the rigid body.

4 Results and Discussion

The relation between the force and the displacement is measured like Fig.3. And then, the length of contact area is measured like Fig.4. By using these measured parameters, the dissipation energy can be calculated. In the present study, the same experiment was conducted three times and the calculation results of the energy dissipation per variation in the length of non-contact area are shown Fig.5 As Fig.5 shows, the dissipation energy is

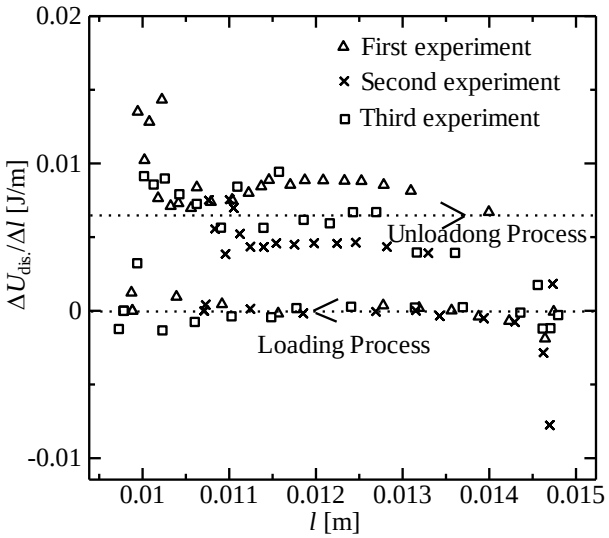

Figure.5 Experimental results of the dissipation energy as a relation of variation in the not-contact area Δl in the whole process

nearly zero in the loading process. And the dissipation energy in the unloading process is nearly fixed. We can think that, in the unloading process, some constant force works to the contact edge, and this force causes the constant energy dissipation. But from the results, the mechanism of this force has not been revealed yet. So we have to reveal it experimentally in future. In order to reveal the mechanism, this beam model can be useful, because the length of the contact edge where this force works is fixed in this model, although it is various in the point contact model.

5 Conclusions

The dissipation energy in the process of adhesion and detachment between elastic beam and rigid body is measured experimentally. And because the energy dissipated constantly in the unloading process, we suggest that some force works to the contact edge in the unloading process. But the mechanism of this force hasn't been revealed. In order to consider the mechanism, this model is useful.

References

[1] D.Beak, et al., a master thesis of Tokyo Institute of Technology(2013)
[2] Y.Sekiguchi, et al., International Journal of Adhesion & Adhesive 49(2014)

方向適応変換による画像符号化のための係数予測に関する研究

学籍番号: 11_12445　　名前: 朱正奇　　指導教員: 山下幸彦

1　はじめに

本研究の画像符号化のための係数予測は OAVEKLT (Orientation Adaptive Karhunen-Loeve Transform)[3] をもとにし，現在処理中の画像ブロックを処理済みのブロックの画素値を使って予測する方法である。自然画像において隣接するブロック同士は互いに強い相関関係を持っているため，ターゲットブロックの OAVEKLT 係数はその隣接のブロックの境界の画素値との最小二乗解によって予測することができる。この方法によって，エントロピー符号器に送るものをターゲットブロックのもとの OAVEKLT 係数と予測係数の差にできる。予測が正確であれば，この差が小さくなり，符号化において要する符号量が少なくなる [4]。従って理論的には係数予測によって符号化効率が向上する。しかし，係数予測を画像符号化の手法として実用化するためには，符号量の効率が実際に向上したか，どのくらい向上したか，予測がどのくらい正確であるか，予測がどのようなところで正確であるか，予測は OAVEKLT のパラメータによってどう変化するのかという様々な課題に答えなければならない。本研究はこのような課題に答えるために，３種類の実験を複数の画像を用いて行い，係数予測の効果を調べた。

2　係数予測

OAVEKLT は，DCT (Discrete Cosine Transform)[1] の変換基底をいくつかの角度で回転し，得られた基底の中で，ブロックごとに低い周波数の領域で最も画像情報量 [2] が多く保たれている基底を選択し，変換を行う方法である [3]。この方法により画像の各方向のエッジを適切に符号化することができる。

画像符号化を行う際，一般的には画像をいくつかのブロックに分けて，右ブロックから左へ順番にブロックごとに処理を行う。ターゲットブロックを処理する際，その隣接のブロックの画素ベクトル $\vec{g}$ は取得することができる。係数予測は処理済みのブロックの画素ベクトル $\vec{g}$ を用いてターゲットブロックの OAVEKLT 係数を予測する方法である [4]。

ブロックが隣接しているため，ターゲットブロックの OAVEKLT 基底を延長を延長して求めたその隣接ブロックの画素値 $\vec{g}$ と隣接ブロックの本当の画素値との差は小さいはずである。つまり予測係数を $\vec{a_i'}$ とする場合，隣接のブロックの本当の画素ベクトル $\vec{g}$ とターゲットブロックの予測係数と延長した変換基底 $\vec{v_i}$ を使って求めた $\vec{g'} = \sum_i a_i' \vec{v_i}$ との差が最小になる必要がある。従って，$||\vec{g} - \vec{g'}||^2$ の最小二乗解 $\vec{a_i'}$ を求めればよい。すなわち，$V = [v_1, v_2 ... v_i ...]$ とおけば，予測係数は $\vec{a'} = (V^T V)^{-1} V)\vec{g}$ で求まる [4]。

普通の OAVEKLT の符号器は OAVEKLT を行った後，OAVEKLT 係数を量子化し，直接エントロピー符号化を行うが，係数予測を取り入れた符号器は，OAVEKLT 係数を量子化した後，逆量子化と OAVEKLT の逆変換を使い，次のブロックの予測に供する隣接ブロックの画素ベクトル $\vec{g}$ を求める。そして係数予測を行い，もう一回量子化を行う。最後にエントロピー符号化器に送るものはもとの OAVEKLT 係数と予測係数の差である。予測が正確であるほど，この差が小さくなり，少ないビット数で符号化できる。復号器においても同様な処理を行い，全体的に符号化の効率を向上させることができる。

3　符号化実験

実験１では予測精度と送信符号量の差の関係を定量的に分析する。各ブロックにおいての予測誤差と送信符号量変化を抽出し，その関係を比較した。実験２では予測の精度に影響する要因を分析する。予測の精度に影響する要因として以下のように２つ仮定し，実験によってそれらの仮定を検証した。仮説１：ターゲットブロックの画素値の分散が小さいほど，その隣接のブロックの相関関係が強い。仮説２：隣接のブロックの境界の画素ベクトルの相関係数が大きいほど，隣接のブロックの相関関係が強い。実験３では OAVEKLT のパラメータによる違いを比較する。係数予測は OAVEKLT に基づく方法であるため，本実験は重要なパラメータである Bit Rate と OAVEKLT の変換基底の種類数 K が係数予測にどのような影響を与えるかを分析した上で，係数予測の精度を向上させるための OAVEKLT のパラメータ設定を調べた。この 3 種類の実験から得られた結果の一部を以下の図で示す。

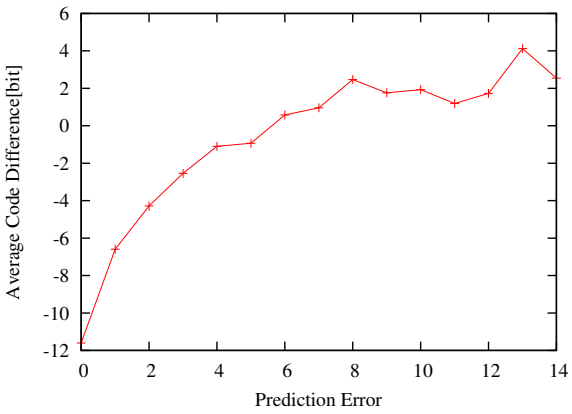

図 1: 予測誤差と符号量差の平均の関係

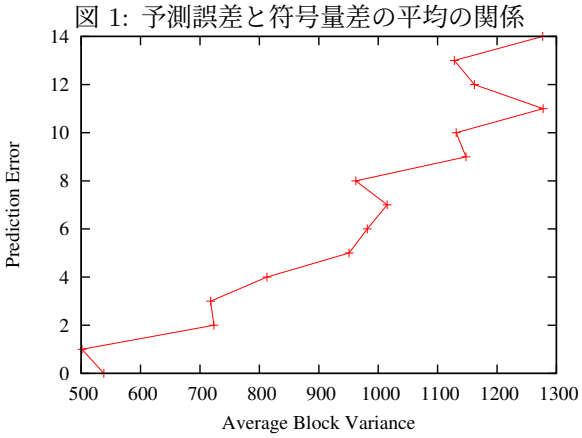

図 2: ブロック分散の平均と予測誤差の関係

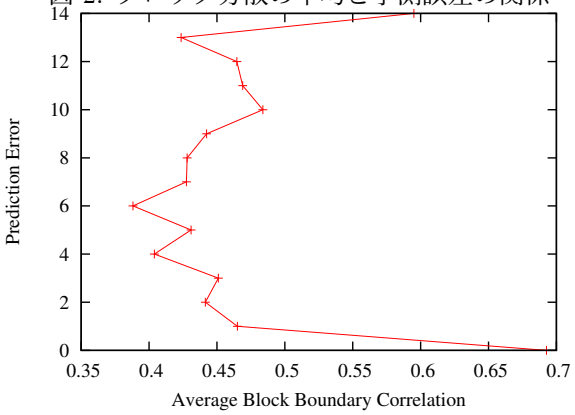

図 3: ブロック境界相関係数の平均と予測誤差の関係

図 1 より予測誤差と符号量の差の平均の間に単調増加が示された。他の実験画像についても同様な結果が得られたため，予測精度を向上させることは符号化の効率の向上につながることがわかる。図 2 より，ブロックの分散の平均と予測誤差の間に単調増加が示された。他の実験画像についても同様な結果が得られたため，入力画像において平坦な領域で予測精度が正確になることがわかる。図 3 より，ブロックの境界画素ベクトルの相関係数の平均と予測誤差の間は簡単な形がなく，他の実験画像においても，同様な結果が得られることが多い。しかし，図 3 の点は散らばらず，断続的に単調増加と単調減少が交互に示された。このような特性が現れた理由は今後の課題である。図 4 より，

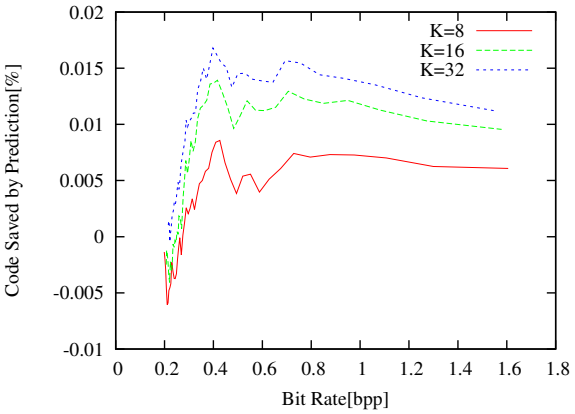

図 4: Bit Rate と減少した符号量%

Bit Rate が低い領域では，係数予測の精度は K の値によってあまり変化しなかった。しかし Bit Rate が大きくなると，係数予測精度の差が開いた。Bit Rate がおよそ 0.3-0.4 のところでピークを迎え，それからまた小さくなった。K=32 の時，係数予測の精度が一番よいが，計算時間もかかる。今回の実験によって，中程度の画質の画像を出力する場合，K の値を高く設定することが効果的であることがわかった。

4 おわりに

今回は符号化実験において多数の視点から係数予測の精度を分析した。係数予測の精度をさらに向上させるには，実験 2 の結果に基づき，ブログの分散を閾値とする係数予測の選択法を開発すること，さらに実験 3 の結果に基づき，出力画像の画質，符号量，計算時間の 3 者のバランスについても研究するこることが必要である。

参考文献

[1] N. Ahmed, T. Natarajan, and K.R. Rao, “ Discrete cosine transform, ” IEEE Transactions on Computers, vol. COM-25, pp. 90-93, January 1974

[2] H. Ogawa,”Karhunen-Loeve subspace,” Proc. 12th Int. Conf. on Pattern Recognition, vol.2 pp.75-78, Hague, Netherlands,1992

[3] T.tanaka and Y.Yamashita, ”Vector-Embeded Karhunen-Loeve Transform and its application in Orientation Adaptive Coding of Image,” vol.E83-A,No.6, pp. 1257-1266, june 2000

[4] Gaudencio G.BanSIL,Jr.,Dr.Yukihiko Yamashita, ”Image Coding by Orientation Adaptive Transform with Prediction,” Master Thesis, Tokyo Tech, 2014

Diffusion of Electric Vehicles and Charging Infrastructures: The Current Condition in Japan

Student Number: 10_01958 Name: Masaaki Ichimura Supervisor: Naoya Abe

1 Introduction

Electric Vehicles (EVs) is a technological innovation that is thought to be a valid measure to reduce greenhouse gas emissions. However, the current EV adoption rate is very low in Japan. One of the possible barriers of EV diffusion is its limited cruising range. While some studies (Neubauer and Wood, 2014) had shown that substantial charging infrastructures allow to overcome barriers to EV adoption, it is also assumed that charging infrastructures are necessary conditions to increase the number of EVs. That is, diffusion of EVs and charging stations are in a dilemma. To solve this problem, there is a need to clarify the relationships between EV diffusion and increase of charging stations.

Not only the number of charging stations, but its placement is also a big deal on EV diffusion. Actually there are many studies about optimal placement of charging stations (Central Research Institute of Electric Power and Kozo Keikaku Engineering, 2011). However, these studies had not compared with the ideal placement and the actual situation. There are possible gaps between ideal and real placement. If gaps exist, there is a need to consider how to overcome the gaps.

Based on these backgrounds, the objectives of this study are:

1) To clarify the influence of increase in the number of charging stations to support EV diffusion

2) To clarify the actual state of charging stations placement

In Objective 1, this study targets Japan's all prefecture, therefore, the number of samples is N=47. And then, in Objective 2, this study had researched Kanagawa Prefecture, which is most successful prefecture in terms of diffusion state of charging station. This study had collected data of the normal and fast charger. The sample number of the normal and fast chargers are N=264 and N=234 respectively.

2 Literature Review

Sierzchula et al. (2014) had studied the effect of economic and social factors on EV adoption rate with Ordinary Least Square (OLS) regression model. The study had shown that the number of charging stations is significant on EV market share, but the correlation is weak. The study noted that the substantial charging station may be effective but does not ensure EV diffusion.

Central Research Institute of Electric Power and Kozo Keikaku Engineering (2011) had analyzed optimal placement by simulating EV driving pattern. The study had shown that the placement of charging stations should be more concentrated on the densely populated area than on the roadside at the beginning of EV diffusion.

3 Methodology

3.1 Multiple Regression (Objective 1)

In order to estimate the influences of various variables that are thought to have some influences on EV diffusion, multiple regression was conducted. The expression of the MR model is following:

$$\begin{aligned}\mathrm{EVshare}_i = \alpha &+ \beta_1 chginf_i + \beta_2 income_i \\ &+ \beta_3 EVcost_i + \beta_4 GEVcost_i \\ &+ \beta_5 \mathrm{EV\_PHVtown}_i + \beta_6 density_i \\ &+ \beta_7 carposess_i + \varepsilon_i\end{aligned} \quad (1)$$

ε_i: residual, α: intercept, i: sumple number

By using OLS, we could estimate the regression coefficient β_k(k: coefficient number). The definitions of independent and dependent variables in this model are shown in the Table 1.

Table 1. The definitions of variables

Variables	Definition
EVshare [%]	Market share of EV as a percentage of all cars
Chginf [/ 100 km^2]	The number of charging stations per 100 km^2
Income [¥]	Average monthly income per capita
EVcost [¥]	Estimated annual running cost of EV
GEVcost [¥]	Estimated annual running cost of Gasoline Engine Vehicle (GEV)
EV_PHVtown	Information about participant or not of Japanese demonstration project "EV-PHV town": expressed on 2-way variables (1 or 0)
Density[/ km^2]	Population density
Carposess	The number of car per household

3.2 Quantification Method Ⅲ (Objective 2)

Quantification Method Ⅲ (QMⅢ) is one type of the Multivariate Analysis. QMⅢ gave score to category and sample respectively. With the scatter diagram of category score or sample scores, we can see the characteristics and relationships of the category and sample.

By assessing the location information of the actual charging stations, this study depicts the characteristics of charging station location of Kanagawa Prefecture. This study set 26 categories elaborated in Table 2. Categories such as "Category 1 low-rise exclusive residential districts" are the term defined in the "City Planning Act" law. Again, the sample numbers of normal and fast chargers is N=264 and N=234 respectively.

Table 2. Categories of the placement of chargers

Categories	
Nissan car dealer	Category 1 low-rise exclusive residential districts
Toyota car dealer	Category 2 low-rise exclusive residential districts
Mitsubishi car dealer	Category 1 medium-to-high-rise exclusive residential districts
Other car dealer	Category 2 medium-to-high-rise exclusive residential districts
Commercial facility	Category 1 residential districts
Convenience store	Category 2 residential districts
Parking lot	Quasi-residential districts
Highway service area	Neighborhood commercial districts
Company	Commercial districts
Gas stand	Quasi-industrial districts
Distance from Main Road: ~250m	Industrial districts
Distance from Main Road: 250~500m	Exclusive industrial districts
Distance from Main Road: 500m~	Unknown districts

4 Results

4.1 Multiple Regression

Table 3 shows the results of the MR model. Model 1 is expressed by equation (1). In Model 1, income is only a significant variable. Since some variables seem insignificant, this study made Model 2 with least Akaike's Information Criterion (AIC). Model 2 is given as following equation:

$$\text{EVshare}_i = \alpha + \beta_1 chginf_i + \beta_2 income_i + \beta_4 GEVcost_i + \varepsilon_i \quad (2)$$

ε_i: residual, α: intercept, i: sumple number

In Model 2, all variables are significant but the adjusted R-square is apparently low. That is to say that the number of charging stations has a weak influence on EVshare.

Table 3. Result of Regression Model 1 and 2

Standardized Beta	Model 1	Model 2
Chginf	0.377	0.519**
Income	-0.651***	-0.531***
Carposess	0.19	
Density	0.368	
EV-PHVtown	0.146	
EVcost	0.147	
GEVcost	0.274	0.317**
Adjusted R-square	0.154	0.17
F-value	2.194*	4.138**
AIC	-170.04	-174.35

'***' P<0.01, '**' P<0.05, '*' P<0.1

4.2 Quantification Method Ⅲ (Objective 2)

Figure 1 and 2 display the scatter diagram of category score of normal and fast chargers placement. Interpretations of the axes are described with red characters. Figure 1 and 2 show that charging stations concentrate on the roadside. In Figure 1 and 2, categories locate everywhere, but clustered around the group encircled with blue circle. This group is composed of car dealers. That is, charging stations are allocated everywhere but concentrate on car dealers. Car dealers generally locate commercial and industrial district, so charging stations concentrate on these districts.

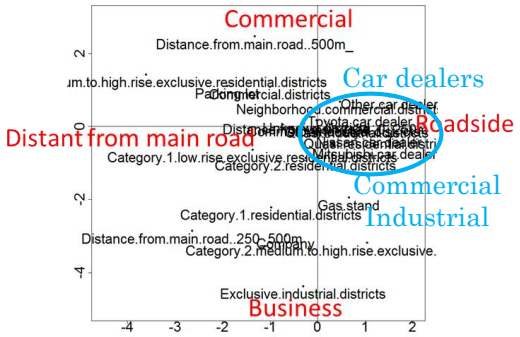

Figure 1. Category plot of normal chargers placement

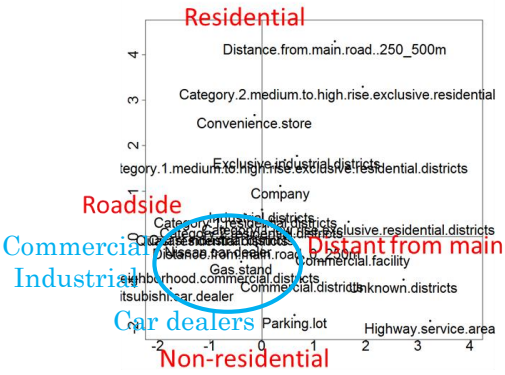

Figure 2. Category plot of fast chargers placement

5 Conclusion

5.1 Installation of charging station

This study had clarified the effect of number of charging stations on EV adoption. This effect is significant, but weak. Therefore, installing charging stations is not much effective on EV diffusion. There seems to be needs to help the operation more than installation of charging station.

5.2 Placement of charging station

This study revealed characteristics of charging stations placement. Charging stations generally locate roadside and commercial district, industrial district. These kinds of districts are relatively non-residential. So there are apparent gaps between actual and ideal placement.

References

[1] Neubauer, J., Wood, E., 2014, The impact of range anxiety and home, workplace, and public charging infrastructure on simulated battery electric vehicle lifetime utility, Journal of Power Sources 257 (2014)

[2] Sierzchula, W., Bakker, S., Maat, K., Wee, B., 2014, The influence of financial incentives and other socio-economic factors on electric vehicle adoption, Energy Policy 68 (2014)

[3] Central Research Institute of Electric Power and Kozo Keikaku Engineering, 2011, Analytical survey of the optimal placement of charging stations

Field survey and numerical analysis for floods in Ho Chi Minh City

Student number: 09_21527 Name: Shintaro Maeda Supervisor: Hiroshi Takagi

1. Introduction

Ho Chi Minh City (HCMC) is the biggest commercial city of Vietnam, experiencing rapid economy growth. HCMC is surrounded by Saigon River and Dong Nai River. Floods in HCMC show complex patterns influenced by sea tides in addition to rain falls and river discharge particularly in the rainy season from July to November. Since HCMC expands over the low-lying floodplain the elevation of which 1 to 3 meters above sea level, the city essentially has a great risk of the flood. In addition to this, sea level rise as well as heavy rain, which is expected to increase due to the global warming, could further increase the flood risk.

Besides many small floods, there were three large floods that occurred on 20th October, 7th November, and 4th December in 2013. Especially, the flood on 20th October is considered to be caused due to the highest tide for the past ten years.

To continue the economic growth, it is necessary for this city to take measures for reducing economic and social loss due to the flood. To reveal mechanisms of flood and find a clue for the countermeasures, the flood in HCMC was investigated by the field survey and numerical analysis.

2. Field survey in HCMC

To research the floods in HCMC, we conducted field survey in HCMC twice in dry (March) and rainy season (November) in 2014, accompanied by the members from Ho Chi Minh City University of Technology. We visited five places where are particularly considered to have high risk of the flood and conducted interviews to the residents and visit Dau Tieng reservoir. Figs.1 and 2 show the investigation sites and the photos during the surveys. The summary of the field surveys is as follows:

(1) Flood elevation can be influence by multiple factors such as heavy rain, high tide, reservoir operation, and inadequate drainage system.

(2) After the historical flood on 20th October, 2013, some countermeasures such as raising of the roads and the repair of drainage systems have been implemented.

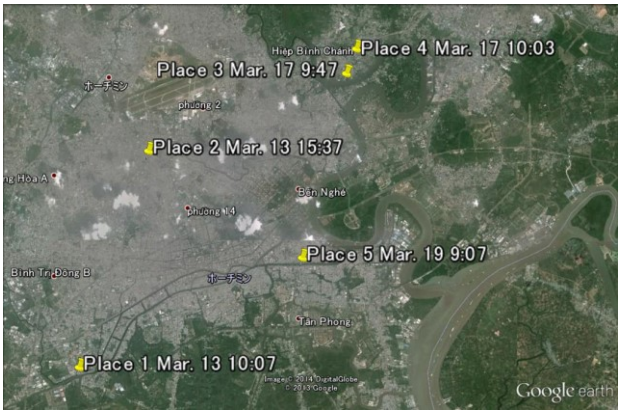

Fig.1 Investigation places

Fig.2 Field survey conducted in 2014

3. Analysis of tides

First, tides observed at Phu An Station and predicted astronomical tides were compared to estimate how high ocean tides influence the total water levels. It was found that actual water level shows 30 to 40cm higher than predicted tides (Fig.2). We investigated atmospheric pressure and precipitation, both of which seem to influence water level. However, strong correlations between them were not observed as shown in Fig.4.

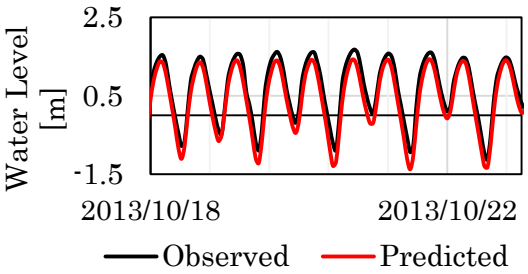

Fig.3 Observed tides and Predicted tides

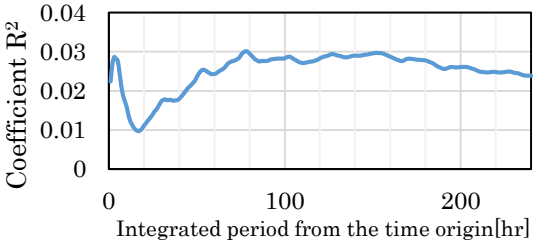

Fig.4 R^2 value between precipitation and adjusted water level considering atmospheric pressure

A moving average filter was applied to filter out tidal components from original water levels in order to examine the excess increases caused by the other mechanisms (Fig.5). The figure indicates that the excess component reaches up to 80cm. The period of the highest water level seems to correspond with the timing of the floods in 2013 (i.e. 20th October, 7th November, and 4th December).

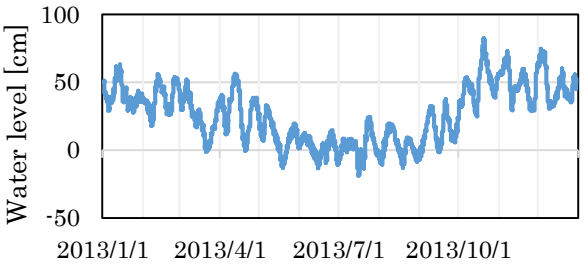

Fig5. Filtered observed tides

4. HEC-RAS model

To reveal the mechanisms of this excess water level, we hypothesized that the operation of two reservoirs in the outskirts of HCMC (Dau Tieng and Tri An) has an influence on water levels downstream, and performed a river simulation by using HEC-RAS model, which is commonly used for one-dimensional flow analysis. The river system developed is shown in Fig.6. The water level simulated (Fig.7) agrees well with the observed one, providing the reason of the excess water level about 80cm.

Fig.6 Two river systems connecting to HCMC

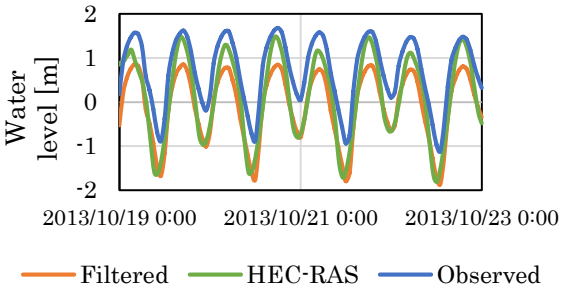

Fig.7 HEC-RAS water level analysis

The regression approximation that enables to estimate the water level was also obtained as follows:

$$Z = 0.001637X_1 + 0.001715X_2 - 1.16155 \quad (1)$$

where Z is the excess water level at Phu An associated with discharge from reservoir, X_1 discharge from Dau Tieng Reservoir, and X_2 discharge from Tri An Reservoir.

5. Conclusion

The floods in HCMC would occur by multiple mechanisms. Among many factors, we concluded that river discharge by reservoir operation particularly affected the water levels in 2013, in addition to daily ocean tides, whereas it seems that precipitation did not contribute significantly.

References

[1] High Tide Floods Ho Chi Minh City, http://floodlist.com/asia/high-tide-ho-chi-minh-city (Accessed on 15th Feb. 2015)

Study of multilingual semi-machine translation based on Collective Intelligence

Student Number：11B27085　Name：Wuning LI　Supervisor：Yukihiko YAMASHITA

1 Introduction

The Wiki system represented by Internet encyclopedia Wikipedia, which anyone can participate anytime, provides useful information continuously by collaboration in a wide area from the arts and sciences to life. However, there is the language barrier to prepare document file in every language in the present Wiki system. Machine translation is a solution in order that people all over the world can cross the barrier and acquire information from one document file, but machine translation has a problem that incorrect recognition occurs in syntactic analysis or semantic selection.

In order to enable high-accuracy translation, a technique called multilingual semi-machine translation based on Collective Intelligence was suggested. By this technique, an XML document is made using a support tool to add the information such as grammar and meaning, and is translated by an exclusive automatic translator to aim at the construction of the multilingual information service system. In this study, I develop a new web-based support tool to add the information such as parts of speech, grammar and meaning.

2 Semi-machine translation system by Adam document

Semi-machine translation system by Adam (Auxiliary Description to Attach Meaning) document enables that users add tags with the information to the original text on the Web. A computer translates these doucuments into plural languages based on the information on tags. Then we can read the web page by the multilanguage. The ducument which is added the tags with information is named Adam document and the machine translation system wthich translates Adam document into plural languages is named Lilith (LInguaL Interpreter To Human) system. Ishibashi [1] developed a support tool to make Adam documents. However this tool was written in Java and only works on the native environent. It also has problems. For instance, users have to add a spece between a word and a punctuation mark before dividing the original text. In this study, I develop a new web-based Adam document support tool by using Ajax.

Collective Intelligence is the count of the medley of a large quantity of information by many people, and it is treated as a synonym of 'the wisdom of the crowd' [2]. This concept means that a gathering of many opinions is more useful than a conclusion or the information making by few authorities, alternatively, leading to a right conclusion and prediction.

Adam document is a document of the XML form that provides the information of meaning, construction and grammar with tags. Mistakes during syntactic analysis or vocabulary interpretation which are the biggest factors of the mistranslation in machine translation disappears and highly accurate translation is enabled by the information. A writer who puts a tag on the original text is not necessary to be familiar with plural languages like a translator. Everyone who is familiar with the source language can do it easily.

Lilith system is a system which can decode tags on the word and translate an Adam document into any language by using a multilingual dictionary. This multilingual dictionary supports plural languages with the index of the source language before translation.

3 Adam document support tool by using Ajax

In this chapter, I explain the Adam document support tool by using Ajax that I developed.

Languages that I used for developing this tool are HTML, CSS, JavaScript and PHP. I have installed this tool in Web, and anyone can make Adam document using this tool by accessing the following Web address: http://eagle.ide.titech.ac.jp/crocofrog/Adam_js/

The main function of this tool is inputting a source

language (now only English), making an Adam document and saving the Adam document.

Figure 1 shows the opening screen on the web of this tool. Concerning that the object of the source language in this study is only English, users who make Adam documents can speak English to some extent. For this reason, I designed all the editing screens of this tool in English. In order to make edit areas plain, I divided it by colors so that users can edit syntactic information such as base form and parts of speech, semantic information and grammatical information easily.

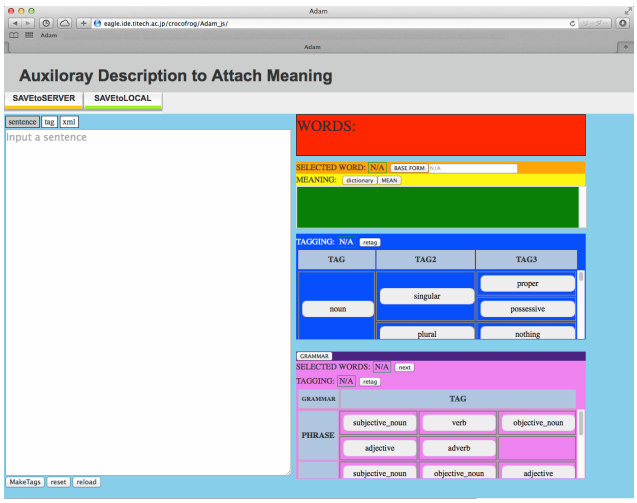

Figure 1: Opening screen on the Web

Black characters "Auxiloray Description to Attach Meaning" in the gray background on the top shows "ADAM" which is the title of this tool. And I located "SAVEtoSERVER" button and "SAVEtoLOCAL" button under the title. The Adam document is saved to the server when "SAVEtoSERVER" button is clicked. The file name is given by the clicked time automatically to prevent duplication of the file names. The Adam document is saved on the local directory when "SAVEtoLOCAL" button is clicked. And users can name the file freely.

The left part of of the screen is a domain for inputting the original text, and checking the tagged document and the Adam document. Left upper "sentence" button is gray when it is the initial state, and the color shows a chosen state. The text area of "Input a sentence" shows a area where users input a original text. And users can confirm the tagged document when "tag" is clicked and the Adam document is displayed when "xml" is clicked. I used Ajax to develop this tool so that the document that was carried out is almost to reflect at the same time and users can confirm progress of description here anytime. After users have input the original text and the "MakeTags" button in the lower left is clicked, the original text will be divided into words and they will be displayed after "WORDS". In addition, the text area will be reset when "rest" button is clicked, and the whole screen will be reloaded and return to the initial screen when the "reload" button is clicked.

The right part of the screen is a domain for giving syntactic information such as base form and parts of speech, and semantic information and grammatical information. "BASE FORM" button is for updating the information of base form of the word and "MEAN" button is for setting semantic information. Users will give the information of parts of speech when a button corresponding to parts of speech of the selected word in the blue domain is clicked. And users will give the grammatical information when a button corresponding to the selected phrase or clause is clicked after clicking "GRAMMAR" button in the purple domain.

4 Conclusions

The machine translation is a technique which can cross the language barrier so that people all over the world can share information with each other. In this study, I developed an Adam document support tool by using Ajax for multilingual semi-machine translation based on Collective Intelligence which is suggested to enable high-accuracy translation. By this tool, we can make Adam document on Web.

Performance could be improved, by adding a support function to make Adam document by anyone who is not familiar with English, and adding other languages on the web user interface as well as English, and making it possible to read a local file. It is also necessary to make the conversion rules of Lilith system by Collective Intelligence, and letting Lilith system work not only on the native enviroment but also on the Web.

References

[1] Takuya ISHIBASHI. Study of multilingual semi-machine translation based on Collective Intelligence. Master's thesis, Tokyo Institute of Technology, 2008.

[2] James Surowiecki. The WISDOM OF CROWDS. Anchor, Aug. 2005.

the Effect of Arc Current and Distance between Electrodes on Reignition Executable Time in DC Arc Discharge

Student Number: 11_06120 Name: Yuki ORIMO Supervisor: Kunio TAKAHASHI

1 Introduction

Arc discharge is the phenomenon of electric current flowing in gas between electrodes. It is applied to welding because high temperature that can melt the electrodes occurs. Breakdown voltage of gas ranges from a few kV to tens kV, but reignition voltage is lower than that voltage[2]. If reignition voltage is the same level with voltage between electrodes before extinction of arc, it can be reignited easily. In this report, "reignition executable time" is defined as the range of arc-less time which reignition is executable in.

In arc welding, anode melts more than cathode because of emission of the energy equivalent to anode's work function. This causes problems because the amount of melt effects on strength and shape of welded part. There is a way capable to solve this problem by altering polarity of arc discharge considering reignition executable time. Therefore it is important to measure reignition executable time and understand the occurrence condition of reignition. In this research, the effect of arc current and distance between electrodes is investigated and cleared the occurrence condition of reignition is clarified.

2 Experiment method and equipment

To investigate the effect of arc current and distance between electrodes, reignition in control of arc current, distance between electrodes and arc-less time is attempted. The experiment system and the discharge circuit are shown in Fig. 1.

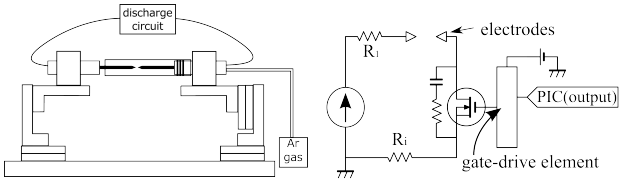

Fig. 1: Schematic illustration of experiment system and arc discharge circuit

Arc discharge is generated by touch start. After starting arc discharge, arc current, distance between electrodes are set to the target value and waited until arc discharge became settle. In stable condition, arc current is stopped by MOSFET switch and voltage between electrodes is set to 0V. After arc-less time, reignition is attempted by raising voltage between electrodes to the same level before extinction of arc.

The electrodes is ThO_2-W and its diameter is 1mm. Shield gas is Ar and its flow rate is 0.55L/min. Constant current source is used, its open-circuit voltage is 61.6V. $R_1(10\,\Omega)$ is used to limit the current at touch start. Voltage between electrodes, voltage drop at R_i and gate-source voltage of MOSFET are measured by a oscilloscope.

3 Experiment results

The Change of arc current with time in case that reignition is succeeded and failed is shown in Fig. 2, 3. Fig. 2 shows in case that arc current is 1.15A, distance between electrodes is 30mm, arc-less time is 300 µs and reignition are successful. Fig. 3 shows in case that arc current is 1.15A, distance between electrodes is 30mm, arc-less time is 350 µs and reignition is failed. If successful, arc current is stopped once, and after arc-less time, it started to flow from small current. In this report, "initial current" is defined as

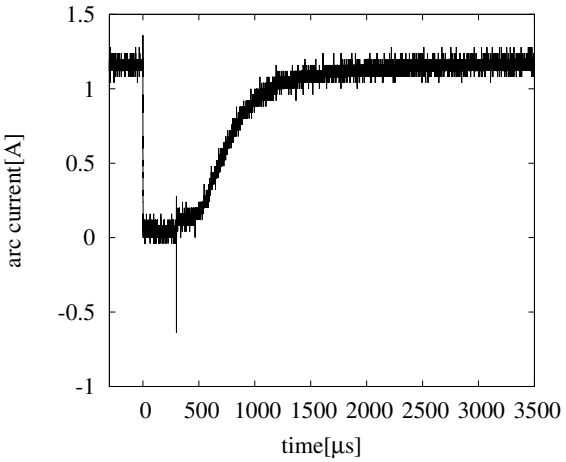

Fig. 2: Change of current between electrodes in case of arc-less time = 300 µs, arc current = 1.15A, distance between electrodes = 30mm

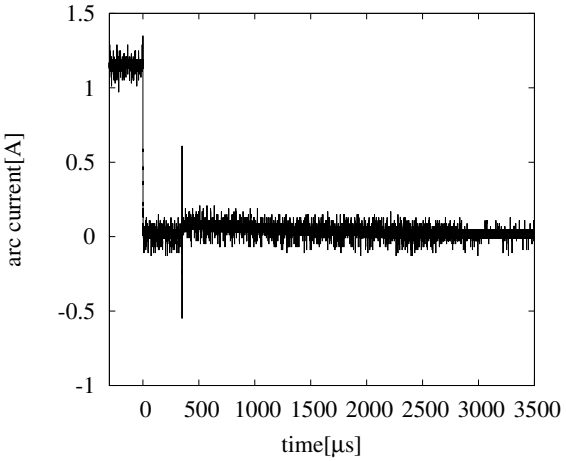

Fig. 3: Change of current between electrodes in case of arc-less time = 350 µs, arc current = 1.15A, distance between electrodes = 30mm

this small current. If failed, after arc-less time, initial current flows but over time it attenuates and finally vanishes.

Reignition executable time is defined rigorously here. In each conditions reignition executable time is the range of arc-less time in which reigniton success rate is over 50%. Fig. 4 shows relation between reignition executable time, arc current and distance between electrodes. From this graph, we can see positive correlation between arc current and reignition executable time and negative correlation between distance between electrodes and reignition executable time.The effect of arc current and distance between electrodes on reignition executable time are suggested.

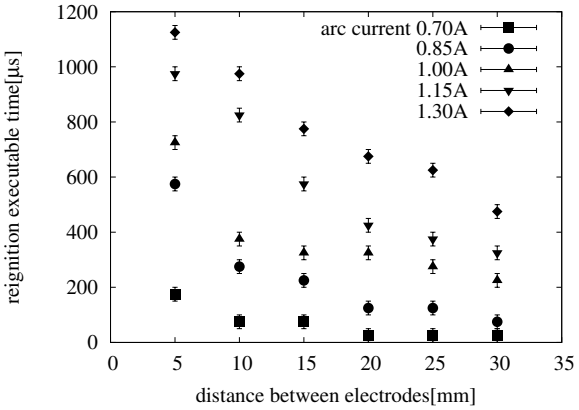

Fig. 4: Reignition executable time

4 Discussion

The difference between reignition and general discharge is that electrodes is high temperature to glow by preceding arc discharge. Voltage is applied to cathode in high temperature, so electrons is easy to be emitted from cathode by thermal electron emission[4], initial current increases. The amount of initial current contributes to reignition because this causes impact ionization and gets to discharge again. Electrodes temperature determines initial current and arc current determines electrodes temperature. It is obvious from energy consumed at discharge that the more the arc current, the higher the temperature of electrodes. Hereby I can explain positive correlation between arc current and reignition executable time.

The longer the distance between electrodes, the weaker the electric field intensity. In the mechanism of starting arc discharge, it is possibly that electric field intensity effects on acceleration of electrons and cations from impact ionization[1]. If electrons have enough energy at impact, initial current can cause impact ionization. That is, the stronger the electric field intensity, the easier the reignition occurs.

Initial current changes by arc current and arc-less time. Accordingly, Fig. 5 shows whether reignition success rate exceeds 50%, being fixed arc-less time and being set arc current and electric field intensity(voltage/distance between electrodes) as variables. This indicates the conditions of reignition about arc current and electric field intensity, interdependence between arc current and electric field intensity.

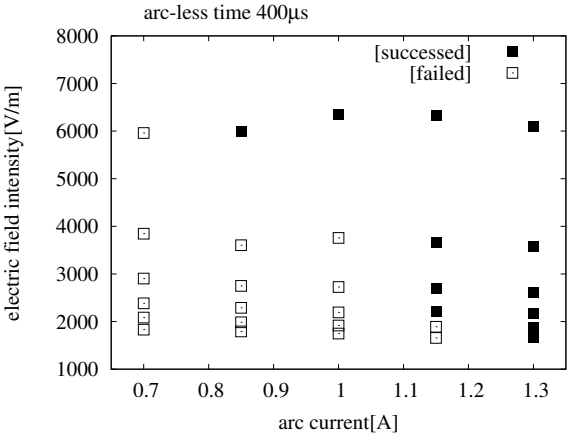

Fig. 5: Threshold of arc current and electric field intensity in case of arc-less time = 400 μs

5 Conclusions

In this report, I measured reignition executable time through experiments in control of arc current, distance between electrodes and arc-less time, and investigated the effect of arc current and distance between electrodes. Positive correlation between arc current and reignition executable time and negative correlation between distance between electrodes and reignition executable time are clarified. These causes are considered arc current and distance between electrodes deciding electrodes temperature and electric field intensity. Additionally thresholds of arc current an electric field intensity required by reignition became obvious from graphs as shown in Fig. 4, Fig. 5.

6 References

[1] Mase HIROSI, “Plasma Production by D. C. Discharge”, J. Plasma Fusion Res., Vol. 3 No. 69 P237-242 (1993)

[2]Mikio MOTOKI, Masaaki ONO, Yukichi KAMIIDE, “Gap Phenomenon in Discharge Process”, Journal of The Japan Society of Electrical Machining Engineers, Vol. 8 No. 15 P44-53 (1974)

[3] Masayoshi OZAWA, Toshikatsu MORITA, Kunio OMURA, “On the After-Arc Phenomena”, Journal of JWS, Vol. 24 No. 1 P5-11 (1955)

[4] Yoshihiro MUROOKA, K. R. Hearne, “The Effect of Electrode Temperature on Spark Brearkdown Voltage”, The transactions of the Institute of Electrical Engineers of Japan.A, Vol. 92-A No9 P19-26 (1972)

Facilitation of methane production from wastewater containing soybean oil by microbial pretreatment

Student Number: 11-15410 Name: Kazumasa TANAKA Supervisor: Kiyohiko NAKASAKI

1. Introduction

Fat is one of the major organic matters in wastewater from food processing factory. Fat is a cause of the scum which is difficult to be treated in the process of the wastewater treatment. For this reason, the fat contained in the wastewater is usually separated and discarded as the industrial waste before the biological treatment stage. However, the fat can be a good substrate for methane fermentation as in theoretical value, 850 mL of methane gas can be produced from 1 g of fat, even though 500 mL of methane gas can be produced from 1 g of protein, and 395 mL of methane gas can be produced from 1 g of carbohydrate [1]. Furthermore, utilization of the fat for methane fermentation will reduce the cost and environmental damage caused by the disposal of the fat. So the establishment of methane fermentation of wastewater containing fat is desired.

In this study, degradation pretreatment of the soybean oil by the microorganism which can degrade the fat was investigated for the facilitation of the methane production from the wastewater containing fat.

2. Materials and methods

2-1. Methane fermentation of soybean oil pretreated by fat degrading bacteria

Strain T1 isolated as the fat degrading bacteria was precultivated in 50 mL of TS broth at 30ºC for 3 days. Then 0.5 mL of the preculture was inoculated to 300 mL of TS oil broth that was composed of 75 g/L of soybean oil, 25 g/L of trypticase and inorganic nutrients and cultivated at 30ºC for 5 days. After 5 days cultivation, the culture was used for methane fermentation.

The mixture of the culture of T1 in TS oil broth and glucose, sodium acetate, lactic acid was used as substrate for methane fermentation. Two kinds of the substrates with different mixing ratio of the culture of T1 in TS oil broth and glucose, sodium acetate, lactic acid, designated as BO-0, BO-25 were prepared. The compositions of those substrates are shown in Table 1. Those substrates were supplied in a stepwise manner: 0-15 days with BO-0, 16-36 days with BO-25.

For the startup of the experiment, 1 L of granular sludge from food processing factory and 1 L of BO-0 were mixed in the anaerobic sequencing batch reactor (ASBR). The reactor was made of Pyrex glass and had a working capacity of 2.5 L. The value of pH of the mixture of granular sludge and BO-0 was adjusted around 8.0 with NaOH, and the reactor was flushed with N_2 for 10 min. The temperature in the reactor was maintained at 39 ºC by water jacket, and the solution was agitated with a stirrer at 100 rpm. In this experiment, 400 mL of supernatant was extracted from the reactor, and the same volume of fresh substrate was fed every day.

The value of pH and ORP was measured by the pH and ORP meter respectively. A sample of the exhaust gas was captured into a plastic bag and gas compositions were measured by GC-MS. Gas volume was measured using dry test gas meter.

Table 1 Composition of the BO-0 and BO-25.

	BO-0	BO-25
Glucose (g/L)	12.5	9.38
Sodium acetate (g/L)	6.25	4.69
Lactic acid (g/L)	5.55	4.16
Soybean oil contained in the substrate (g/L)	0	2.6

2-2. Methane fermentation of soybean oil pretreated by fat degrading yeast

Two strains of yeast, *Pseudozyma antarctica* NBRC 10260 and *Pseudozyma rugulosa* NBRC 10877 were used to pretreat the soybean oil. The yeasts were precultivated in 50 mL of YM broth at 25 ºC for 2 days. Then, 0.5 mL of the preculture was inoculated to 100 mL of Yeast oil broth that was composed of 20 g/L of soybean oil, 3 g/L of yeast extract and inorganic nutrients and cultivated at 25ºC for 7 days. After 7 days cultivation, the culture was used for methane fermentation.

The mixture of the culture of yeasts in Yeast oil broth and glucose, sodium acetate, lactic acid was used as substrate for methane fermentation. Three kinds of the substrate with different mixing ratio of the culture of yeast in Yeast oil broth and glucose, sodium acetate, lactic acid, designated as YO-0, YO-25 and YO-50 were prepared. The compositions of those substrates are shown in Table 2. Those substrates were supplied in a stepwise manner: 0-13 days with YO-0, 14-47 days with YO-25 and 48-64 days with YO-50.

For the startup of the experiment, 1 L of granular sludge from food processing factory and 1 L of YO-0 were mixed in the anaerobic reactor. The adjustment of pH, flushing of the reactor by N_2, and fermentation condition were the same with previous experiment. In this experiment, 200 mL of supernatant was extracted from the reactor, and the same volume of fresh substrate was fed every day.

Physicochemical analyses for taken samples were the same with previous experiment.

Table 2 Composition of the YO-0, YO-25 and YO-50.

	YO-0	YO-25	YO-50
Glucose (g/L)	11.86	8.9	5.93
Sodium acetate (g/L)	5.93	4.45	2.97
Lactic acid (g/L)	5.27	3.95	2.64
Soybean oil contained in the substrate (g/L)	0	2	4

3. Results and discussion

3-1. Methane fermentation of soybean oil pretreated by T1

Fig. 1 shows the courses of total gas volume in the fermentation of soybean oil pretreated by T1. After changing the substrate to BO-25, the total gas volume increased until day 24. It is considered the trypticase contained in the TS oil broth of BO-25 was consumed by the microorganisms, and gas was produced consequently. Then, after day 24, the total gas volume decreased to around 1 L until day 34. It is reported that *Bacillus amyloliquefaciens* can produce the biosurfactant called fengycin which is toxic for the microorganisms [2,3]. It is considered that the culture of T1 in TS oil broth contained fengycin, and accumulation of fengycin inhibited the methanogen activity.

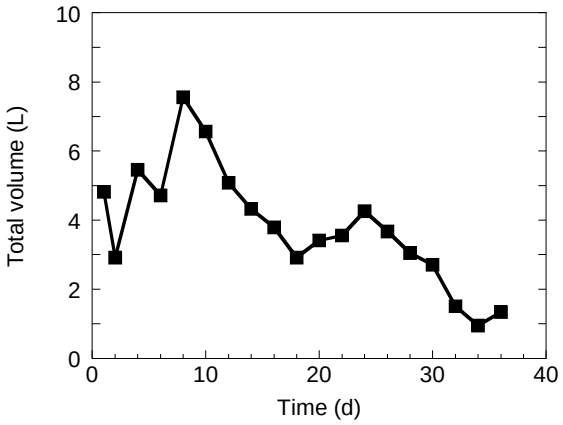

Fig. 1 Courses of total gas volume from BO-0 and BO-25.

3-2. Methane fermentation of soybean oil pretreated by yeast

Fig. 2 shows the courses of total gas volume in the fermentation of soybean oil pretreated by yeasts. During 1 to 10 days of fermentation, the gas production was not stable. Then, the volume became stable from day 10. After changing the substrate to YO-25 at day 14, the gas volume decreased to around 1.5 L. Then, the volume began to increase at day 22, and reached at around 2.5 L on day 26 that is almost the same volume with that observed before changing the substrate to BO-25. It is considered that during 22 to 26 days, microorganisms were acclimated to utilize the Yeast oil broth in the YO-25. After changing the substrate to YO-50 at day 48, the gas volume decreased to around 1.5 L, and did not recover until the end of fermentation.

Long Chain Fatty Acid is produced in the degradation of fat, and it is known that the high concentration of LCFA cause the inhibition against microorganisms [4]. In this experiment, it is considered that LCFA was produced during the pretreatment of soybean oil. And YO-50 contained higher amount of soybean oil than O-25. As a result, YO-50 may have contained higher amount of LCFA than O-25. Therefore, it is considered that the concentration of LCFA in the reactor increased after change of the substrate from YO-25 to YO-50, which led the decrease of the gas production.

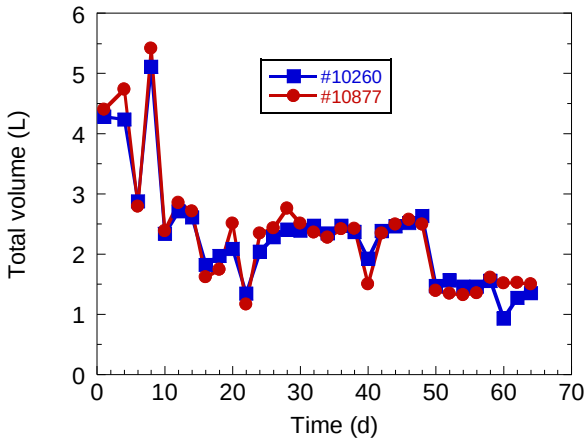

Fig. 2 Courses of total gas volume from YO-0, YO-25 and YO-50.

4. Conclusions

The methane could be produced from Yeast oil broth pretreated by *P. antarctica* NBRC 10260 and *P. rugulosa* NBRC 10877 which produce nontoxic biosurfactant while the TS oil broth pretreated by T1 could not be used for methane fermentation due to the toxicity of the biosurfactant produced by T1.

Reference

[1] N. Kataoka et al. : Studies on a Methane Fermentation Process for Treating Oil and Fat Containing Food-processing Wastewater, Ebara engineering review, 212, 3-9 (2006).

[2] S. Lee et al. : Isolation, Purification, and Characterization of Novel Fengycin Sfrom Bacillus amyloliquefaciens LSC04 Degrading-Crude Oil, Biotechnology and Bioprocess Engineering, 15, 246-253 (2010) .

[3] T. Okano : 殺菌と界面活性剤の話, Kao Hygiene Solution, 7, 24-25 (2004).

[4] I. Angelidaki et al. : Effects of free long-chain fatty acids on thermophilic anaerobic digestion, Appl Microbial Biotechnol, 37, 808-812 (1992).

Arch action in embankments subjected to subsidence of foundation

Student ID: 11_24247　Name: Yoshito MIYATA　Supervisor: Jiro TAKEMURA

1. Introduction

Because of the great east Japan earthquake on March 11th 2011, many embankments was collapsed. According to the report of Ministry of Land, Infrastructure and Transport (MLIT), these embankments are collapsed by liquefaction due to inundation in the loose part of beneath embankment before earthquake attacked. But until quite recently, liquefaction occurs only sand ground which was formed in natural condition. So, it is important to research how internal sand condition goes loose. In this study, I consider this mechanism by noting the variation of internal stress which is subjected to subsidence of foundation. To research this mechanism, a series of 1G physical models of an embankment inclined at angle of repose was conducted with four different heights. If we clarify the mechanism reducing the resistance to liquefaction in this study, it will contributes to design the embankments which have some resistance to liquefaction.

2. Physical model

Physical models was conducted by using apparatus which can make subsidence. This subsidence speed was controlled 0.041mm/s by actuator without making any external effect. The value of subsidence is determined by using dial gauge fixed under the apparatus. Frame of apparatus was made of Aluminum and surface of apparatus is covered with teflon sheet to reduce the friction between beneath the embankment and surface of apparatus. To determine the soil pressure beneath the embankment, four pressure gauges is fixed on apparatus not making any difference of height between surface of apparatus and pressure gauges. Each pressure gauge is fixed 30mm, 55mm, 100mm, 150mm from centerline of apparatus whose value of subsidence is maximum.

Sand spreader was used to make embankments. The height of spreading sand is 10mm from top of embankments to make embankments' density uniformly. And height of embankment is controlled by changing the number of sand spreader's reversal. Normally, we can make triangle embankment reversing sand spreader four times. After making embankment on the apparatus, we made subsidence and determined the value of pressure by using data logger. We determined sand density by using density pan which was made of acryl. Eight density pans was put on apparatus before making embankment and removed carefully without giving external effect after conducting subsidence. Each two density pans are fixed same distance of pressure gauges from centerline of apparatus.

Silica sand No.8 and No.6 are used to make embankments. Their physical value is as follows.

Table 1 Physical value of silica sand No.8

Parameters	Values and
Specific gravity	2.637
Maximum grain size	0.250 mm
Medium grain size	0.090 mm
Uniformity coefficient	3.05
Minimum density	1.153 g/cm^3
Maximum density	1.554 g/cm^3

Table 2 Physical value of silica sand No.6

Parameters	Values and
Specific gravity	2.643
Maximum grain size	0.850 mm
Medium grain size	0.316 mm
Uniformity coefficient	1.30
Minimum density	1.241 g/cm^3
Maximum density	1.556g/cm^3

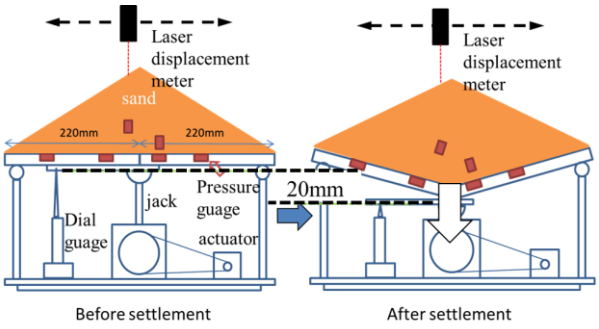

Fig. 1 Sectional view of experiment

3. Experimental theory

I used the concept of Fixed Principal stress Analysis (FPA) to this study. This way assumes the direction of principal stress. In this study, I determined the direction of principal stress as Fig.2 from Mohr-Coulomb yield criterion. Next, I divide embankments into six areas as Fig.3 to decide boundary condition of Lame-Maxwell equation as follows.

$$\frac{\delta\sigma_1}{\delta\xi} = \gamma \sin\psi$$ The equation for direction of ξ

$$\frac{\delta\sigma_3}{\delta\eta} = \gamma \cos\psi$$ The equation for direction of η

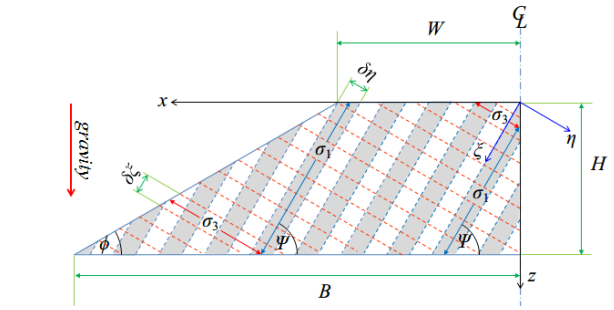

Fig.2 The direction of principal stress after subsidence occured

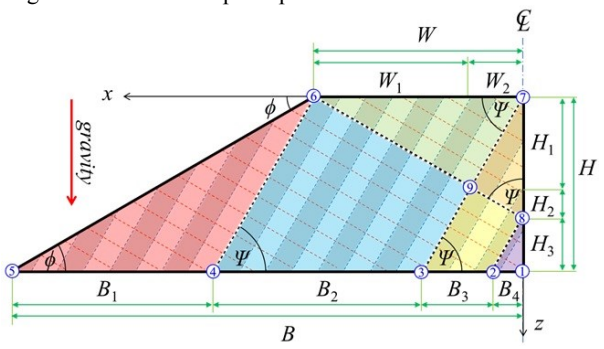

Fig.3 Divided areas of embankment

Note: Angle ϕ means angle of repose, and angle ψ means angle of $\sigma 1$'s rotation from z axis.

4. Result and discussion

Table.3 Experimental condition

Test	embankment's height	settlement	density
1	152mm	40mm	1.37g/cm^3
2	148.4mm	20mm	1.31g/cm^3
3	124.8mm	20mm	1.31g/cm^3
4	96.2mm	20mm	1.29g/cm^3
5	57.2mm	20mm	1.27g/cm^3
6	125.4mm	20mm	1.29g/cm^3
7	82mm	20mm	1.31g/cm^3
8	40.6mm	20mm	1.31g/cm^3
9	146.6mm	10mm×3	1.32g/cm^3
10	85.4mm	10mm×3	1.31g/cm^3
11	142mm	20mm	1.45g/cm^3
12	118.6mm	20mm	1.42g/cm^3
13	87.4mm	20mm	1.46g/cm^3
14	50.2mm	20mm	1.44g/cm^3
15	117.8mm	20mm	1.49g/cm^3
16	80.6mm	20mm	1.44g/cm^3
17	39.4mm	20mm	1.43g/cm^3
18	142mm	10mm×3	1.43g/cm^3
19	87.4mm	10mm×3	1.44g/cm^3
20	144.4mm	2.5,5,10mm	1.41g/cm^3
21	87.4mm	2.5,5,10mm	1.43g/cm^3
22	150mm	20mm	1.47g/cm^3
23	100mm	20mm	1.47g/cm^3
24	75mm	20mm	1.47g/cm^3
25	50mm	20mm	1.47g/cm^3

Note: From Test1 to 10 are conducted by dry silica sand No.8, from Test 11 to 21 was conducted by dry silica sand No.6 and from Test22 to 25 was conducted by moist silica sand No.6 whose water ratio was 10%.

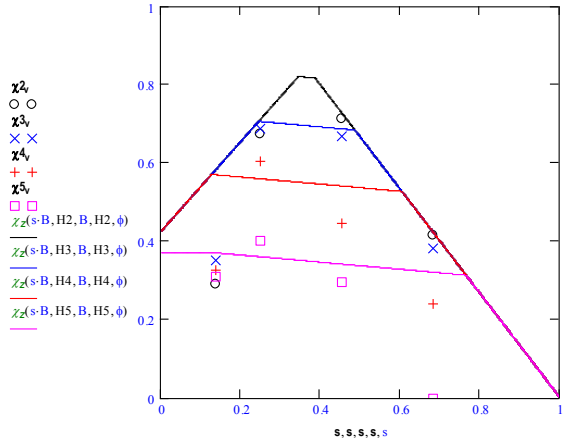

Fig.4 The result of Test2 to 5 (subsidence 10mm)

Note: Vertical axis is non-dimensional vertical pressure and horizontal axis is non-dimensional distance from centerline of the apparatus. Real line is analysis solution from FPA. Each point is result of experiment. Black line is the result of Test2, blue line is that of Test3, red line is that of Test4, and pink line is that of Test5.

I conducted same experiment using silica sand No.8 and No.6 to consider the difference of grain size. Also, to consider the difference between dry condition and unsaturated condition, I used moist silica sand No.6. Fig.4 shows that the result of Test2 to 5. Before subsidence occurred, pressure of the bottom center of embankment is higher any other point. But after settlement, we can see the pressure of center decreased. It is because the direction of principal stress is changed. Particularly the shape of principal stress is like an arch (arch action). Also we can see the pink line, that is the result of Test5 near the center of embankment doesn't change. So there is something like the ratio of embankment's width and height which determine not to occur the arch action.

But results of Test22 to 25 depend on the way to making embankment much, so the way to make embankment uniformly is my challenging for the future.

5. Conclusion

1. The pressure of center beneath embankment decreased rapidly after subsistence started.
2. The lower embankment is, the lower effect of arch action occur in the embankment.
3. The shape of embankment while foundation subsides doesn't change uniformly.
4. The soil pressure beneath embankment changed more rapidly in unsaturated condition than in dry condition.

6. Reference

1) JP. Wittmer, P. Claudin, M.E. Cates, and J.P. Bouchaud: An explanation for the central stress minimum in sand piles, Nature 382(6589), pp.336-338, 1996.

2) ピパットポンサー・ティラポン, 竹山智英: 安息角で形成された平面状斜面における固定主応力軸を仮定した応力解析, 第 45 回地盤工学研究発表会講演集, pp.305-306, 2010.